University of Seville

Faculty of Physics

Department of Condensed Matter Physics

High-temperature plastic deformation of micro and nano-boron carbide and B_4C-based composites prepared by spark plasma sintering (SPS): experimental and modelling.

Deformación plástica a alta temperatura de carburo de boro micro y nano-estructurado y materiales compuestos basados en éste preparados mediante sinterizado por chispa de plasma (SPS): experimentos y modelización.

Ph. D. dissertation proposed by Bibi Malmal Moshtaghioun to get the Doctoral degree with International Mention.

Advisors:
Prof. Arturo Domínguez Rodríguez
Dr. Miguel Castillo Rodríguez

Seville, April 2015.

List of contents

Chapter I: Introduction

The famous Polish anthropologist Bronisław Malinowski (1884-1942) defined the term culture in terms of its functionality for the human being. Culture cannot be separated from the tools that humans created to cover their biological and social needs. In this sense, science in general and materials science in particular, are landmarks of the culture of the mankind. The progress of societies are intrinsically linked to the improvements on tools that humans can fabricate for the sake of easy access to food, water, military advantages or commodities.

A few clear examples can be addressed: our civilization gained a competitive advantage for survival during the iron age: this is the beginning of the technology of metals, which opened up new opportunities for fabricating more solid and better tools for agriculture or for defense. Generally speaking, the knowledge of metallurgy has been one of the pillars of the technological development of societies from the last 2500 years. The discovery of steel was also a keystone which modified the political, economic and social evolution of many countries. More recently, the fabrication of plastics was a revolution. It is obvious how plastics and polymers in general are present in most of the tools commonly used in our daily life.

Nowadays, the search of new materials for more and more sophisticated applications or for several functionalities simultaneously is a one basic ingredient of the more promising countries. Even more, the countries which do not pay attention to this goal have in common a slow and unavoidable tendency to social and economic decline.

Ceramics are among the materials which are receiving more considerable attention in the first decades of the twenty-first Century. This is the consequence of several facts: first, they are well-known and abundant in Nature. Secondly, they are pretty stable from a chemical point of view: ceramic plates vessels are found in Yazd (Iran) dated back more than 3000 years ago….and the external decoration can still be seen. Thirdly, many of them are excellent structural materials with outstanding hardness. Unfortunately such shiny prospective is darkened by the low resistance to crack propagation; i.e. ceramics are brittle.

Nowadays, research on new ceramic systems or on the use of new techniques of fabrication of some classical systems is at the forefront of the modern science of materials.

One intriguing family of ceramics is that of covalent carbides. It is very well-known that carbon is the ubiquitous element in earth and the mere existence of life is a consequence of the chemical easiness to form long chains. Boron, carbon and silicon are elements

sharing many common properties. All of them are light ones and they are usually found in compounds in Nature. They can combine to form carbides such as silicon carbide or boron carbide. The first one was discovered in the 19th Century when routes to fabricate artificial diamonds were searched. Edward Goodrich Acheson failed to this purpose but he succeeded to fabricate an unknown system until that time that is rarely found in our planet. And the new carbide is extraordinarily hard. Regarding the second one, boron carbide was fabricated in the first decades of the twentieth Century. Regarding boron carbide, it was discovered in the mid 19th Century as a by-product in the production of metal borides, but only studied in detail since 1930. It is one of the hardest materials known, ranking third behind diamond and cubic boron nitride. This is the material which will be object of our attention in this PhD dissertation.

In general, the element boron is a very challenging and attractive one due to its excellent combination of physical properties of its compounds with carbon, nitrogen or some transition metals. Being a very light element, boron itself has the highest tensile strength reported among the elements. Boron has the ability to create complex structures such as carbon. However, carbon tends to saturate the four sp3 orbitals and create long chains (the origin of Organic Chemistry); boron, on the contrary, has a ternary valency and it turns to create caged structures. Such tendency is very clear in compounds such as boron carbide, as displayed later on in this work. The exploration of the mechanical properties of these structures is still a pending task in science.

Boron carbide has a major limitation: fabrication of fully-dense specimens is a very tough goal, because the diffusivity of chemical species in its lattice is rather low. This is the reason why fabrication of ceramic pieces requires very high temperatures and stresses, restricting the large-scale applicability in daily life. Quite recently, this severe limitation has been partially overcome: the use of advanced sinterization techniques such as "spark plasma sintering" has allowed fabrication of "almost" fully-dense species at temperatures ranged from 1600-2000ºC.

This PhD dissertation is devoted to the sintering, microstructural characterization, room temperature fracture properties and high-temperature plasticity of fully-dense fine-grained polycrystals of boron carbide.

Fabrication has been carried out by means of spark-plasma sintering. Optimization of the temperature and external pressure conditions was performed, permitting the fabrication of fully dense specimens at 1600ºC with average grain size approximately equal to 600 nm. Moreover, nanopowders were used to the aim of obtaining

nanostructured polycrystals. Such goal has been fulfilled, at least for specimens with average grain size around 150 nm.

The fabricated specimens were tested for determination of the fracture properties and the mechanisms driving these ones. In addition to that, microstructural characterization of the grain microstructure has been made by electron microscopy techniques.

With respect to the high-temperature plasticity, a virgin region in the forest of novel properties of this exciting material, creep studies has been systematically conducted in compression at temperatures ranged from 1500-1800ºC. The analysis of the mechanical tests, together with the additional piece of information provided by the post-mortem microstructural observation, opens up an unexpected surprise: creep behavior cannot be explained in terms of the conventional models for large-strain ceramic plasticity. An original model is developed, which has been validated with the experimental results. The agreement is rather satisfactory. This model shows the outstanding role of the interaction between dislocations and twins in high-temperature plasticity of these high-refractory ceramics.

This book is organized as follows: chapter 2 is concentrated on the "state of the art" of boron carbide ceramics, with special emphasis on the description of the outstanding physical properties which makes them so special. Chapter 3 is a summary of the experimental techniques used along this research work. Experimental results for specimen fabrication, optimization conditions for fully-dense sample preparation, mechanical tests and microstructural characterization are collected in chapter 4.

The room-temperature fracture properties are discussed also in this chapter. Chapter 5 is the discussion of the high-temperature plasticity. Modelling of this is carefully analyzed and validation is also done in this chapter.

Finally, chapter 6 is a brief summary of the main original achievements of this research work and it concludes this presentation.

Chapter II: Literature review and theoretical background

2-1- Boron carbide

In the group of the most important non-metallic hard materials (silicon carbide, silicon nitride, diamond or cubic boron nitride), boron carbide occupies a specific place since it is the third hardest material known and the hardest material produced in tonnage quantities. This compound was first discovered as early as 1858 and first synthesized artificially by Joly in 1883, when it was identified as B_3C. In 1934 its stoichiometric formula was assigned as B_4C. Today boron carbide refers to a wide range of composition, from $B_{10.4}C$ (8.8 at.-%C) to B_4C (20 at.-%C). Except B_4C, other compounds within this range of composition are regarded as solid solution of carbon in B_4C[1]. Boron carbide is characterized by a unique combination of properties that make it a material of choice for a wide range of engineering applications. Boron carbide is used in refractory applications due to its high melting point and thermal stability; it is used as abrasive powders and coatings due to its extreme abrasion resistance; it excels in ballistic performance due to its high hardness and low density; and it is commonly used in nuclear applications as neutron radiation absorbent. In addition, boron carbide is a high temperature semiconductor that can potentially be used for novel electronic applications [2]. The brief details about physical properties and main applications are described in section 2-3 and 2-4, respectively.

2-2- Crystal structure and phase diagram

The primary structural units of boron carbide are the 12-atom icosahedra located at the vertices of a rhombohedral lattice of trigonal symmetry ($R\bar{3}m$ space group), and the 3-atom linear chains that link the icosahedra along the (111) rhombohedral axis, as illustrated in Fig. 2.1 [3]. This structure can also be described in terms of a hexagonal lattice based on a nonprimitive unit cell, in which case the [0001] axis of the hexagonal lattice corresponds to the [111] rhombohedral direction (Fig. 2.2). The longest diagonal of the rhombohedral unit cell normally contains a three-atom linear chain of C-B-C type. Each end member of the chain is bonded covalently to an atom of three different icosahedra. In general, icosahedra consist of 11 boron atoms and one carbon atom. The locations of carbon atoms within different icosahedra are not ordered relative to one another. The icosohedral configuration is the result of a tendency to form three centre covalent bonds due to deficiency of valence electrons of boron. In other words, the presence of icosahedra within the boron carbide structure is a consequence of elemental boron's ability to form caged structures of a variety of sizes; the icosahedra in boron carbide are essentially two pentagonal pyramids bonded together[2]. Two

crystallographically inequivalent sites exist in the icosahedron. Six atoms reside in two polar triangles at the opposite ends of the icosahedron and the remaining six atoms occupy equatorial sites. The atoms at polar sites are directly linked to neighbouring icosahedra via strong two-centre bonds along the cell edges. The atoms in equatorial sites either bond directly to other icosahedra through three centre bonds or to chain structures[4].

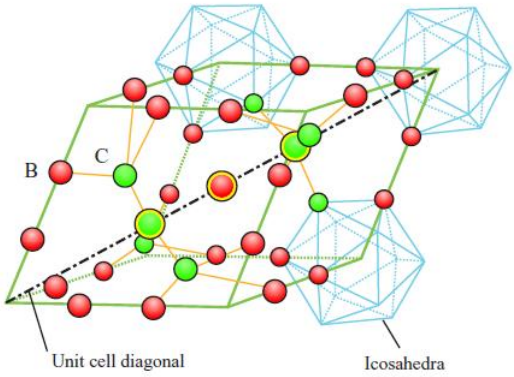

Fig. 2.1. Rhombohedral unit cell structure of B_4C showing $B_{11}C$ icosahedra and the diagonal chain of C-B-C atoms[3].

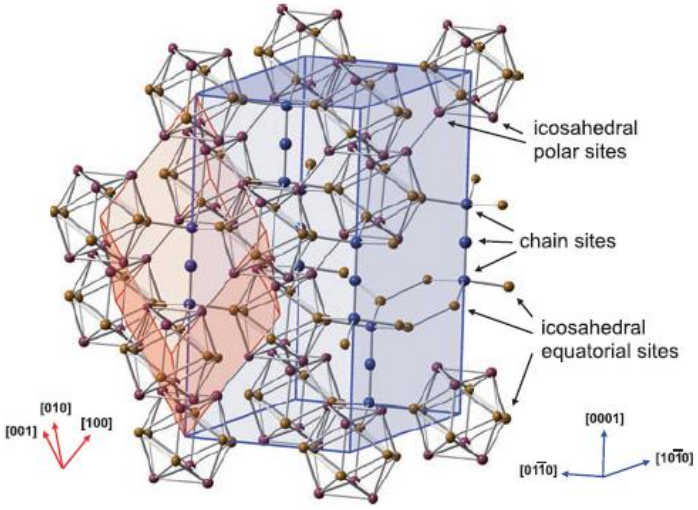

Fig. 2.2. Boron carbide lattice showing correlation between the rhombohedral (red) and the hexagonal (blue) unit cells. Inequivalent lattice sites are marked by arrows [5].

A more detailed description of icosahedra structure itself is followed below. Each icosahedron is bonded to six other icosahedra directly via strong two-centre bonds along the cell edges. The atoms forming these two-centre bonds are from two three-atom "poles", or caps, on the top and bottom of the icosahedra. The remaining six atoms in the so-called equatorial sites either bond directly to other atoms inside the icosahedra

through three-centre bonds or to the linear chain structures, as shown in Fig. 2.3. The carbon atoms within different icosahedra do not have some preferred locations relative to one another. In most of the icosahedra C atom is in a polar site, while in a few percent there is a B_{12} structure or a $B_{10}C_2$ structure with the two C atoms placed in two antipodal polar sites [6].

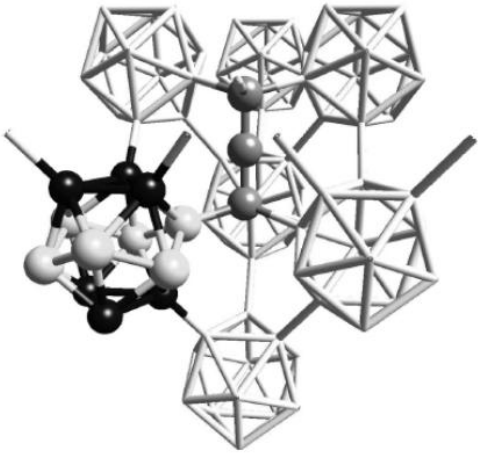

Fig. 2.3. Atomic structure of the icosahedron unit in B_4C. The black atoms are on the so-called polar sites, bonded to neighboring icosahedra. The white atoms form a puckered hexagon and are in equatorial sites. The grey atoms form the chain, to which the equatorial atoms are bonded[6].

Three types of three-atom chain are envisioned: C-B-C, C-B-B and B-B-B or B-□-B (the symbol □ –indicates an atom vacancy) since the similarly sized C and B atoms readily substitute for each other. Variation in carbon concentration changes the distribution of three-atom chains. B_4C (20%C) structure consists of $B_{11}C$ icosahedra and C-B-C chains. As the composition becomes rich in boron, carbon of the $B_{11}C$ icosahedra is retained, while one of the carbon atoms on the C-B-C chains is replaced by boron. Near the composition $B_{13}C_2$, the structure consists of $B_{11}C$ icosahedra and C-B-B chains. On further carbon reduction, some of the $B_{11}C$ icosahedra are replaced by B_{12} icosahedra retaining the C-B-B chain. Carbon-boron bonds present in the three atom chains are much stronger than boron-boron bond in icosahedra. The inter-icosahedra bonds are stiffer than the intra-icosahedra bonds [7].

Conflicting views still exist concerning the nature of site occupancies. A model based on early X-ray diffraction data proposed that the B_4C composition is made up of B_{12} icosahedra and C-C-C chains. However later studies based on improved X-ray and neutron diffraction, nuclear magnetic resonance studies, theoretical calculations and vibrational spectra indicate that the structure consist of $B_{11}C$ icosahedra and C-B-C

chains. Even among those who favour $B_{11}C$ icosahedra and CBC chain model for 20 at.-% C (B_4C), there is a disagreement on the structural changes that occur in boron carbides, as the carbon content is decreased towards 13 at.-%C ($B_{13}C_2$). It is proposed that carbon atoms are removed from the icosahedra to form B_{12} icosahedra, while there are other reports suggesting that carbon atom is replaced from three atom chains. Owing to similarity of boron and carbon in electron density and nuclear cross-section (B^{11} and C^{12}), both X-ray and neutron diffraction studies are not very successful in unambiguously assigning the exact site occupancies[5, 7, 8].

Fig. 2.4 shows phase diagrams of B-C. There is an agreement in the community about the existence of a wide range of solid solubility for carbon in the stable phase and a homogeneous range extending from ~8 at.% to ~20 at.% C. The rhombohedral lattice parameters for the carbon-rich B_4C compound are a = 5.16 Å and α = 65.7 °, with minor variations depending on the extent of the investigation. Converted into the more easily worked hexagonal lattice parameters, B_4C has values of a_0=5.60 Å, c_0 = 12.07 Å, and an axial ratio of c_0/a_0 = 2.155 [2, 9].

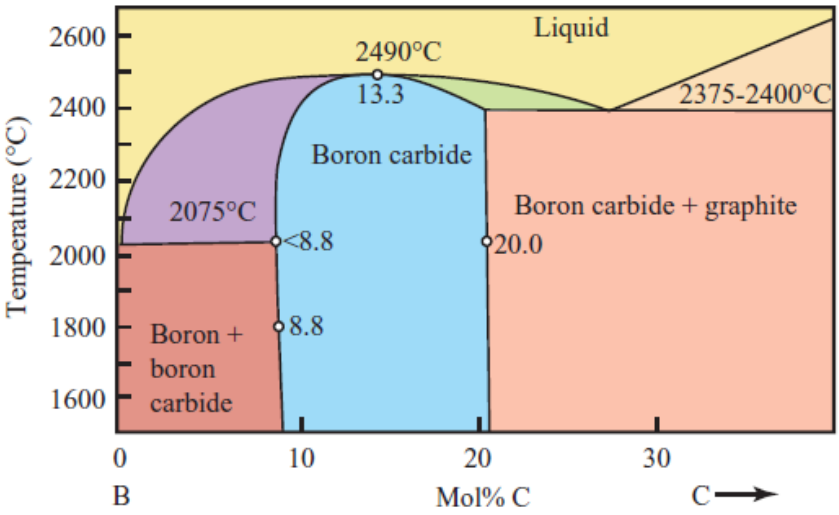

Fig. 2.4. Phase homogeneity range in B-C phase diagram [9].

2-3- Physical Properties of Boron Carbide

Physical properties and mechanical behaviour of boron carbide strongly depend on the final microstructure (grain size, density, porosity, impurities…) of the fabricated material, which is greatly influenced by the sintering characteristics: technique (SPS or MW), sintering temperature and pressure, holding time, use of sintering aids, etc.

Therefore the measured values reported by different researchers are hardly comparable. Here some physical properties of boron carbide are pointed out:

2-3-1- Density

The density of boron carbide increases linearly with carbon content within the homogeneity range of the phase. The dependence of boron carbide's theoretical density (d) on the carbon content [C]at.% can be expressed by Equation 2.1[1, 10].

$$d(g/cm^3) = 2.422 + 0.0048\ [C]at.\% \quad (r = 0.998) \tag{2.1}$$

with [C] ranging between 8.8 and 20.0 at.%. Then, the theoretical density for B_4C ([C] = 20.0 at.%) is 2.52 g/cm^3, for $B_{13}C_2$ ([C] = 13.3 at.%) is 2.488 g/cm^3 and for $B_{10.4}C$ ([C] = 8.7 at.%) is 2.465 g/cm^3.

2-3-2- Strength at room temperature

The mechanical properties measured on boron carbide samples, with densities close to the theoretical value, differ and depend on specific impurity contents (or second phase) and distribution, porosity, clusters of diffusion pores, grain size, etc. Therefore measurements are hardly comparable. .

Flexural strength depends on the stoichiometry of the compound. Within the homogeneous range of boron carbide, strength would increase with the carbon content. Beyond this range, the strength value will decrease due to the existence of free graphite. Besides, the pressureless-sintered B_4C samples show lower strength value than the HP or post- HIP treated ones. Different measurement methods also result in different strength values. Reported data of flexural strength are altered between 300 to 500 MPa.

The effect of porosity and grain size on the strength has been studied. The flexural strength decreases with increasing porosity and increasing grain size. Fig. 2.5 presents the relationship between the flexural strength and the porosity up to 30% [11]. Equation 2.2 and 2.3 show the relation from several models proposed by Knudsen and other researchers using empirical data from hot-pressed boron carbide.

$$\ln\sigma = 20.337 - 0.367 \ln D - 4.974P \tag{2.2}$$

and

$$\sigma = \sigma_0 e^{-bP} / D \tag{2.3}$$

where σ [11] is the flexural strength, σ_0 and b are constants, D [μm] is the mean grain size, and P is the volume fraction porosity[12].

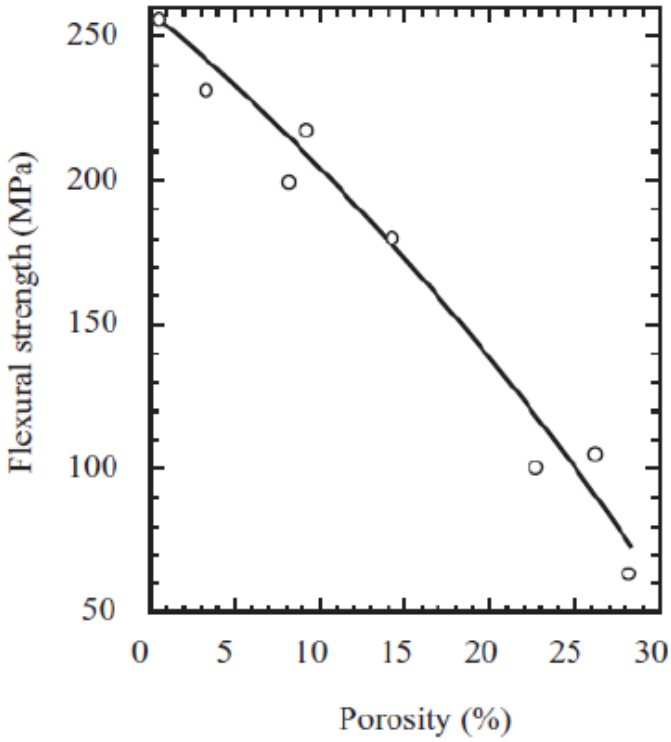

Fig. 2.5. The change of flexural strength of B4C with porosity[11]

2-3-3- Hardness

Boron carbide is among the third hardest materials after diamond and cBN. The hardness measurements of boron carbide are very difficult due to its high hardness value. Since the measurement conditions and the preparation processes of boron carbide samples are uncertain, the actual measured values of hardness are scattered, making comparisons difficult.

The influence of carbon content on boron carbide's hardness is debatable. Within the homogeneity range, as the carbon content increases, the structure of boron carbide becomes stiffer, so the hardness increases. For instance, after mechanical polishing, HK_{200g}= 2910 ± 90 kg mm^{-2} (29. 1 GPa) for 10.6 at. C %, and reaches 3770 ± 80 kg mm^{-2} (37.8 GPa) for 20 at.C % (B_4C, with maximum density) [1, 10].

Hardness values also depend on microstructure and on processing and densification parameters. Normal values of hardness for pressureless-sintered samples are around 25.5 ± 2.4 GPa, while for hot-pressed samples increase to 29.0±1.5 GPa. For modern techniques of sintering in presence of electric field like spark plasma sintering (SPS), values of hardness reach to values higher than 30 GPa [13, 14].

2-3-4- Fracture toughness

The fracture toughness (K_{IC}) can be obtained from either indentation tests or Single Edge Notched Beam (SENB) tests. A relatively wide range of fracture toughness values of boron carbide has been reported (2.9 - 3.7 $MPa.m^{1/2}$). There is obvious correlation between fracture toughness and microstructure (grain size and porosity) as well as the presence of second phases[15, 16].

Other mechanical properties of boron carbide, such as Young's modulus and shear modulus increase with carbon content. Table 2.1 gives the relation between the elastic properties and the carbon content [1].

Table 2.1. Elastic properties of boron carbide[1]

Carbon (%)	E (GPa)	G (GPa)	υ
20.0	471	200	0.18
18.2	465	197	0.18
15.4	466	197	0.18
13.3	450	189	0.19
11.5	351	150	0.17
10.0	348	150	0.16

2-3-5- Mechanical properties at high temperature in air and oxidation resistance

It is known that B_4C oxidation starts near 600 ˚C. From a thermodynamic point of view the following course of the reaction is the most probable one:

$$B_4C + 3O_2 = 2B_2O_3 + CO_2 \quad (2.4)$$

As a result of the reaction, liquid boron oxide is formed (melting point of B_2O_3, 577 ˚C). Up to 1100 ˚C, the oxidation results in a weight gain because of B_4C oxidation. Starting from 1200 ˚C, a linear weight loss is reported. This confirms that all boron oxide formed vaporizes from the surface of the material and the oxidation process at temperatures above 1200 ˚C is limited by the reaction rate. Within the temperature range of 650 – 1000 ˚C, a protective B_2O_3 film is formed on the sample surface. At 1000 ˚C the process becomes more rapid, and above 1200 ˚C catastrophic B_4C oxidation starts, accompanied by a considerable exothermic effect. The oxidation rate

up to 1200 ˚C is limited by the diffusion of the oxygen and carbide components through the oxide film.

In air there is a gradual decrease in strength between 600 and 1000˚C, due to superficial oxidation into B_2O_3. Above 1200 ˚C, catastrophic B_4C oxidation resulted in a complete degradation of strength. However, in fracture toughness tests, where a crack propagates from a previously-made notch, a larger number of defects on the sample surface obviously has no influence on the K_{IC} value [17].

2-3-6- Mechanical properties at high temperatures in inert atmosphere

High temperature deformation of boron carbide has deserved scarce interest. There is only one paper reporting the creep behaviour of pure B_4C. T. G. Abzianidze et al. [18] performed creep tests under compression up to 7% final elongation. They reported that creep in boron carbide at stress values lower than 90 MPa occurred by a vacancy-driven diffusive mechanism, for which n=1. At stress values over 90 MPa, n=3 and the creep mechanism was proposed to be consistent with dislocation creep. However, these statements were made in the lack of any microstructural analysis of the post-mortem specimens and are based on the values of the stress exponents and the common thumb's rule linking n=3 to dislocation activity and n=1 to diffusional creep. The creep activation energy in both cases is the same and equal to 385 kJ/mol, a value consistent with the activation energy for carbon diffusion in this system. In consequence, the mechanism of high-temperature creep of the fully dense of boron carbide ceramics is still unclear. However, there is neither a systematic work on this matter by means of large strain creep tests at the higher temperatures, nor a detailed modeling of the microstructural mechanisms involved for boron carbide. Brief review on the creep deformation mechanisms is pointed out in section 2-6.

2-3-7- Thermoelectrical properties

It is well-reported that the thermal conductivity λ reduces when the density reduces; i.e. the porosity increases. Regarding the dependence of this quantity with the carbon content, at the highest carbon concentration (B_4C), the thermal conductivity reaches its maximum value and it is also a decreasing function of temperature. By contrast, for lower carbon concentrations, the thermal conductivity gets much smaller values together with much weaker temperature dependence. The thermal conductivities of the

B_4C stoichiometric samples have a temperature dependence characteristic of a single crystal and the heat conduction mechanism occurs by phonon diffusion[19]. This is consistent with the view that at the B_4C composition all available intericosahedral chain positions are filled by CBC chains. At lower carbon concentrations only a fraction of the available chain locations are filled. Since these carbon-containing intericosahedral chains are relatively stiff, the absence of such structural units should affect the thermal conductivity. In particular, thermal transport through such a defect structure should resemble that of a partially-disordered material.

The electrical conductivity of boron carbides increases with temperature. The conduction mechanism is explained by hopping of small-polaron holes among carbon atoms in inequivalent sites or by a bipolaronic hopping. The hopping activation energy E, increases slightly when the C content increases; there is perhaps a break in the slope for 13.3at.%C. Boron carbide is a p-type semiconductor even at very high temperatures; the Seebeck coefficient (S) remains positive over the whole phase homogeneity range, increases slightly with temperature and reaches values of 200-300~V/K at 1250K.
The temperature dependence of the so-called figure of merit Z, defined as $Z = S^2 \sigma/\lambda$, is the parameter for rigorous comparison of thermoelectric performance. For all the phase homogeneity range of boron carbides the figure of merit Z increases with temperature. In particular, at the temperature of 1250K the 13.3 at.%C composition-sample possesses the highest Z value reported in this system: 0.85×10^{-3}/K. This Z value, obtained for the $B_{13}C_2$ compound, exceeds that of the best p-type Si-Ge alloys, generally used at these high temperatures. This fact emphasizes the promising perspectives of boron carbide for potential use in high-temperature thermoelectric generators [20].

2-4- Industrial Applications

Boron carbide has been widely used in industry due to some of the previously described properties, such as high hardness, high strength until high temperature and high neutron absorption ability, as well as good electrical properties.
The main industrial application of boron carbide is as abrasive powder or grit due to its outstanding hardness. Particle sizes are available from 1 μm to 10 mm, used for lapping, polishing, grinding media and water jet cutting.

Boron carbide are also used as a wear-resistant component of coatings in cutting tools of various alloys, such as brass, stainless steel, titanium alloys, aluminium alloys, cast iron, etc . Hot-pressed boron carbide ceramic is used for blasting nozzles, mortars and pestles due to its good wear resistance[1, 10].

Other important applications of boron carbide include their use in body vehicles, resulting from the combination of low specific weight, high hardness and impact resistance. Boron carbide is an effective strengthening medium because of its high modulus to density ratio, which is superior than most of the high temperature materials. The low density, high stiffness and low thermal expansion characteristics make B_4C attractive candidate to replace Be/Be alloy in aerospace applications[1, 10, 21, 22].

Owing to its high Seebeck coefficient (300 μV/K), boron carbide is widely used in carbide/graphite thermocouples until 2473 K. As a p-type semiconductor, boron carbide is found to be a potential candidate material for electronic devices at high temperatures, such as diodes and transistors and so on [23, 24].

Another significant application of B_4C can be found in nuclear industry due to its high ability to absorb neutron without forming long life-time radionuclide. B_4C is an important part of the control rods used for control and shut down of nuclear reactors. It is also extensively used as shielding materials and neutron detectors in nuclear reactors. Boron carbide composites with good thermal conductivity and thermal shock resistance are found suitable as first-wall material of nuclear fusion reactors. B_4C's neutron absorption capacity can be increased by enrichment in ^{10}B isotope. Because of its low neutron-induced radioactivity, low cost and high melting point, B_4C is an attractive material at this regard. Especially B_4C has revealed its best behaviour under fast neutrons: a large cross-section and no resonance in the whole spectrum [25-27].

2-5- Consolidation and sintering of boron carbide

In spite of its outstanding advantages, applications of B_4C have a major drawback: the severe difficulties in densification and low fracture toughness. Consolidation of B_4C is complicated due to its high melting point, low self-diffusion coefficient and high vapour pressure. Very high sintering temperatures are required for densification due to the presence of predominantly covalent bonds in B_4C. Boron carbide particles generally have a thin coating of surface oxide layer which hinders the densifications process. At temperatures <2000˚C, surface diffusion and evaporation condensation mechanism

occur, which results in mass transfer without densification. Densification is achieved only at temperatures >2000˚C, by grain boundary and volume diffusion mechanisms. At such high temperatures, exaggerated grain growth also takes place resulting in poor mechanical properties [7].

Grabchuk et al.[28] have found that shrinkage starts at 1500 ˚C, recrystallisation above 1800 ˚C and rapid grain growth above 2200 ˚C. Lee et al.[29] have observed the densification onset at 1800 ˚C, rapid increase in densification in between 1870–2010 ˚C and a slow down in densification rate in the range 2010–2140 ˚C. The change in densification within 1870–2010 ˚C is attributed to the presence of oxide layer which helps in precipitation of B_4C through liquid B_2O_3 or due to evaporation and condensation of rapidly-evolving oxide gases. Slower densification rate at temperatures above 2010 ˚C is attributed to evaporation of B_2O_3 and condensation of B_4C.

Densification of boron carbide without deterioration of mechanical properties, especially high hardness, is a very challenging task. Many researchers have been working in processing of B_4C and they proposed that densification can be improved either by using a suitable sintering aid and/or advanced techniques of sintering in presence of pressure. Selection of the additive and the method of consolidation are generally dictated by the end use of the product and the properties that are required. The additive by itself or due to in situ reaction with boron carbide would form a non-volatile second phase aiding in densification and properties enhancement. Hence, selection of the additive should be directed towards the formation of a suitable structure providing the correct property enhancement for final use. Recent or advanced techniques such as microwave-driven sintering (MWS), spark plasma sintering (SPS), explosive compaction, etc. help to obtain dense products without microstructural coarsening. These techniques are presently limited to laboratory scale only. A thorough literature review on the different techniques used for sintering of boron carbide is presented in the following sessions.

2-5-1- Pressureless sintering

Pressureless sintering is a simple and economic process to produce dense compacts. This operation is carried out in two steps: in the first step green compacts with sufficient handling strength are prepared by uniaxial die compaction. In a second step these green pellets are sintered at a chosen high temperature under controlled atmosphere. Sintering of B_4C powder compacts is commonly performed in an inert gas medium. But the application of vacuum helps in evaporation of the surface oxide layer and also prevents

further oxidation, thereby promoting the sintering mechanisms. Removal of the oxide layer by heating in a reducing atmosphere before sintering also has a similar effect [7].

Decrease in particle size and increase in sintering temperature (2100 to 2190 ˚C) give rise to higher final densities. Densities higher than 90% TD are achieved by sintering at a temperature above 2200 ˚C with particles size close to or smaller than 1 μm size. Grain coarsening is the common feature in compacts with high densities obtained by pressureless sintering[29-31]. Surface mass transport, which is active at temperatures below which densification can proceed, is responsible for the coarsening process. At higher temperatures, vapour phase diffusion of boron carbide is the important transport mechanism for coarsening. Rapid heating is helpful in achieving higher densities with fine microstructure, as the compacts can be heated to a temperature where densification can take place before the microstructure becomes highly coarsened. Vickers hardness and flexural strength of the pressureless sintered boron carbide samples are in the range 18– 24 GPa and 120–200 MPa respectively, which are lower than theoretical values. One can conclude that the densification of pure boron carbide with density higher than 90% TD is possible only at very high sintering temperatures of ~2300 ˚C. Such compacts have a coarse-grained microstructure with high amount of intragranular porosity and poor flexural strength [15, 29, 31, 32].

2-5-1- Hot pressing

In pressureless sintering the rate of densification is very slow. Though higher densification can be achieved at higher temperatures, it is difficult to avoid grain growth. Addition of a second phase can only retard but not completely avoid the grain growth. Pressure-assisted consolidation/sintering generally involves heating a powder compact, with the simultaneous application of pressure. The powder compacts are typically heated externally and the pressure is applied hydraulically. Hot pressing is the most common method for fabricating dense articles of pure B_4C. Without sinter additives B_4C can be fully densified by hot pressing at temperature higher than 2100 ˚C with an applied load of ≥30 MPa [7]. Densification by sintering during hot pressing results from three successive mechanisms:

1- Particle rearrangement, where both the total and open porosities decreases and the closed porosity remains constant (temperature range: 1800–1950 ˚C)

2- Plastic flow, leading to the closing of open porosity without significantly affecting the closed pores (1950–2100 ˚C)

3- Volume diffusion and pore elimination at the end of hot pressing (2100–2200 ˚C) [7].

The density, porosity and microstructure of hot pressed B_4C depend on the hot pressing parameters, such as temperature, pressure, time, heating/cooling rate, etc. Though very fine particles are not a precondition the size of boron carbide used for hot-pressing generally falls in the range 1–10 mm [16, 33-35]. The density of the compacts obtained under identical hot pressing conditions (2150 ˚C for 10 min) were 91.6 and 99.7% TD with starting powders of 3.85 and 0.35 μm respectively [7]. Properties of dense B_4C compacts prepared by hot pressing generally have the best properties with the following values: hardness, 29– 35 GPa; fracture toughness, 2.8–2.9 MPa $m^{1/2}$; elastic modulus, 450–470 GPa; flexural strength, 350 MPa; compressive strength, 1400–3400 MPa [7]. Fractography of fully dense boron carbide compact shown that mode of fracture seems to be transgranular [31].

Compacts with densities higher than that achievable by pressureless sintering process are produced by hot-pressing of boron carbide powders. The added advantages of hot pressed compacts are: a fine-grained structure, very low porosity and improved mechanical properties. For application in nuclear industry, where pure boron carbide is essential and impurities/additives cannot be tolerated, hot pressing is the preferred method to produce dense, pure compacts [7].

2-5-3- Hot isostatic pressing (HIP)

The HIP process, originally known as gas pressure bonding, uses the combination of elevated temperature and high pressure to form/densify raw materials or preformed components. The application of the pressure is carried out inside a pressure vessel, typically using an inert gas as the pressure transmitting medium with or without glass encapsulation of the part. A conventional resistance-heated furnace inside the vessel is the temperature source. Parts are loaded into the vessel and pressurization occurs usually simultaneously with the heating. The high pressure provides a driving force for material transport during sintering which allows the densification at considerably lower temperatures in comparison to those of traditional sintering. In addition to this, the high pressure induces particle rearrangement and high stresses at the particle contact points particularly during the initial stages of the process. The pressure level used in the HIP process typically is 100–300 MPa, as compared to 30–50 MPa in uniaxial hot pressing, and the isostatic mode of application of pressure is generally more efficient than the uniaxial one [36]. Larsson et al. used hot isostatic pressing for processing boron carbide at

1850 ˚C for 1 h under a pressure of 160 MPa and they obtained 97% TD[37]. The combination of pressureless sintering and post-HIP is gaining importance for fabrication of dense bodies with higher densities, lower graphite contents and significantly higher Vickers hardness than commercially hot-pressed B_4C. Boron carbide (100% TD) could be obtained by a combination of pressureless sintering and post-HIP at 2150 ˚C for 125 min under 310 MPa of argon pressure [7, 38]. Fully dense very fine-grained boron carbide has been prepared by this fabrication route: injection moulding/pressureless sintering (2175˚C)/ post-HIP (2050˚C, 200 MPa, Ar) from B_4C doped with 4 wt-% carbon black. Elimination of residual porosity and significant improvements in flexural strength, elastic constants and hardness were observed[39].

Porosity severely degrades the ballistic properties of ceramic armour as it acts as a crack initiator. Sintering aids generally degrade hardness and ballistic properties. Therefore, boron carbide protective inserts for personal armour is hot-pressed to minimize porosity (~98% relative density), yielding acceptable performance. Post-hipping of pressureless sintered boron carbide is gaining importance for this purpose[40].

2-5-4- Microwave sintering

Microwave sintering has the advantage of uniform and rapid heating since the energy sources are volumetric and heat is generated inside the sample rather than being conducted into the specimen from an external heat source. Enhanced densification and finer microstructures, not feasible in the conventional furnaces are possible through the use of microwave systems. The sample size and shape, the distribution of the microwave energy inside the cavity, and both electric and magnetic fields of the electromagnetic radiation are crucial for heating and sintering[7]. Literature on microwave sintering of boron carbide is scarce. One of the recent articles describes the behaviour of B_4C/SiC/ Al mixtures during microwave heating in air. A dense composite with B_4C-SiC skeleton and the voids filled with the reaction products of Al and B_4C were obtained. SiC was not attacked by oxygen and was able to contribute to matrix toughness. This material with low density and high hardness is attractive for use in lightweight armour[41]. One can expect more research using microwave heating when bigger size units with higher power ratings become available in the market.

2-5-5- Spark plasma sintering (SPS)

Conventional pressure-assisted consolidation techniques, such as hot-pressing, hot isostatic pressing, etc., require long processing time and high temperatures in order to

produce high density parts. SPS was based on the idea of using the plasma on electric discharge machine for sintering metal and ceramics in the early 1960s by Inoue et al.[42]. They expected that sintering assisted by plasma could help fabricating advanced materials. The SPS equipment was patented in America [43, 44].

The technique is similar to traditional hot-pressing, but in this case the sample is heated by a high-intensity, low-voltage pulsed DC electric current flowing directly through the sample (if electrically conducting) and through a die, typically made with graphite. This makes possible faster heating rates (up to 1000 ˚C/min) than those provided by traditional hot-press systems. In addition to rising Joule heating, high intensity electric currents have also been shown to produce significant modification in the reactivity in several solid-state systems. While the presence of short pulses has been suggested to produce plasma discharges enhancing the early stages of sintering, direct evidence for this has yet to be provided [45].

A schematic of the SPS apparatus is shown in Fig. 2.6. The equipment consists of a mechanical device capable of uniaxial pressure application and the electrical components to apply a pulsed and steady current. The loose powders are directly loaded into a punch and die unit. Graphite die and graphite punches are commonly used. This limits the pressure levels to low values, generally lower than 100 MPa. The graphite confinement provides a reducing sintering environment. The machines are equipped with chambers for vacuum or controlled environment. The consolidation process consists of two stages: (1) an initial activation through the application of a pulsed voltage, and (2) the subsequent heating and densification by using DC current. These stages may be applied sequentially or simultaneously. A typical pulse discharge is achieved by the application of a low voltage (approximately 10 V) and a 600–1000 A current. In SPS machines an AC current rectifier is used to achieve controlled DC pulsing. The resultant is a square wave current with equal on and off pulses. The duration of each pulse may be varied between 1 and 300 ms. In the second stage, when regular sintering takes place, the current is DC or quasi-DC at a level dependent on the powder type. The conductive powders are mainly heated by Joule effect. The pulsed current may be applied prior to or throughout the Joule heating cycle. For non-conductive powders heating occurs through heat transfer from the die and plungers. In this case the die and punches are heated as a result of their own resistance by Joule effect. Temperature measurements are carried out using either pyrometers or thermocouples. The latter are inserted in a horizontal die hole about 1–2 mm apart from the loaded powders. Throughout the process, a uniaxial pressure is applied. The

pressure may be constant or changed in the second stage. Sometimes the initial pressure level is light (approximately 10–15 MPa) and then increased during the heating stage. The sintering time is dependent on the type of powder. To determine the sintering time SPS machines are equipped with a linear gauge that monitors the powder shrinkage and shrinkage rate during densification. The shrinkage decreases continuously while the shrinkage rate has a maximum and then decreases to essentially zero. The densification is considered complete when the shrinkage rate reaches the zero value. The entire operation, from the loading of the die to the ejection of the finished part, may be accomplished in less than 1 hour.

In general, SPS results indicate accelerated densification with minimum grain coarsening while achieving a good metallurgical grain-to-grain bonding. The latter may be partly explained by the ability to remove the oxides and impurities from the particle surfaces. In general the remaining oxides on powder particles are known to cause consolidation difficulties. Sintering at high temperatures in vacuum or reducing atmospheres usually provides good interparticle bonding due to oxide decomposition. In SPS of conductive powders, oxide removal and subsequent good interparticle bonding may be attributed to phenomena ranging from resistance heating to thermal and electrical breakdown of insulating films and discharge or arc induce. In any SPS, densification starts with a highly porous body. The initial pressure application proceeds with neck formation. The neck formation is due to the geometric amplification of the pressure on the interparticle point contacts, but as the necks grow the local pressure at the necks is substantially reduced. At this stage the pulsed current is applied and a current path is established in either the metal or conductive ceramic powders. The goal is to achieve a uniform current path rather than local channels that may concentrate all the passing current. Usually, the initial 1–2 pulse applications ensure a uniform current path, particularly for high resistance powders. Next, the current is forced to choose the path of least resistance, i.e. through the contact points to complete the current path through powders. However for non-conductive powders, there are conflicting viewpoints about the presence of plasma or other type of surface effect due to electric field activation, even there is not any experimental verification for conductive powders to assess these phenomena [46, 47].

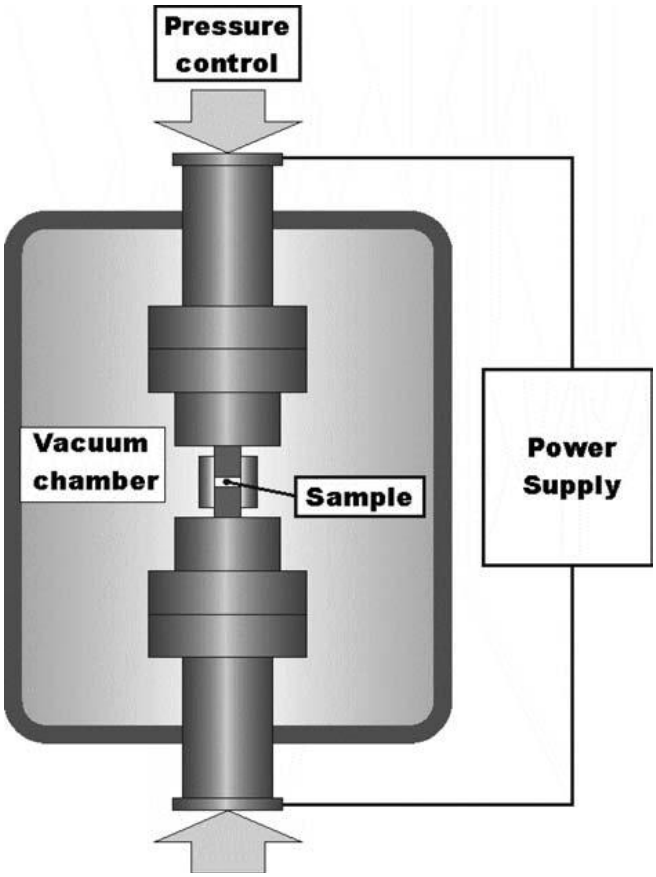

Fig. 2.6. Schematic of the SPS process[47].

In the last few years, few attempts for fabricating fully dense pure, B_4C specimens have been carried out by means of SPS or similar techniques [13, 14, 48]. Ghosh et al.[13] have consolidated micrometer-sized boron carbide at 1750 ˚C by the application of a compression stress equal to 88 MPa for 2 and 5 min by means of plasma pressure compaction. The densities were 96 and 99.2% theoretical density with the average grain size in between 1.6 μm and 2 μm, respectively. A fully-dense boron carbide was attained by Hayun et al.[14, 48] at 2050 ˚C for 10 min under an applied compression stress equal to 32 MPa. They observed a homogeneous distribution of fine equiaxed grains 4.05 μm average size. No unexpectedly enhanced grain growth was reported. Sairam et al. obtained fully dense boron carbide by SPS at1800 ˚C for 15 min under applied compression stress equal to 50 MPa[49]. In all cases, improvements in mechanical properties, especially in hardness, are reported[13, 14, 49].

2-5-6- Role of sinter additives

Various sinter additives have been tested to increase the rate of densification, control grain growth and improve mechanical properties of boron carbide especially from point of view of fracture toughness and strength. Although those sintering aids can increase

the specific density of boron carbide, hardness normally drops and there are many doubts about improvement of ductility and fracture toughness [50]. In the following sessions, brief review on different additives used for sintering of boron carbide is presented.

2-5-6-1- Carbon

Carbon has been found to be very effective, primarily in reducing the oxide layer of the boron carbide powders, thereby promoting sintering and hindering grain growth. Carbon, well distributed between the particles, reacts with the B_2O_3 coating according to the reaction:

$$2B_2O_3+6C=B_4C+6CO \quad (2.5)$$

Removal of oxide layer allows direct contact between B_4C particles, permitting sintering to initiate at significantly lower temperature (~1350 ˚C). In addition, carbon at the grain boundaries enhances diffusion, facilitating accelerated solid-state sintering. Any carbon which is not consumed by the reduction reaction is left in the compact as excess carbon[7, 51]. Carbon additive greatly enhances the sintering kinetics in pressureless sintering. Such an effect is not expected in the case of hot pressing as the sintering mechanisms are different [7].

2-5-6-2- Carbide/boride additives

Addition of carbides and borides have been found to increase the flexural strength and fracture toughness of B_4C by grain refinement and crack propagation influencing mechanisms such as crack deflection, micro crack interaction and crack impediment. Carbides/borides can either be directly added or formed by in situ reaction with B_4C while sintering. The ideal second phase, in addition to maintaining chemical compatibility, should be present in amounts of 10 to 20 vol.%. Greater amounts may diminish the toughness increase due to overlapping particles. Addition of various transition metal (TM:Ti, Zr, Hf, V, Nb, W and Ta) carbides/borides for preparing dense boron carbide pellets have been studied[52-55]. Boron carbide is reacted at approximately 1500 ˚C with the transition metal oxide/carbide to form a mixture of boron carbide+metallic carbide/boride (equation 6 or 7), which is sintered at temperatures >2000 ˚C in pressureless sintering or at temperatures ≥1800 ˚C in hot pressing or spark plasma sintering .

$$B_4C+2TMO_2+3C=2MB_2+4CO\uparrow \quad (2.6)$$

$$B_4C+2TMC=3C+2MB_2 \quad (2.7)$$

The improved mechanical properties are attributed to the presence of a fine distribution of secondary phase particles in the matrix. If the second phase is not as hard as boron carbide, the presence of a large volume of it is likely to deteriorate the mechanical properties of B_4C[53, 56-58]. Goldstein et al. have studied the reaction between B_4C and MeO mixtures (MeO: TiO_2, ZrO_2, V_2O_5, Cr_2O_3, Y_2O_3 and La_2O_3) fired up to 2180 ˚C for 2 h in argon. The main solid reaction products are found to be borides[56].

B_4C–15 vol.-%TiB_2 composite with a flexural strength of 621 MPa and fracture toughness of 6.1 MPa $m^{1/2}$ have been prepared by hot pressing at 2000 ˚C and a pressure of 20 MPa in argon atmosphere for 1 h by Skorokhod et al.[59] They have observed that factors for an increased strength are mainly: the healing of the cracks during sintering and the presence of TiB_2 particles which force the crack to propagate in a non-planar way, thus enhancing the energy dissipation at the crack tip.

S.G. Huang et al.[60] obtained fully dense B_4C–TiB_2 composites by SPS for 4 min at 2000 ◦C with application of an external pressure equal to 60MPa. Microstructural analysis showed that B_4C and TiB_2 grain growth was substantially suppressed due to the pinning effect of the secondary phase and the rapid sintering cycle, resulting in micrometer-sized and homogeneous microstructures. Excellent properties were obtained for the 60 vol% TiB_2 composites, combining a Vickers hardness of 29 GPa, a fracture toughness of 4.5MPam$^{1/2}$ and a flexural strength of 867 MPa.

2-5-6-3- Liquid phase sintering

Liquid phase sintering is carried out either by the addition of a substance with low melting point or by the formation of a low melting substance by in situ reaction of the additive with boron carbide. Wettability, capillary action, dissolution and reprecipitation are the important parameters, which determine the sintering feasibility and the mechanical properties. The most important additives for liquid phase sintered-B_4C are Si and Al. Although the sinterability can be significantly improved, normally the toughness remains low and the hardness drops sharply[61, 62]. In the case of Al, the wettability of B_4C is found to be strongly depend on temperature and the formation of different reaction products such as $Al_{2.1}B_{51}C_8$, Al_3BC, AlB_2, $Al_3B_{48}C_2$ at the interface are reported [63-65].

Silicon, with a melting point of 1410 ˚C, acts as a liquid sinter additive when added to boron carbide and in addition reacts with carbon of boron carbide to form silicon carbide, thus helping the sintering process and also strengthening the matrix. Silicon carbide has attractive properties, similar to that of boron carbide such as high hardness

(28 GPa), low specific gravity (3.1 g cm^{-3}) and good wear resistance and hence considered an attractive sinter addition to boron carbide[58]. The process to get this implies infiltration of silicon into a porous body of boron carbide and then sinterization in the temperature range 1500–2200 ˚C. As a result of this, dense non-porous boron carbide body, consisting of normal B_4C, together with second boron carbide-type having an expanded lattice and alpha and beta silicon carbides and silicon are achieved. The presence of unreacted, free silicon degrades the mechanical properties of such reaction-bonded B_4C [58, 61, 62].

Another option if the addition of alumina, which improves the densification of boron carbide through the formation of a liquid phase of $AlB_{12}C_2$ by reaction between B_4C and Al_2O_3 [66, 67]. It has been reported that B_4C can react with Al_2O_3 and free C by the following chemical reaction:

$$6B_4C + Al_2O_3 + C = 2AlB_{12}C_2 + 3CO \quad (2.8)$$

$AlB_{12}C_2$ will be in a molten state at 1900 ˚C, which may contribute to the enhanced densification rate of the B_4C matrix ceramic composites[66, 67].

2-6- Creep deformation mechanisms

Creep of materials is classically associated with time-dependent plasticity under a fixed stress at an elevated temperature, often greater than roughly 0.5 Tm, where Tm is the absolute melting temperature. The plasticity under these conditions is described in Fig. 2.7 for constant stress (a) and constant strain-rate (b) conditions. Several aspects of the curve in Fig. 2.7 require explanation. First, three regions are delineated: Stage I, or primary creep, which denotes that portion where the creep-rate (plastic strain-rate), $\dot{\varepsilon} = d\varepsilon/dt$ is changing with increasing plastic strain or time. In Fig. 2.7(a) the primary creep-rate decreases with increasing strain. Often (in pure metals) the strain-rate decreases or the stress increases to a value that is constant over a range of strain. The phenomenon is termed Stage II, secondary, or steady-state (ss) creep. Eventually, cavitation and/or cracking increase the apparent strain-rate or decrease the flow stress. This regime is termed Stage III, or tertiary creep, and leads to fracture [68].

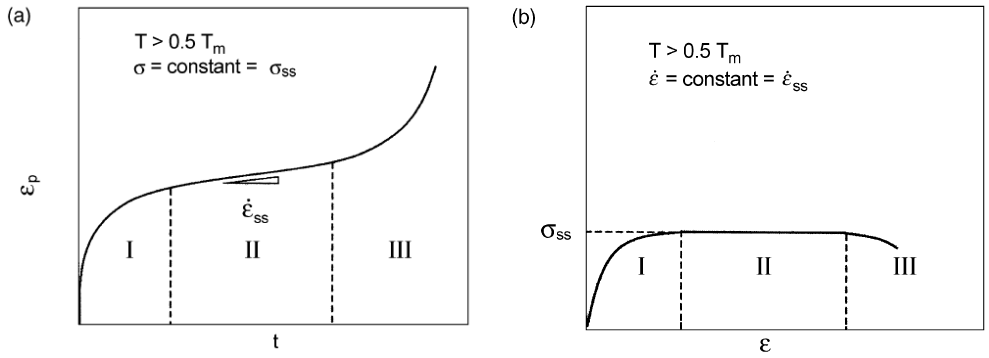

Fig. 2.7. Constant true stress (a) and constant strain rate (b) creep behaviour [68]

The relationship between the applied stress and the steady-state creep-rate is phenomenologically described by:

$$\dot{\varepsilon} = \mathrm{A}\ \frac{\mathrm{Gb}}{\mathrm{kT}}\left(\frac{\mathrm{b}}{\mathrm{d}}\right)^{p}\left(\frac{\sigma}{G}\right)^{n} D \tag{2.9}$$

where $\dot{\varepsilon}$ is the strain rate, A the dimensionless constant, G the shear modulus, b the magnitude of the Burgers vector, k the Boltzmann`s constant, T the absolute temperature, d the grain size, p the invers grain size exponent, σ the stress, n the stress exponent and D the appropriate coefficient given by:

$$D = D_0 \exp\left(-\frac{Q_c}{RT}\right) \tag{2.10}$$

where D_0 is the pre-exponential factor, which contains a frequency factor, Q_c is the activation energy of the mechanism controlling creep and R is the gas constant[69]. As shown in Fig. 2.8 for a given temperature, the variation in the steady-state creep-rate with the applied stress is often described by the steady-state stress exponent, n, defined by:

$$\mathrm{n} = \left[\delta \ln \dot{\varepsilon}_{\mathrm{ss}} / \delta \ln \sigma_{\mathrm{ss}}\right]_T = \left(\ln \frac{\dot{\varepsilon}_2}{\dot{\varepsilon}_1}\right) \Big/ \left(\ln \frac{\sigma_{ss2}}{\sigma_{ss1}}\right) \tag{2.11}$$

The activation energy for steady-state creep, Q_c, simply describes the change in (steady state) creep-rate versus temperature for a given substructure, at a fixed applied "stress". The activation energy for creep, Q_c, can be defined by

$$Q_c = -\mathrm{k}\left[\delta\left(\ln \dot{\varepsilon}_{\mathrm{ss}}\right) / \delta\left(1/T\right)\right]_{\sigma_{ss}} \approx -k\left(\frac{\ln \dfrac{\dot{\varepsilon}_1}{\dot{\varepsilon}_2}}{\dfrac{1}{T_1} - \dfrac{1}{T_2}}\right) \tag{2.12}$$

Three discrete mechanisms can occur at the atomic level during creep deformation: grain boundary sliding accommodated by grain shape changing, dislocation slip and

diffusional creep. These three mechanisms can either occur independently of one another to some approximation, or be accommodated by each other.

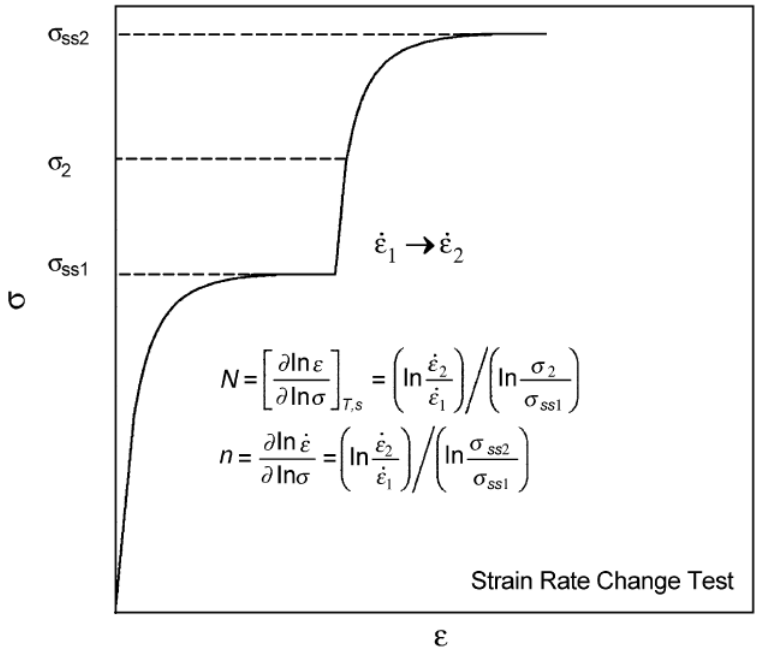

Fig. 2.8. A graphical description of the constant strain rate and the steady state stress exponent,n [68].

2-6-1- Grain boundary sliding

Grain boundary sliding is the most commonly considered mechanism for superplastic flow. The microscopic mechanism responsible for superplastic deformation is still not thoroughly understood. One of the most spectacular observations of superplasticity is perhaps that reported by Pearson in 1934 of a Bi-Sn alloy that underwent nearly 2000% elongation[70]. He also claimed then, for the first time, the grain boundary sliding was the main deformation mechanism responsible for superplastic deformation[70]. It is essential to be accompanied by an accommodation mechanism for GBS. Otherwise, premature fracture will occur due to the extensive cavitation, especially near the triple junctions. The accommodation mechanism may include grain-boundary migration, recrystallization, diffusional flow or slip. The accommodation process is generally believed to be the rate-controlling mechanism[68, 71].

Over the years a large number of models have emerged in which the accommodation process is either diffusional flow or dislocation movement. The best known model for GBS accommodated by diffusional flow, depicted schematically in Fig.2.9, was proposed by Ashby and Verral[72]. This model explains the experimentally observed

switching of equiaxed grains throughout deformation. It is based on a topological mechanism for GB sliding followed by accommodation by atomic diffusion along the boundaries. This model predicts a linear stress dependence of the strain rate (n=1) and a threshold stress for GB sliding that depends on the interfacial boundary energy. According to this model:

$$\dot{\varepsilon}_{ss} = \mathrm{K}(\mathrm{b}/g)^2 D_{eff}\left(\sigma - \sigma_{THs}/E\right) \tag{2.13}$$

where $D_{eff} = D_{sd}9\left[1+(3.3w/g)(D_{gb}/D_{sd})\right]$, K is a constant, σ_{THS} is the so-called threshold stress and w is the grain boundary width. The threshold stress arises since there is an increase in boundary area during grain switching when clusters of grains move from the initial position

(Figure 2.9(a)) to the intermediate one (Figure 2.9(b)).

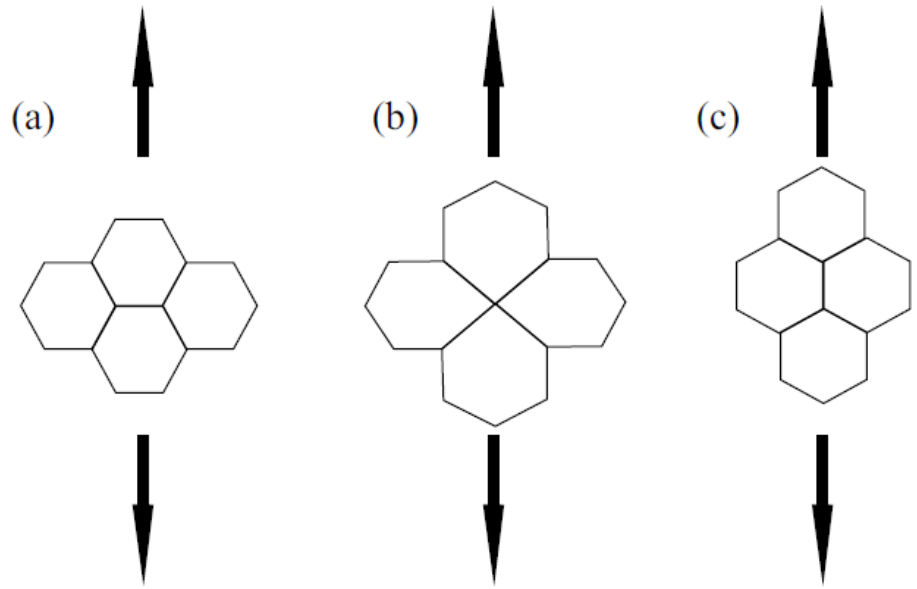

Fig. 2.9. Ahby-Verral model of GBS accommodated by diffusional flow[72].

Rearrangement proposed by Ashby–Verral cannot occur purely by diffusional flow, and the diffusion paths were reported to be physically incorrect. For this reason, researchers again focused on the first model of GBS that was proposed by Ball and Hutchison[73], in which GBS is generally modeled assuming sliding is accommodated by the movement of extrinsic dislocations along the grain boundary. Dislocation pile-ups at grain boundary ledges or triple points may lead to stress concentrations. In order to avoid extensive cavity growth, GBS must be aided by an accommodation mechanism (Fig. 2.10). The latter must ensure rearrangement of grains during deformation in order to achieve strain compatibility and relieve any stress concentrations resulting from GBS. Stress concentration at triple points is relieved by the generation and movement of

dislocations within the grains. Later, in an improved model by Gifkins (referencia), accommodation process also consists of dislocation movement which only occurs in the "mantle" region of the grains, i.e., in the region close to the grain boundary (Fig. 2.11). According to all these GBS's models n = 2 in a relationship such as:

$$\dot{\varepsilon}_{ss} = K(b/d)^p D(\sigma/E)^2 \qquad (2.14)$$

where p = 2 or 3 depending on whether the dislocations move within the lattice or along the grain boundaries, respectively. K is a constant, which varies from a model to another, and the diffusion coefficient, D, can be D_{sd}, or D_{gb}, depending on whether the dislocations move within the lattice or along the grain boundaries to accommodate stress concentrations from GBS[68, 74].

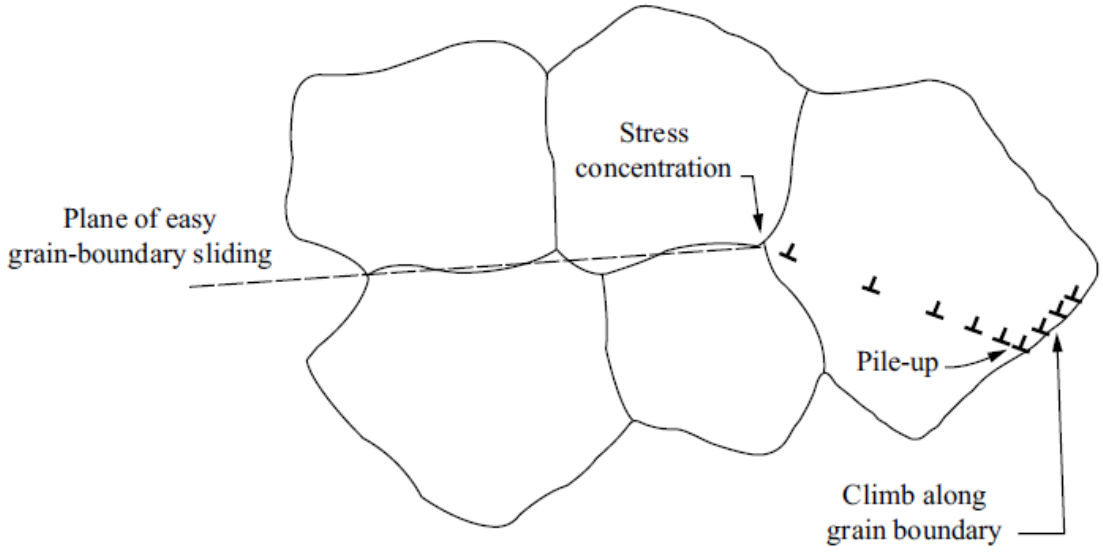

Fig. 2.10. Ball-Hutchinson model of GBS accommodated by dislocation movment[73].

Artz *et al.* further developed an improved model in which it is admitted that grain migration is controlled by the mobility of evenly-spaced GB dislocations. The mobility of these dislocations is severely limited by the dragging effect of solutes present in the grain boundaries. Assuming that the dislocation density is proportional to the flow stress, the modified creep equation yields two new features: the stress exponent decreases from n=2 at low stresses to n=1 with increasing stress while the grain-size exponent increases from p=1 to p=2[75]. However, in most nonmetallic systems, including ceramics, dislocation activity requires very high applied stresses, which are well above the experimentally recorded ones. The lack of understanding for superplasticity in ceramics resulted in the development of a new model by Gomez-Garcia et al. (referencia) that accounts for the occurrence of superplasticity in the absence of

dislocation motion. It is based on a mechanism of grain-boundary sliding by pure-shear motion under stationary conditions, which is accommodated by lattice or grain-boundary diffusion. A key element of this model is the central role of grain curvature as the driving force for grain sliding. Assuming that grain boundaries are dislocation free, it describes a mechanism of grain-boundary sliding accommodated by diffusion, which can explain the values of the stress exponent, especially the value n=2, and its possible stress and temperature dependences[76].

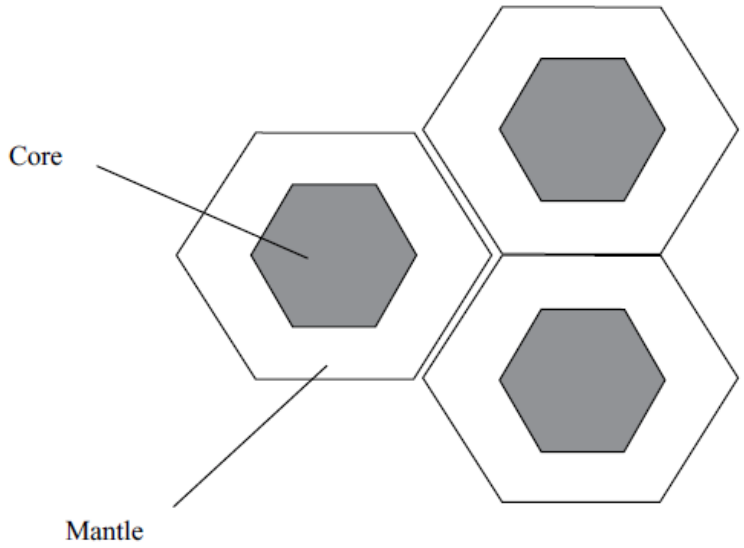

Fig. 2.11. Gifkins ¨core and mantel¨ model[74].

2-6-2-Dislocation creep or power-law creep (PL)

Dislocation creep is associated to dislocation motion in the grain lattice during deformation, which involves both glide-controlled creep and climb-controlled creep.

Climb-controlled creep refers to the process of climb by non-conservative dislocation motion over physical obstacles. This is usually found in pure metals or Class M alloys (again, similar behavior to pure metals) in which creep follows the typical behaviour **depicted** in Fig. 2.7. Stage I, or primary creep, occurs when the material experiences hardening through changes in the dislocation substructure. Eventually Stage II, or secondary, or steady-state creep, is observed. In this region, hardening is balanced by dynamic recovery (e.g., dislocation annihilation). Here, a moving dislocation is held up by an obstacle on its slip plane. The applied stress is less than that needed to overcome the obstacle via dislocation glide alone. However, the dislocation can climb by

diffusional processes to a parallel slip plane. The climb process permits the dislocation to glide onto a new plane until it encounters another obstacle and the process repeats itself. Since glide and climb are sequential processes, the climb creep is determined by climb velocity which is less than the glide velocity. Dislocation substructure forms from dislocation reactions and also as a consequence of dynamic recovery process. The consequence of this is that the creep-rate or plastic strain-rate is constant under constant true stress (tension, compression or torsion). Since Stage II or steady-state creep is important, the creep behavior of a material is often described by the early steady-state creep plots. The stress exponent n usually measured is around 5. In more general terms, the creep rate equation can be expressed by:

$$\dot{\varepsilon}_{ss} = KD_L\left(\sigma^n/G\right) \tag{2.15}$$

where D_L is the lattice diffusion coefficient, E is shear modulus . Here the n exponent is not precisely five but it is constant over a range of temperatures, stresses and strain-rates, and falls within the range of 4–7 observed in pure metals and class M alloys (ceramics may have exponents less than the range). This range has been conveniently termed "five power". Some have referred to the Five-Power-Law Creep as "dislocation climb controlled creep"[68, 77-79].

When the temperature decreases below roughly 0.5–0.6 T_m or at higher stresses, n continually increases and Qc generally decreases until the power-law-breakdown (PLB) occurs. Within PLB, creep is dislocation climb controlled, but Q_c corresponds to the activation energy for dislocation-pipe diffusion. Vacancy supersaturation resulting from deformation, associated with moving dislocations with jogs, could explain this decrease in the values of Q with decreasing temperature (increasing stress) and still be consistent with dislocation climb control. Dislocation glide mechanisms may be important and the rate-controlling mechanism for plasticity in PLB is still speculative. But observation of very well-defined subgrain boundaries formed from dislocation reaction (perhaps as a consequence of the dynamic recovery process), suggests that substantial dislocation climb is at least occurring in PLB[68].

Glide-controlled creep refers to the process of glide of dislocations on slip planes. This mechanism occurs mainly because solute atoms impede dislocation motion. Such kind of alloys are called Class I solid solutions. The mechanism of deformation in viscous glide of dislocation is due to the fact that the dislocations interact in several possible ways with the solute atoms, and their movement is impeded. There are two competing mechanisms over this stress range, dislocation climb and glide, and glide is slower and

thus rate controlling. Weertman[80] has suggested a possible explanation for this relationship that it follows naturally from equation:

$$\dot{\varepsilon} = 1/2\,\bar{v} b \rho_m \tag{2.16}$$

where $\bar{v}$ is the average dislocation velocity and ρ_m is the mobile dislocation density. It has been theoretically suggested that $\bar{v}$ is proportional to σ for solute drag viscous glide. Moreover, Friedel proved that $\sigma^2 \propto \rho_m$ which leads to $\dot{\varepsilon} \propto \sigma^3$ or 3-power behavior in equation 2.16. More precisely, following the original model of Weertman[80], Viscous Glide Creep is described by the equation:

$$\dot{\varepsilon}_{ss} = K D_s \left(\sigma^3 / G\right) \tag{2.17}$$

where D_s is the diffusion coefficient of the solute atoms in the alloy. Typical stress exponents measured in Class I solid solutions are clustered around 3, defining the so-called Three-Power-Law viscous glide creep.

At low temperatures the solute atoms are immobile; thus, their effect is an increase of the flow stress owing to the enhanced value of the stress required for dislocations to move through them. At higher temperatures, solute atoms are mobile. Thus, if the dislocation velocity is not too high, the solute atoms move together with edge dislocations, acting as a ¨drag¨ on their motion. Solute drag creep takes place when the solute atoms and dislocations move in a cooperative way. Dislocation velocity increases with the applied stress and, when the stress level becomes sufficiently high, the dislocations ¨breakaway¨ from the cloud of solute atoms. Once dislocation is released the stress decreases and so does the dislocation velocity. The lower velocity permits the solute atoms to concentrate and oversaturate the dislocation cores, thus the flow stress increases rapidly. Therefore stress again attains a value sufficiently high to induce breakaway, the process repeats itself and serrated flow can be observed in the stress-strain curves. The phenomenon is called the Portevin-Le Chatelier effect. The Portevin-Le Chatelier effect is found only over a limited range of strain rates. For example, if the strain rate is sufficiently high, the flow stress is always greater than the breakaway stress and serrated flow is not found [68, 77, 80, 81].

2.6.3 Diffusional creep

Non-dislocation based diffusional creep occurs at high temperatures (T≈Tm) and very low stresses in fine-grained materials due to the transport of matter by diffusion. It was qualitatively suggested 50 years ago by Nabarro. This was rigorously (quantitatively) proposed and described by Herring. Mass transport of vacancies through the grains from

one grain boundary to another was described as follows: Excess vacancies are created at grain boundaries perpendicular to the tensile axis with a uniaxial tensile stress. The concentration may be calculated using:

$$c = c_v\left[\exp\left(\frac{\sigma\Omega}{kT}\right)-1\right] \tag{2.18}$$

where c_v is the equilibrium concentration of vacancies, Ω is atomic volume and the activation energy for vacancy formation is altered by $\pm\sigma\Omega$ that $\pm$ signs refer to compressive and tensile regions, respectively. Usually $\left(\frac{\sigma\Omega}{kT}\right)>>1$, and therefore equation (2.18) can be approximated by:

$$c = c_v\left[\left(\frac{\sigma\Omega}{kT}\right)\right] \tag{2.19}$$

These excess vacancies diffuse from the grain boundaries lying normal to the tensile direction toward those parallel to it, as illustrated in Fig. 2.12. Grain boundaries act as perfect sources and sinks for vacancies. Thus, grains would elongate without dislocation slip or climb. The excess concentration of vacancies per unit volume is, then, $(c_v\sigma/kT)$. If the linear dimension of a grain is "d", the concentration gradient is $(c_v\sigma/kTd)$. The steady-state flux of excess vacancies can be expressed as $(c_v\sigma\Omega/kTd)D_v$, where D_v is the effective diffusion coefficient of vacancies. The resulting strain-rate is given by:

$$\dot{\varepsilon}_{ss} = \frac{D_v\sigma\Omega}{kTd^2} \tag{2.20}$$

As it is shown in Fig. 2.12 (b), changes in grain shape happen as a result of matter arrangement by diffusional flow. It is important to realize that this process does not guarantee the integrity of the polycrystal unless sliding of adjacent grains occurs to avoid cavitation. This is the Liftshitz mechanism for diffusional creep accommodation.[68, 77, 82].

In 1963, Coble proposed a controlled grain-boundary diffusion creep mechanism. He suggested that, at lower temperatures (T<0.7 Tm), the contribution of grain-boundary diffusion is larger than that of self-diffusion through the grains.

Thus, diffusion of vacancies along grain boundaries controls creep. Diffusion path through the grain boundary is proportional to δ/d, where δ is an effective grain boundary thickness for mass transport. The strain-rate suggested by Coble is:

$$\dot{\varepsilon}_{ss} = \frac{D_{gb}\sigma\Omega}{kTd^2}\frac{\pi\delta}{d} \tag{2.21}$$

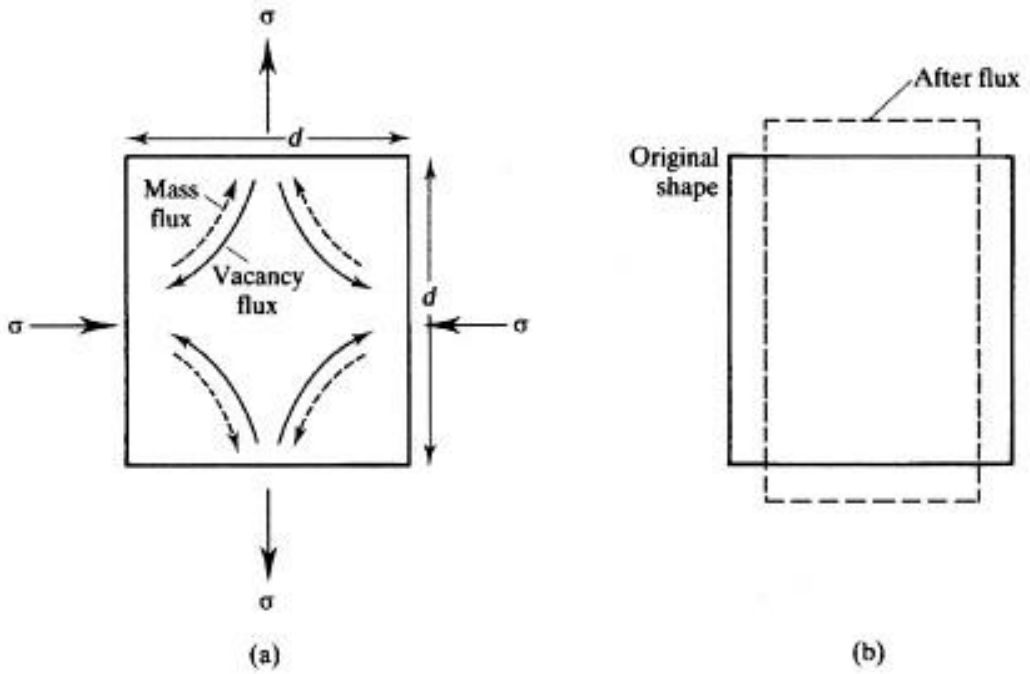

Fig. 2.12. Nabarro-Herring of diffusional flow[77].

where D_{gb} is the diffusion coefficient along grain boundaries. Thus, contrary to the d^{-2} dependence exhibited by the Nabarro–Herring model, a d^{-3} is pointed out as more accurate one in the Coble model. Also, the activation energy for Nabarro-Herring creep is found to be greater than that for Coble creep[68, 77, 82].

In both Nabarro- Herring and Coble creep models, strain rate has a linear dependency with stress. Normally theses two mechanisms activated simultaneously. Therefore, the general strain rate for diffusional creep is given by[77]:

$$\dot{\varepsilon} = \frac{A\Omega\sigma}{kTd^2}\left(\frac{\pi\delta}{d}D_{gb} + D_l\right) \tag{2.22}$$

To sum-up, the main creep models invoked in literature has been briefly revisited. Other models have been proposed, but most of them make use of different features of the models commented above or they are a combination of both of them. We will show that the accurate analysis of boron carbide demands a return of the basics of dislocation creep to account for the effects and twinning and the dislocation-twin interaction. That will one of the central aspects of the discussion chapter.

Chapter III: Experimental procedure.

3-1- Starting materials

In the first part of study, commercially boron carbide powders (Grade HD20, H. C. Starck, Germany) with average particle size around 500 nm were used as the starting material. The morphology of the powders is shown in Fig. 3.1. According to the specification provided by the supplier (see Table. 3.1), there is some amount of impurities, mainly silicon (0.15 wt%) and iron (0.05 wt%).

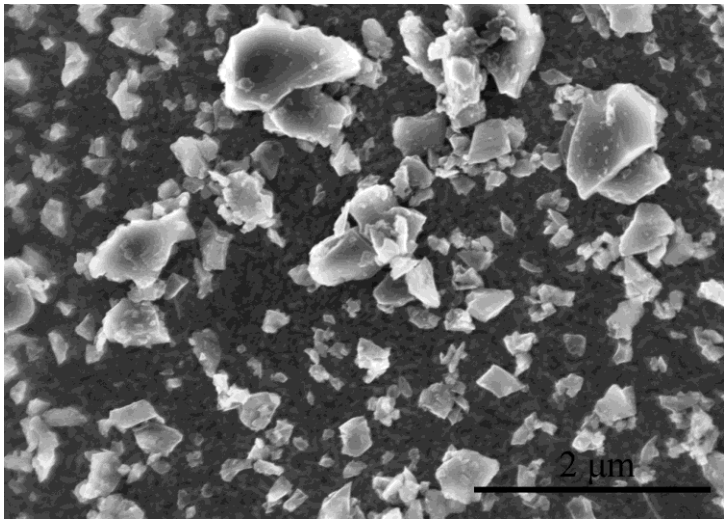

Fig. 3.1. SEM micrograph of an as-received boron carbide provided by H. C. Starck, Germany.

Table. 3.1. Characteristics of an as-received boron carbide provided by H. C. Starck, Germany.

Specific surface area	22-27 m^2/g
Impurity levels	Max
N	0.7 wt%
O	2.6 wt%
Si	0.15 wt%
Fe	0.1 wt%
Al	0.05 wt%
Other (Ca, Cr, Mg, Mn, Ni, Ti, W)	0.1 wt%
Total carbon	Min 21.8 wt%
B:C ratio	3.7-3.9

In the second part, to prepare an ultrafine B_4C, as-received powders were subjected to high-energy ball-milling in a shaker mill (Spex D8000, Spex CertiPrep, USA) operated at about 1060 back-and-forth cycles per minute. The high-energy ball-milling was carried out under ambient conditions for 180 min in cylindrical hardened-steel

containers with WC balls (6.7 mm in diameter; Union Process Inc., USA) at a ball-to-powder volume ratio of ~8:1 and in inert atmosphere of ultrahigh purity Ar to prevent the occurrence of oxidation during milling. The inert atmosphere was achieved by performing the loading of the balls and powders into the containers in a glovebox (CaptairPyramid, Erlab, UK) filled with ultrahigh purity Ar, which had been previously purged twice. In addition, to minimize the powder contamination during milling a first milling cycle was carried out as described above to cover the surface of the container and of the balls with a thin film of B_4C, and the resulting powder was thrown away. Next, the milling cycle was repeated utilizing the same container and balls, using the resulting powder mixtures for the rest of the study. This approach has already proven to be effective in the shaker milling of other hard ceramics[83, 84] with less than 1 wt.% contamination by WC.

In the following part in order to improve the mechanical properties of boron carbide specially fracture toughness, two kinds of composites with addition of SiC and SiC plus graphite were prepared and studied. For this aim, available powders of submicrometric B_4C from H.C. Starck and submicrometric β-SiC (~0.5 μm; Ultrafine, Ibiden Corp., Japan), and micrometric graphite (>2 μm; Synthetic, Sigma–Aldrich, Spain) were used. Two powder batches were prepared with different compositions, one of which contains B_4C with 15 wt.% SiC, and the other B4C with 15 wt.% SiC and 2 wt.% graphite. SiC was added as a potential sintering additive and enhancer of the mechanical properties, whereas graphite was added as possible process-control agent and/or sintering additive. The powder mixtures were subjected to high-energy ball-milling in a shaker mill (as explained before) operated at about 1060 back-and-forth cycles per minute. Here, the high-energy ball-milling was carried out for 180 min in cylindrical hardened-steel containers with WC balls (6.7 mm in diameter) under a ball-to-powder volume ratio of ~2:1, and in inert atmosphere of ultrahigh purity Ar.

In the last part of study, commercially nano boron carbide powders with high purity (Tekna Plasma system Inc., Canada) with average particle size from 40-80 nm were used as the starting material. The morphology of the powders is shown in Fig. 3.2.

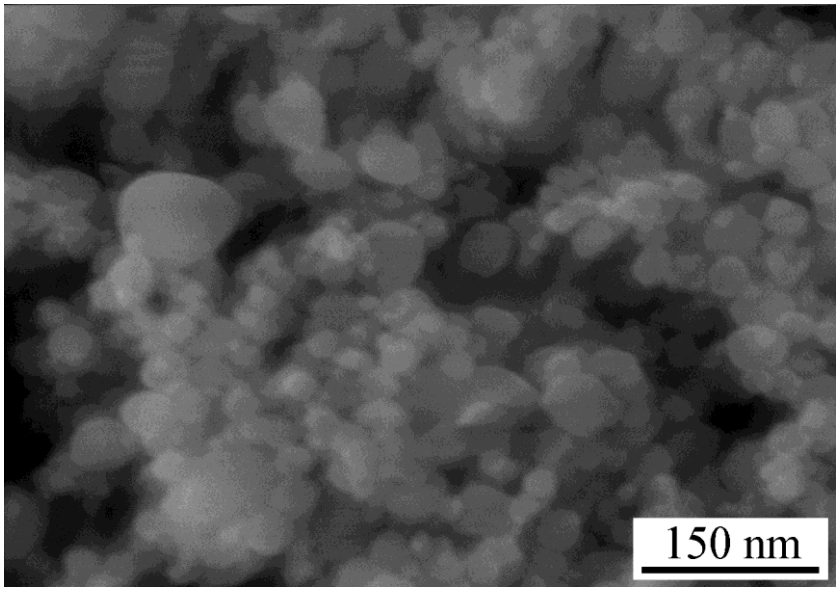

Fig. 3.2. HR-SEM micrograph of an as-received nano-boron carbide provided by Tekna Plasma system Inc., Canada.

3-2- Powder processing

3-2-1-Pre-annealing of powders

It will be described in following chapter that in some cases especially in milled boron carbide and nano-boron carbide, B_4C powder has poor sinterability. This was attributed to the presence of extra B_2O_3 on the surface of the B_4C nanocrystals, which is known to favour coarsening over densification[85, 86]. In order to enhance sinterability of boron carbide in theses special cases, annealing at temperatures higher than 1000˚C (heating and cooling ramps of 5˚C/min) for 8 h in a tubular furnace (TermoLAb TH1700,Portugal) under a flowing atmosphere of ultrahigh purity Ar, was performed. This kind of heat-treatment has already proven to be effective for the elimination of the B_2O_3 impurities in other boride ceramics[87]; the basis is that B_2O_3 melts at ~510˚C and experiences significant evaporation beyond 1000˚C[17], so that even in the absence of chemical reactions the B_2O_3 surface impurities can be removed through the phase-change reaction $B_2O_3(l) \rightarrow B_2O_3(g)$.

3-2-2- Densification by Spark Plasma Sintering (SPS)

All different kinds of powders were consolidated under vacuum in a SPS device (Dr. Sinter 515S, Kanagawa, Japan). The unit consisted of a sample chamber with hydraulic rams, graphite spacers, graphite die and punch (Fig 3.3), power unit, water cooling circuit, control module, and computer data acquisition unit (Fig. 3.4). The data acquired

during the SPS process included time, temperature, current, voltage, and displacement. In all experiments, B_4C powder was loaded into 15-mm diameter graphite dies lined with graphite foil and surrounded by a 1 cm thick graphite blanket to minimize heat loss, and then spark-plasma sintered in a dynamic vacuum (i.e., ~6 Pa) at peak temperatures in the range 1500–1800˚C (as measured by an optical pyrometer focused on the die), with soaking times in the interval 1–9 min, heating ramps of 100 or 200˚C/min, and uniaxial pressure of 75 MPa (applied during the first minute of heating). The conditions of all experiments by SPS are provided in chapter IV.

The applied electrical power is delivered by the SPS in rapid pulses, 3.3 ms in length. The applied voltage is in the range 0–10 V, while the current can be as high as 2000 A in our system. The pulses are delivered in groups of up to 99 consecutive pulses, followed by 1–9 missing pulses. The sequence represents the pulse pattern. In the present work a pulse pattern of 12:2 (12 pulses on and 2 off) was always used.

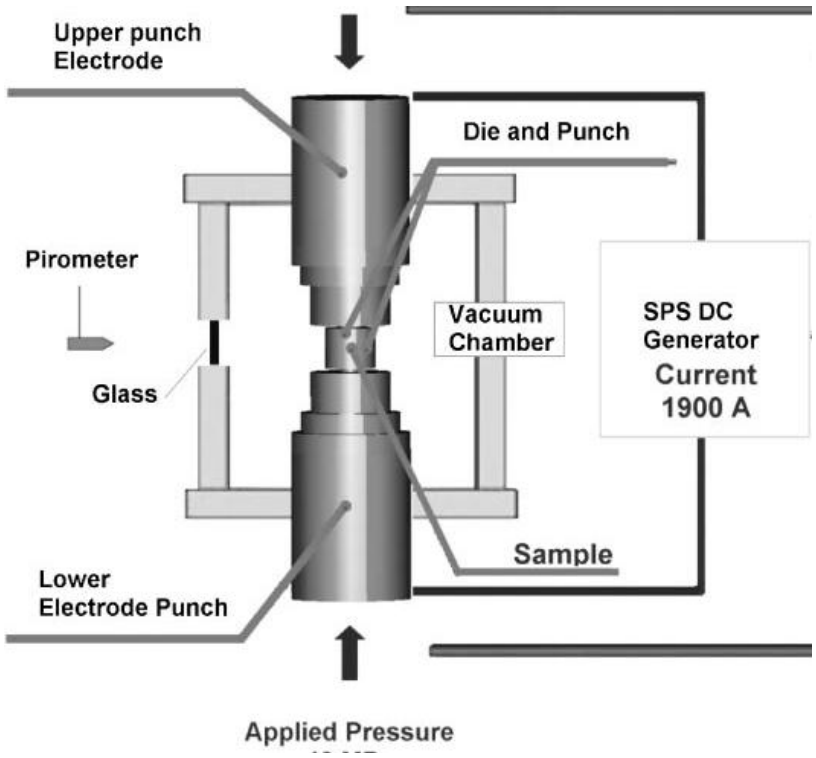

Fig. 3.3. Schematic of SPS apparatus.

Fig. 3.4. Spark plasma sintering machine.

3-3- Characterization after SPS consolidation

3-3-1- Density measurement

The density of sintered samples was measured by distilled water displacement technique (Archimedes method). According to the Archimedean Principle, a solid body immersed in a liquid apparently loses as much of its own weight as the weight of the liquid that it has displaced. This makes it possible to determine the unknown value. For this propose, B_4C samples were first weighed while in air, and then while immersed. And from the two weightings (made in grams), density ρ was calculated by Equation 3.1:

$$\rho = \frac{W_d}{W_d - W_{sub}} \times \rho_0 \qquad (3.1)$$

Where ρ [g/cm^3] is the density of the sintered samples, ρ_0 is the density of distilled water at room temperature, W_d [g] is the weight of samples in air (dry weight) and W_{sub} [g] is the weight when immersed in distilled water. Hence (W_d-W_{sub}) equals the buoyancy in grams.

3-3-2- X-ray diffraction

X-ray bulk diffraction (XRD) of the samples was carried out by X-ray diffractometry (XRD; D8 Discover, Bruker, Germany) to analyze the structural changes of sintered samples. Diffraction patterns were recorded using Cu Kα radiation over a 2θ range of 10–90◦ and a position-sensitive detector using a step size of 0.05˚ on the polished cross-

section surface of samples. In order to determine the crystallographic data and accurate compositions of sintered samples in different conditions, Rietveld refinement was performed. In this study, we used the version 3.5d of the Rietveld analysis software FULLPROF[88], assuming the pseudo-Voigt function to describe the peak shapes. The refinement protocol included the background, the scale factors, and the global-instrumental, lattice, profile and texture parameters.

3-3-3- X-ray photoemission spectroscopy

X-ray photoemission spectroscopy (XPS K-Alpha, Thermo Scientific, UK) was performed for determining composition based on the photoelectric effect. This technique is on base of using monochromatic (X-ray) incident beam which the energy of an incident photon (hv) is transferred to a bound electron. If the energy of the photon is greater than the binding energy of the electron and the electron has enough energy to overcome the work function (Φ) of the solid, it can leave the solid (Fig. 3.5). Due to the emission of the electron, the inner shell of the atom is ionized. The energy conservation requires:

$$KE = h\nu - BE - \Phi \qquad (3.2)$$

where BE is the binding energy relative to the Fermi level E_F and KE is the kinetic energy of the photoelectron (relative to the vacuum level E_V). The photoelectron spectrum is given by the kinetic energy distribution of the photoelectron measured with an electron analyzer. For known photon energy (hv) the binding energy can be determinate for all core electrons with Eq. 3.2. Since each element has unique set of core levels, KE's can be used to fingerprint element

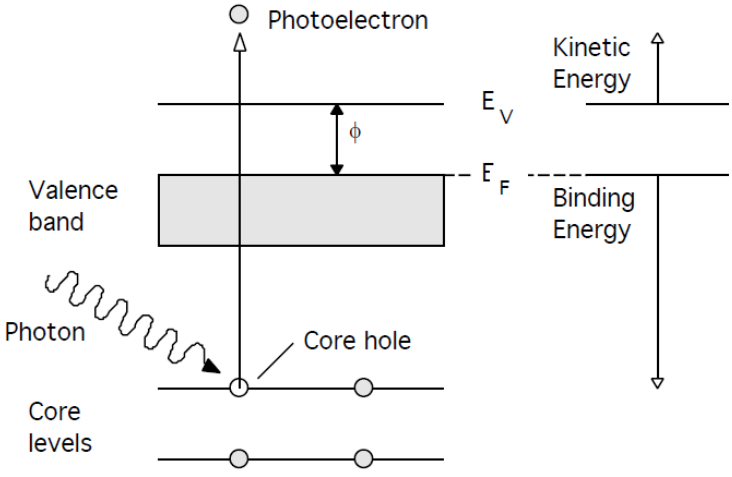

Fig. 3.5. Schematic representation of the photoemission.

This is powerful technique for chemical analysis means elemental identification and chemical state of element and also relative composition of the constituents in the surface region. Therefore is complementary technique for determining composition especially when it is less than to be detected by XRD or distinguishing the composition of amorphous phase that is not possible by XRD.

In this study the main goal of using XPS was determining the amount of glassy phase of boron oxide in as-received powder and some sintered samples. For this aim, the XPS spectrum of the B 1s core line was recorded in ultra-high vacuum(10^{-6}Pa) in the 180–196 eV range at 0.1 eV energy resolution using a monochromatic Al-Kα X-ray source (1486.6 eV), and was indexed using common databases, the purpose here being to identify the bonding environments or statuses.

3-3-4- Raman spectroscopy

Raman spectrometer equipped with a dispersive microscope (Horiva Jobin Yvon LabRam HR800) was used for analysing crystal structure of sintered samples especially determination of subsurface damage beneath the indentation from mechanical Vicker test(See. 3-5-1) for analyzing possible phase changes. Raman spectra provide information on the vibrational modes of molecules and, therefore, determine change in atomic structure of damaged sample from Vickers test compare with undamaged sample. Raman spectra were recorded with a 20 mW He–Ne green laser (532.14 nm), without filter and with a 600 g/mm grating. The microscope used a 50× objective and a confocal pinhole of 100 μm. The Raman spectrometer was calibrated using a silicon wafer.

In simple words, Raman spectroscopy is a spectroscopic technique based on inelastic scattering of monochromatic light, usually from a laser source. The Raman effect occurs when light impinges upon a molecule and interacts with the electron cloud and the bond of that molecule. For the spontaneous Raman effect, which is a form of light scattering, a photon excites the molecule from the ground state to a virtual energy state. When the molecule relaxes it emits a photon and it returns to a different rotational or vibrational state that it means inelastic scattering. The difference in energy between the original state and this new state leads to a shift in the emitted photon's frequency away from the excitation wavelength. Since vibrational information is specific to the chemical bonds and symmetry of molecules, therefore, it provides a

fingerprint by which the molecule can be identified. Also changes in chemical bonding in individual composition can be easily determined with this technique.

3-4- Microstuctural observation

3-4-1- Scanning Electronic Microscope (SEM) and High-Resolution Scanning Electronic Microscope (HR-SEM)

Microstructural analysis was performed on both fractured and polished surfaces of all the sintered and deformed (See 3-6) samples by Scanning Electron Microscopy (Philips XL30, The Netherlands) and High-Resolution Scanning Electron Microscopy (HR-SEM; S5200, Hitachi, Japan) for sub-micrometric and ultra fine microstructures samples, respectively. In the required cases X-ray energy dispersive spectrometry (XEDS) which is coupled to SEM was used for chemical determination of different observed grains. For observing polished surface (1-μm finish using routine ceramographic method), electro-chemically etching with a solution of 1% KOH is necessary. The average grain size was determined from the SEM images. For this aim, the grain diameter was defined as that of the equivalent circle as a follows:

$$D = 2\sqrt{\frac{Area}{\pi}} \tag{3.3}$$

3-4-2- Transmission Electronic Microscope (TEM)

TEM observation was performed by means of a Hitachi H800 or Philips CM-200 microscope operated at 200 kV in order to microstructural evolution in the scale of individual grains especially after deformation test (See. 3-6). For TEM, slices from the sintered sample before and after creep test were prepared using conventional TEM-specimen-preparation methods. All foils were mechanically ground to a thickness of about 100 μm and polished with diamond paste of grain size 3 μm. They were then dimpled to ~30 μm (Dimpler grinder Gatan Model-656) and ion beam thinned to electron transparency (PIPS Gatan Model-691).

3-5- Mechanical properties at room temperature

3-5-1- Vickers Hardness

Hardness was measured by the Vickers indentation test. In the materials community Vickers hardness in general is used for measuring hardness, however it can be used for fracture toughness measurements. The widely accepted definition in hardness testing is

to use the actual area of contact of the four faces of the indenter pyramid leading to a definition of Vickers hardness:

$$H = 2P/a^2 \qquad (3.4)$$

where 2a is the length of the diagonal of the hardness indent and P is applied load (See Fig. 3.6).

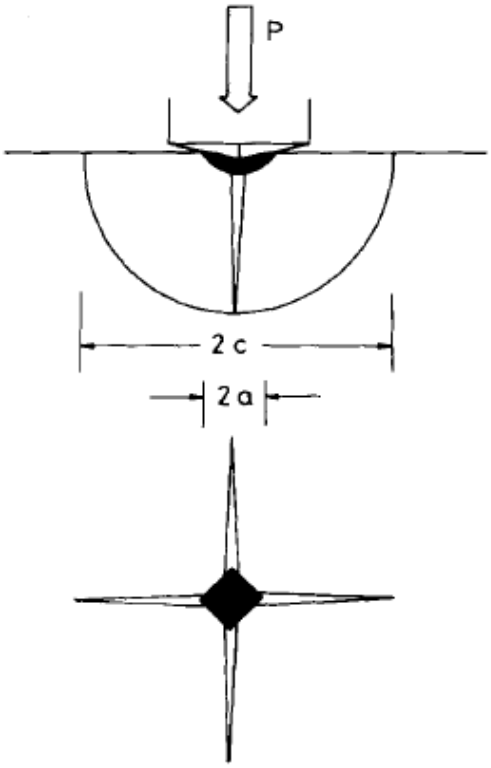

Fig. 3.6. Schematic of Vickers-produced indentation-fracture system, peak load *P*, showing characteristic dimensions C and a of radial-median crack and hardness impression, respectively[89].

In this study, polished cross-section of sintered samples were cut along the diameter of the disc-shaped discs and were indented at several locations (minimum 10 indentations per specimen) under a load (P) of 9.81 N using a hardness tester (Struers A/S, DK-2750 Bullerup, Denmark) equipped with a Vickers diamond pyramid. Diagonal lengths of Vickers imprint (2a) were measured by optical microscopy.

3-5-2- Fracture toughness base on Vickers hardness

Cracks extending from the corners of the Vickers indentations were used for fracture toughness (K_{IC}) measurements. This idea, first proposed in the late 1970´s to estimate the fracture toughness of ceramic materials base on measuring the lengths of cracks emanating from Vickers indents by Lawn et al.[90]. The method has subsequently

received much recent attention for making measurements of fracture toughness in different materials. However, accurately measuring the fracture toughness of brittle materials can often be challenging. On the other hand, creating sharp pre-cracks for measuring toughness in hard ceramics can be difficult without catastrophically failing the specimen, while fracture toughness data using notched specimens can give erroneously high values. Such tests on base of Vickers hardness can be relatively quick and easy to perform, require little specialized equipment, and can allow probing of localized microstructural features. Accordingly, such techniques are finding considerable usage in studying the fracture behavior of hard and brittle materials[90, 91].

Numerous empirical fracture toughness relations are available in literature depending on the nature of the crack systems [92]. It should be mentioned that the way of calculating the fracture toughness is determined by the crack pattern, i.e., either according to a radial/median (half-penny cracks)[90] or Palmkvist crack[93, 94] mode. The radial-median (half-penny) cracks are usually observed on the brittle materials with very limited plasticityand low fracture toughness like ceramics and glasses as well as the high-indentation load when the crack easily propagates along the surface and into the bulk of the specimen. This half-penny crack is characterized by relatively high ratio of the crack length C to the half-diagonal of the indent C/a≥3 (Fig. 3.7). A number of models for the radial-median crack geometry are suggested that can be in a general form:

$$K_{IC}^{\text{Half-penny}} = \beta.(E/H)^{n}.P.C^{-3/2} \qquad (3.5)$$

where β and n are dimensionless experimental factor and power constants, that is equal to 0.016 and 0.5, respectively according to Lawn et.al.[89, 90] and E is the Young modulus. The dimensionless factor $(E/H)^{n}$ in Eq. (3.5) accounts for the effects of the residual stresses beneath the hardness indentation.

Another crack system, so-called Palmqvist cracks, however, have been found at low values of *c/a*. Such cracks begin only at the end of the diagonals of the indentation, as illustrated in Fig. 3. 7. In this mode, four independent elongated semielliptical cracks are created with relatively low ratio of the length (L) to the half-diagonal (a) of the indent 0.25≤L/a≤2.5. According to this model fracture toughness can be estimated as a following:

$$K_{IC}^{\text{Palmkvist}} = 0.0122(E/H)^{2/5}\, P/aL^{1/2} \qquad (3.6)$$

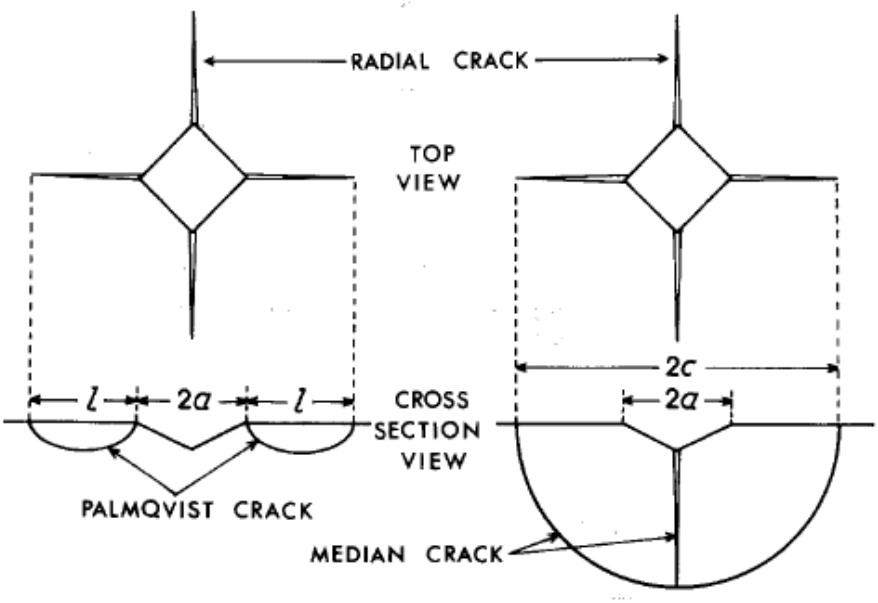

Fig. 3.7. Comparison of geometries of Palmqvist and median cracks around Vickers indentation[93].

Each kind of the crack systems results in the different values for K_{IC}. In order to identify the type of crack an additional, post-indentation, polishing is required. The gap in-between the edge of the polished indentation and the actual crack reveals a Palmqvist crack mode [48, 66]. In the current study, the indented surfaces were additionally polished for few minutes with 3 μm diamond paste and no gap appeared after the subsequent polishing on the indented surfaces that resulted in a half-penny crack system beneath the indentations. The fracture toughness can therefore be calculated according to Eq. 3.5. Recently Lee et.al.[15] and Ghosh et.al.[13] used a similar fracture toughness equation based on a half-penny crack system to calculate K_{IC} for boron carbide. For this aim, crack length (C) extending from the corners of the Vickers indentations were measured by optical microscopy.

3-6-High-temperature mechanical properties

Evaluation of mechanical properties or plastic deformation of ceramics at high temperatures can be performed by means of two different types of deformation tests. One of them is a compression test at constant load which is well-known as a creep test and the other one is a compression test at constant strain rate (cross-head speed) that results in the conventional stress-strain curve. Both cases can be used for determining the mechanical behaviour of ceramics at high temperatures. Data are rationalized in terms of the high-temperature creep equation introduced in section 2-6 (Eq. 2.9). As mentioned there, in this equation stress exponent (n) and activation energy (Q) are

important parameters that determined the creep mechanism of materials at high temperature. According to Eq. 2.11, stress exponent (n) can be easily calculated by jumps in stress at constant temperature in the case of compression test at constant load, while for compression test at constant strain rate is obtained by change of strain rate at constant temperature. Activation energy (see Eq. 2.12) can be calculated by means of temperature changes while the stress or strain rate is kept constant in compression test at constant load or at constant strain rate, respectively.

In this study, compression test at constant load was used for evaluating of deformation mechanism of boron carbide ceramics. All the experiments were carried out in one prototype machine which is shown in Fig. 3.8. The required sample for this test is small parallelepipeds of dimensions 2.5 mm × 2.5 mm × 5.0mm that is located between two cylinders made of SiC surrounded by heating elements of tungsten in the center of the chamber (Fig. 3.9). Upper SiC cylinder or piston is fixed while the lower one is mobile. Required load can be applied by equivalent weight with the factor 0.1 on a plate attached via a lever system to the lower piston on the sample.

The tests were performed at different range of temperatures under argon. To minimize oxidation several cycles of vacuum followed by introduction of argon at room temperature have been done. These cycles are repeated again at 500 ° C to remove the products of the possible degassing of the elements inside the chamber. To avoid possible buckling of the samples with SiC pistons, sample have been sandviched between SiC pads (Fig. 3.10). In this typical test, change in the length of the sample was recorded versus the time. With known original length, real strain can be calculated:

$$\varepsilon(t) = \ln\left(\frac{l_0}{l(t)}\right) = \ln\left(\frac{l_0}{l_0 - \Delta l(t)}\right) \tag{3.7}$$

where l_0 is the original length, l(t) is length at each time and $\Delta l(t)$ is change in the length with time . Then the strain rate will be:

$$\dot{\varepsilon} = \frac{d\varepsilon}{dt} \approx \frac{\Delta\varepsilon}{\Delta t} \tag{3.8}$$

Therefore, the typical creep curve of strain rate versus strain can be drawn. Also real stress can be calculated as a following:

$$\sigma(\mathrm{t}) = \frac{F}{S(t)} \tag{3.9}$$

where F is applied load and S(t) is surface of sample perpendicular of applied stress at each time. Considering that volume of sample is constant:

$$S_0.l_0 = S(t).l(t) \tag{3.10}$$

where S_0 is original surface.According to Eq. 3.9 and 3.10, real stress can be obtained:

$$\sigma(t) = \frac{F}{S_0 e^{\varepsilon(t)}} = \sigma_{eng} e^{-\varepsilon(t)} \tag{3.11}$$

Fig. 3.8. The prototype creep machine used in this study.

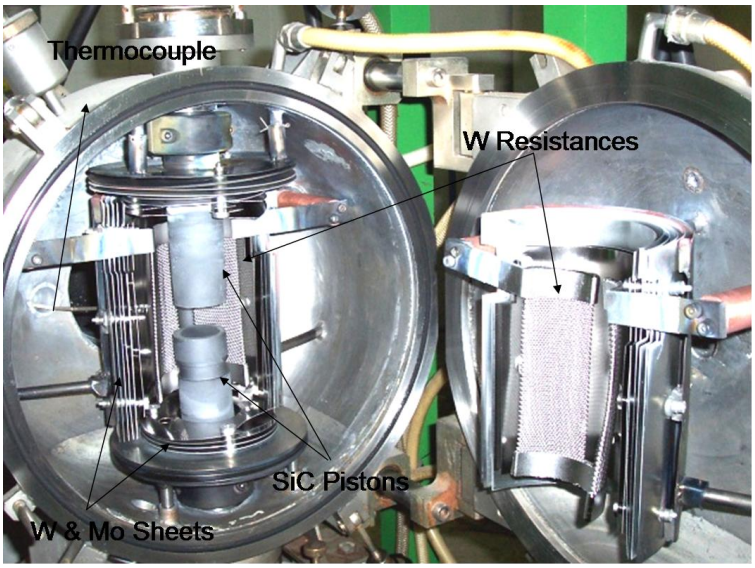

Fig. 3.9. Experimental set-up inside the heating chamber of the creep machine

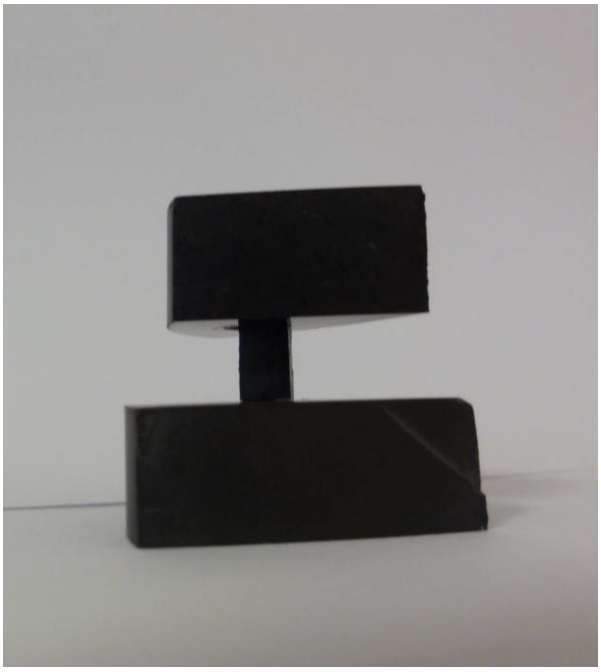

Fig. 3.10. A usual prepared sample between SiC pads for creep test.

Chapter IV: Results

4- Introduction

In this chapter, at first the processing condition of boron carbide by spark plasma sintering (SPS) was studied. To this end, several B_4C samples have been sintered with use of sub-micrometric boron carbide powder, high energy ball milled boron carbide powder and and finally nano-boron carbidepowders. Two type of composites based on boron carbide containing SiC and SiC plus graphite have been prepared by SPS, as well. Later on best samples (more dense with finer grain size) of each one have been mechanically characterized by Vickers indentation and creep tests.

4-1- As-received sub-micrometric boron carbide powder (H. C. Starck)

4-1-1- Processing by SPS and characterization

Table 4.1 shows sintering condition in SPS and the experimental density in sintered samples. Boron carbide sintered at 1600 ˚C for 5 min attained 90.3% the theoretical density. On increasing the sintering temperature to 1650 ˚C, a significant improvement in density was observed. When the sintering temperature is equal or higher than 1700 ˚C and the holding time is at least equal or longer than 3 min the samples display full density. In all cases several graphite thin foils were located between the powder and the punches.

Table 4.1. Processing condition in SPS for sintering sub-micrometric boron carbide powder

Sample No.	Temperature (°C)	Time (min)	Pressure (MPa)	Relative density (%)
1	1800	3	75	100
2	1750	3	75	100
3	1700	5	75	100
4	1700	3	75	100
5	1700	0	75	98.2
6	1650	10	75	97.6
7	1650	5	75	96.8
8	1600	5	75	90.3

Rietveld refinements corresponding to the samples sintered at 1700 ˚C for 3 min and at 1800 ˚C for 3 min are provided in Fig. 4.1. a and b, respectively. The crystallographic results after iterative fitting for these two samples are displayed in Table 4.2. According to this, the crystallographic structure fits into a space symmetry group $R\bar{3}m$. The structure is described in terms of icosahedra located at the vertices of a rhombohedral lattice. These icosahedra are linked together along the (1 1 1) rhombohedral axis by 3-atom chains. Two types of sites are possible within a single icosahedron. The polar sites

are those associated to atoms that link the icosahedra together and are one half of all the sites available within an individual icosahedral [4, 8].

The results show that two slightly different structures account for Rietveld analysis depending upon the sintering condition. For SPS-ed sample at 1700 ˚C, the structure fits into a model of $B_{11}C$ icosahedra with 3-atom chains. The chains can be either CBC-type or CBB-one, with a statistical ratio given in Table 4.2. In order to discard any possible effect of texture on the samples, the existence of effects of texture was supposed to exist. The Rietveld analysis derived from this assumption points out results with a much worse fitting to experimental data. On the contrary, for SPS-ed specimens at 1800 ˚C, the structure fits into a model of predominant $B_{10}C_2$ icosahedra (80%) rather than $B_{11}C$ one (20%). Furthermore, 4% vacancies are found in the chain centers. The possible effects of texture are also completely discarded. In this sintering condition, the lattice parameters are expanded and there are some changes in composition which is slightly different from B_4C (20%C) structure consists of $B_{11}C$ icosahedra and C-B-C chains .In addition to that, there is evidence of 6H-SiC phase present in small amount in both samples. The amount of this phase is estimated to be 0.10± 0.03 wt%. Such phase is very possibly the consequence of the residual presence of silicon present in the original powder. The presence of silicon in B_4C is a common fact[1]. The peak related to residual carbon amount is coming essentially from the graphite foils (Table 4.2). The carbon content is smaller than the amount reported in samples in which amorphous carbon is added to facilitate sintering[7]. It could not be detected the presence of any other contaminants by XRD tests or through microscopy analysis. This is in good agreement with the achievements by Hayun et al.[48] who observed clean surfaces and no secondary phases produced by residual impurities. In order to assess this statement, EDX was performed in a scanning electron microscope. The results are in full agreement with those achieved by XRD analysis, showing no presence or other contaminants rather than silicon. The crystallographic structure of boron carbide shows a large variability although the phase is the same. The role of this subtle change on the lattice on the physical properties, particularly on electric conductivity, should deserve further investigation in future.

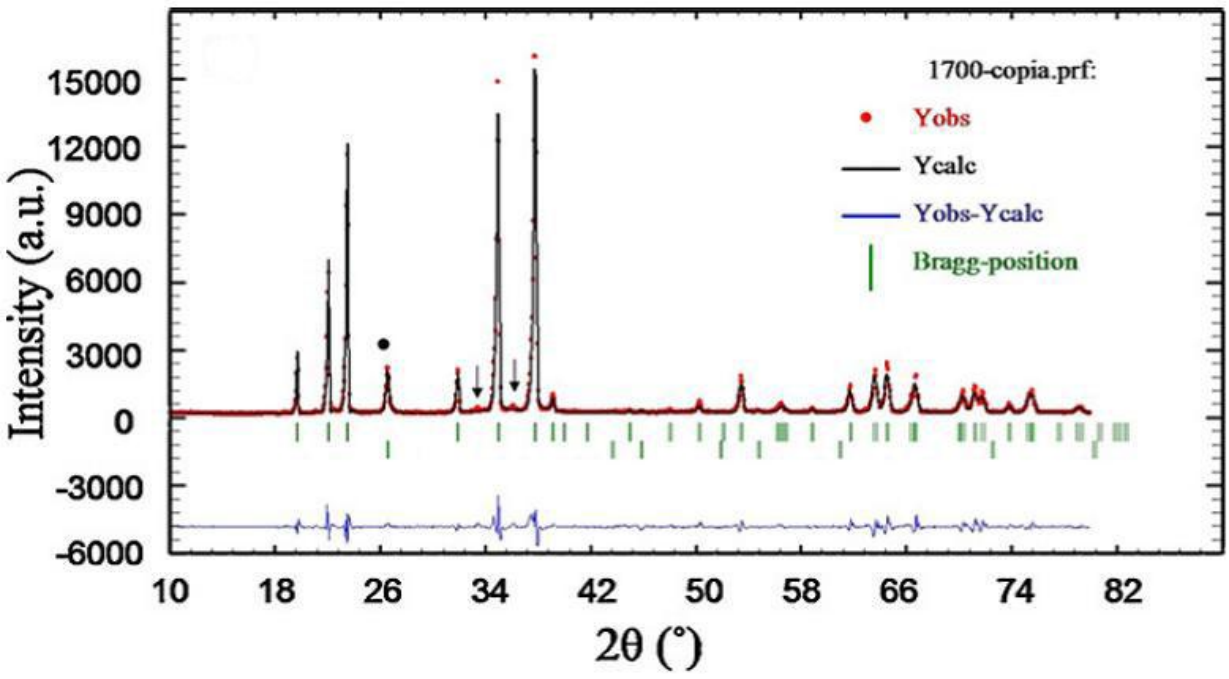

(a)

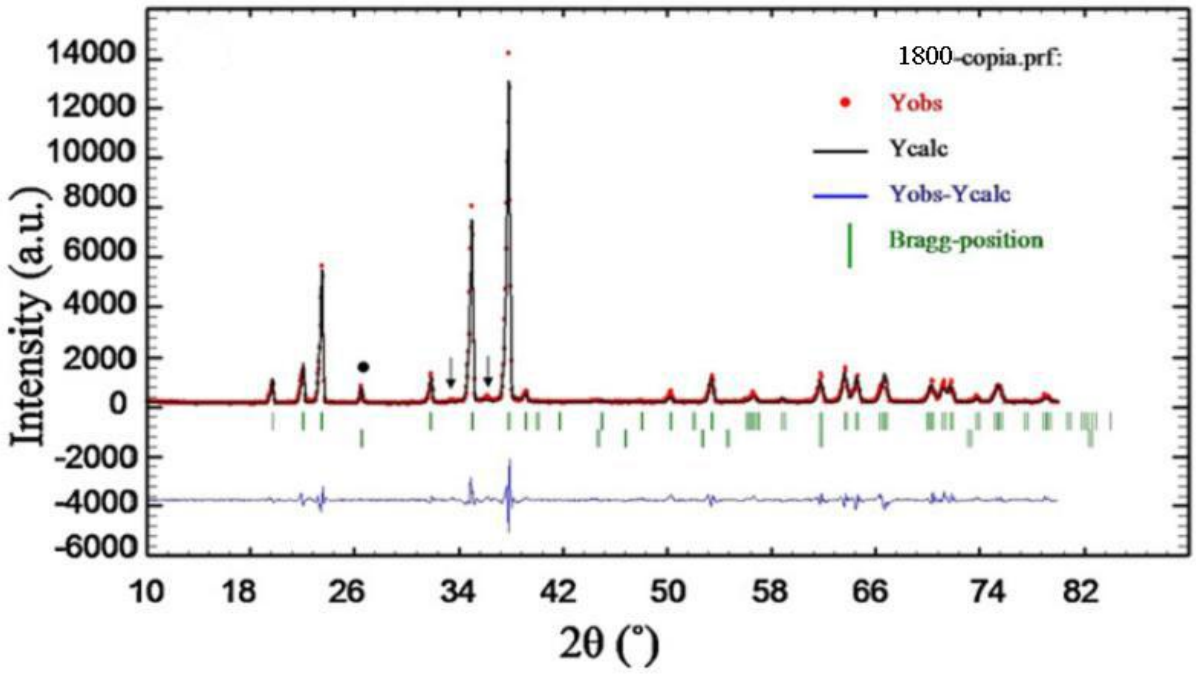

(b)

Fig.4.1. Rietveld refined XRD data for sintered sample at 1700 ˚C for 3 min (a) and sintered sample at 1800 ˚C for 3 min (b).

Table. 4.2. Rietveld refinement of a SPS-ed specimen at 1700 ˚C for 3 min compared with SPS-ed specimen at 1800 ˚C for 3 min.

	Sintered at 1700 ◦C for 3 min	Sintered at 1800 ◦C for 3 min (Enhanced grain growth)
Space group	$R\bar{3}m$	$R\bar{3}m$
Lattice parameters	a=5.593 (1) Å c= 12.061 (2) Å	a=5.607 (1) Å c= 12.096 (2) Å
Density	2.574 gcm^{-3}	2.524 gcm^{-3}
Occupancy probability (*f*)	Non-polar position B1 0.98(2) C1 0.02(1) Polar position B2 0.85(4) C2 0.15(3) Chain positions: Center B3 1.00 C3 0.00 Extremes B4 0.05(2) C4 0.95(4)	Non-polar position B1 1.00 C1 0.00 Polar position B2 0.70(2) C2 0.30(2) Chain positions: Center B3 0.83(3) C3 0.13(3) Extremes B4 0.48(2) C4 0.52(2)
Comments	Almost all icosahedra are $B_{11}C$-type. The chains are: CBC (90%) and CBB (9.8%).	80% icosahedra are $B_{10}C_2$-type and 20% are $B_{11}C$-CBC. (4% vacancies in chain centers)
Residual graphite	1.61wt%	0.59wt%

The cross-sectional microstructure of both polished and electrolytically etched specimens are displayed in Fig. 4.2. As reported elsewhere[13, 48], darker regions in the micrographs of fully dense samples, originates from the sample preparation procedure (polishing and etching) and it is caused by the pull-out of the fine particles. The improvement in density (or decrease in porosity level) with an increase in temperature is clearly evident from these SEM micrographs (comparing Fig. 4.2d with e). The fully dense samples were considered for further study of the grain size distribution and average grain size. SEM micrographs showed irregular (non-equiaxed) fine-grain microstructure with average grain sizes around 0.69, 0.81 and 0.88 μm for samples SPS-ed at 1700 ˚C for 3 (Fig. 4.2d) and 5 min (Fig. 4.2c) and 1750 ˚C for 3 min (Fig. 4.2b), respectively. An enhanced grain growth was observed in the sample SPS-ed at 1800 ˚C (Fig. 4.2a) for 3 min with average size of 51 μm, and also showed the presence of high concentrations of twins in relatively large B_4C grains. This result is consistent with previous works in literature [31, 65, 95].

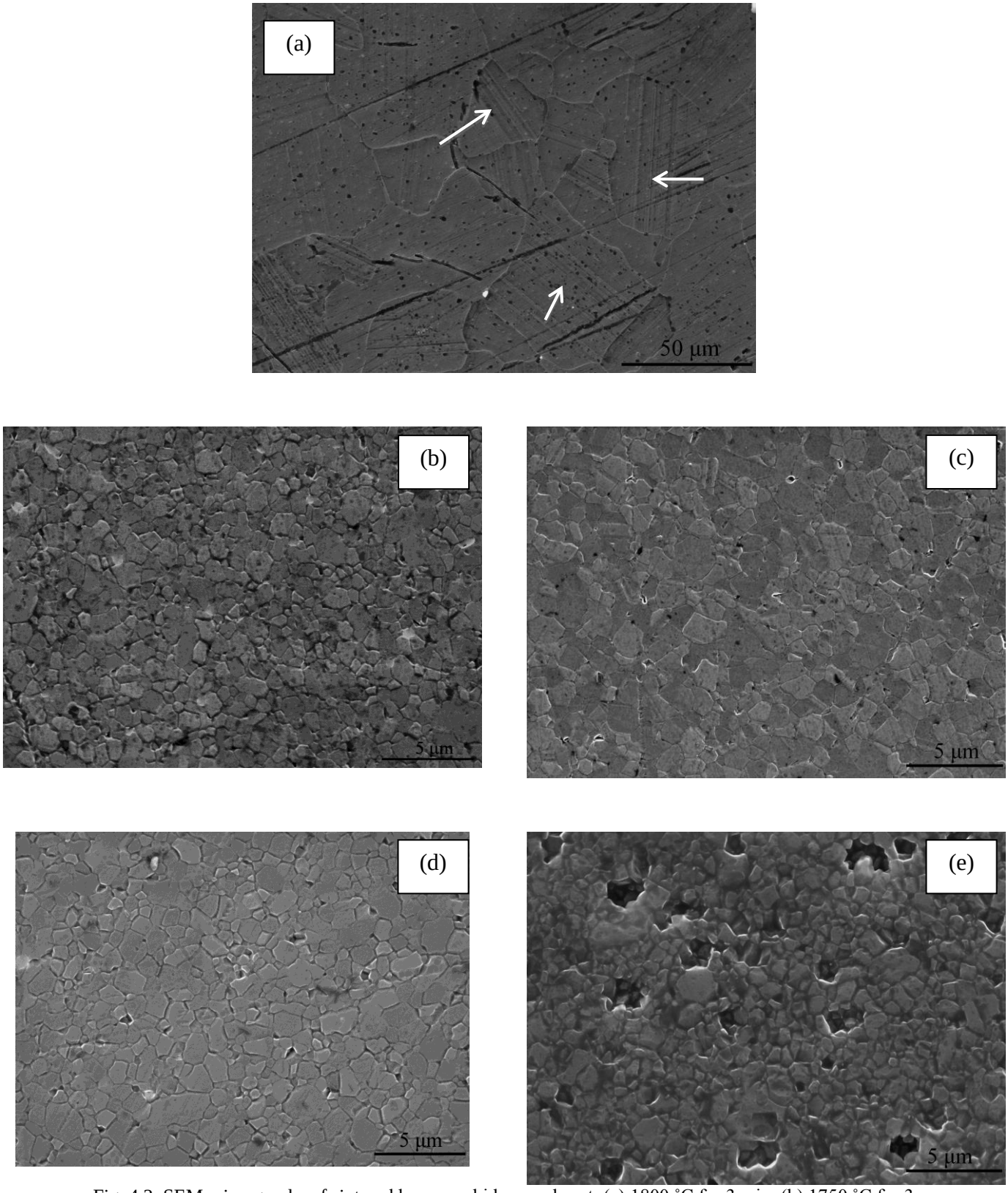

Fig. 4.2. SEM micrographs of sintered boron carbide samples at: (a) 1800 ˚C for 3 min, (b) 1750 ˚C for 3 min, (c) 1700 ˚C for 5 min, (d) 1700 ˚C for 3 min and (e) 1650 ˚C for 10 min. White arrows show twinning.

According to our results, fully-dense, fine-grained specimens can be prepared from initial powders with an average size equal to 500 nm, provided that temperatures as high as 1700 ˚C. Such temperature is significantly lower than those considered in previous

works[13, 48, 61]. However, grain growth seems to be inhibited at 1700 ˚C, while it is sharply enhanced in sample sintered at 1800 ˚C for 3 (See Table. 4.3).

Microstructure of fully dense specimen with smallest grain size (sintered at 1700 ˚C for 3 min) was more studied by TEM as shown in Fig. 4.3. The main feature is the presence of fine twinning in small grain that can not be observed by SEM.

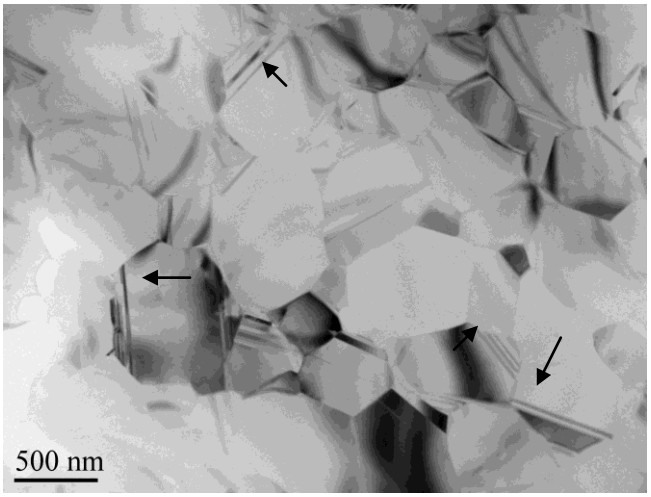

Fig. 4.3. Bright-field TEM micrograph of SPS sintered sample at 1700 ˚C for 3 min. Black arrows show twining.

4-1-2- Room temperature mechanical tests

Micrographs of fracture surfaces of boron carbide sample sintered at 1800 ˚C and one sintered at 1700 ˚C are shown in Fig. 4.4, respectively. The fracture surface of these completely dense samples shows predominantly mixed brittle fracture modes: transcrystalline and slightly intercrystalline mechanisms (Fig. 4.5a), but mostly transcrystalline (transgranular) mechanisms in sample with larger grain sizes (Fig. 4.5b). Twinning in course grains is visible even through fracture surface as shown by arrow in Fig. 4.5b.

The hardness and fracture toughness of the ceramics consolidated by SPS are summarized in Table 4.3. The measured Vickers hardness values are found to lie in the range of 22.8–36.4 GPa for the samples sintered by SPS at 1600–1800 ˚C for 0–10 min. The hardness measured in present study is higher than those obtained by other authors[13-16, 31]. As seen, there is an obvious correlation between the hardness and porosity. The highest average hardness of 36.4 GPa was found in the sample sintered at 1700 ˚C for 3 min with no porosity.

The hardness mechanism is to be controlled by dislocation motion, because dislocation activity is reported to occur in this material under mechanical solicitation [18]. The

presence of dislocation activity in this material is also proved in this study by creep test (See 4-1-3).

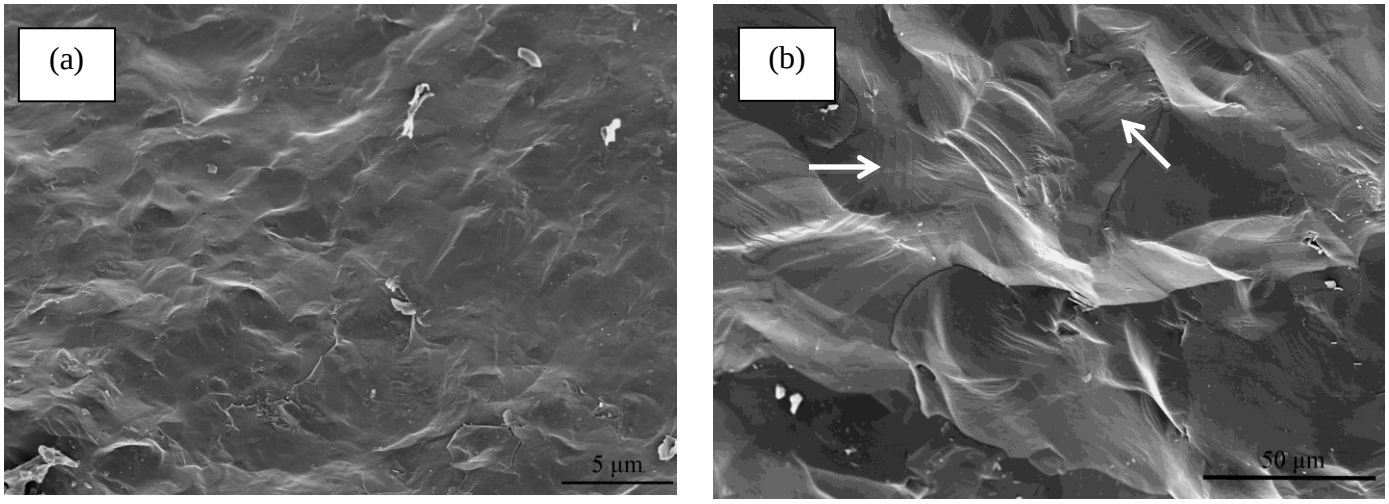

Fig. 4.4. SEM micrographs of fracture surfaces of sintered boron carbide at: (a) 1700 ˚C for 3 min and (b) 1800 ˚C for 3 min. White arrows show twinnig.

The minimum average hardness of 22.8 GPa was achieved in the sample sintered at 1600 ˚C for 5 min mainly due to the low relative density (90.3%). When comparing the results, hardness is less influenced by the grain size rather than the porosity level. Thus, the samples with the density lower than theoretical density do not follow the well-known Hall–Petch relationship and the lower hardness resulted from porous regions providing no resistance to applied load.

Table .4.3. Comparision of mean grain size, hardness and fracture toughness values for boron carbide samples.

Sample No.	Relative density (%)	Mean grain size	Max. grain size	Hardness (GPa)	Toughness ($MPa.m^{0.5}$)
1: (1800°C -3min)	100	51 µm	130 µm	28.5	1.88
2: (1750°C -3min)	100	877 nm	2.7 µm	34.2	3.05
3: (1700°C -5min)	100	811 nm	2.5 µm	35.6	3.31
4: (1700°C -3min)	100	688 nm	2.1 µm	36.4	3.65
5: (1700°C -0min)	98.2	≈ ≤688nm	-	32.3	3.75
6: (1650°C - 10min)	97.6	≈ ≤688nm	-	31.8	3.89
7: (1650°C -5min)	96.8	≈ ≤688nm	-	29.4	4.21
8: (1600°C -5min)	90.3	≈ ≤688nm	-	22.8	4.81

The indentation toughness data revealed that the average fracture toughness of the samples consolidated by SPS at 1600–1800 ˚C for 0–10 min ranged between 1.88 and 4.81 $MPa.m^{1/2}$. When compared to other previously reported studies[13-16, 31], the fracture toughness improves only slowly. For completely dense samples, the sample with smallest grain size has a higher toughness, because smaller grain size results in a larger deflection in the crack path. The maximum average toughness of 4.81 $MPa.m^{1/2}$ was

achieved in the sample sintered at 1600 ˚C for 5 min mainly due the low relative density (90.3%). It seems that the pores could behave as crack arrestors, contributing to increased fracture toughness.

Fig. 4.5 shows Raman spectra obtained from the undamaged surface as well as from the damaged regions of indentations for samples sintered at 1600 for 5 min, 1650 for 5 min and 1700 for 3 min. Raman spectrum from the undamaged polished surface in the neighbour of the indentation print is consistent with that reported in the literature for single crystal and polycrystalline boron carbide ceramics[5, 8, 13]. The several peaks in the spectrum can be related to the crystal structure of boron carbide [5, 8] as follows: The two broad peaks in the lower frequency range (at 275 and 325 cm^{-1}) are related to the chain-icosahedra linkages. The presence of the next two narrow peaks (at 478 and 532 cm^{-1}) has been related to the rotation of the CBC chain about an axis perpendicular to the [111] direction and the vibrational mode of the $B_{11}C$ icosahedron, respectively. Broad peaks in the high-frequency range (between 600 cm^{-1} and 1200 cm^{-1}) are associated to the $B_{11}C$ icosahedrons.

Raman spectra obtained from the indentation-induced damaged zones showed different features from those of the undamaged surface (compare Fig. 4.5a with b–d). The intensities of all the peaks decreased compared with that of the undamaged surface. But the most significant change was in the high-frequency range where a broad peak around 1340 cm^{-1} was observed. This peak is identified as the so-called D peak (disordered graphite peak) typically linked to amorphous carbon[13]. It has been found that the boron carbide exhibits a localized small fraction of amorphization under high velocity impact during indentation [96, 97]. Such fraction is usually considered so small that it does not restrict validity to the calculations of toughening.

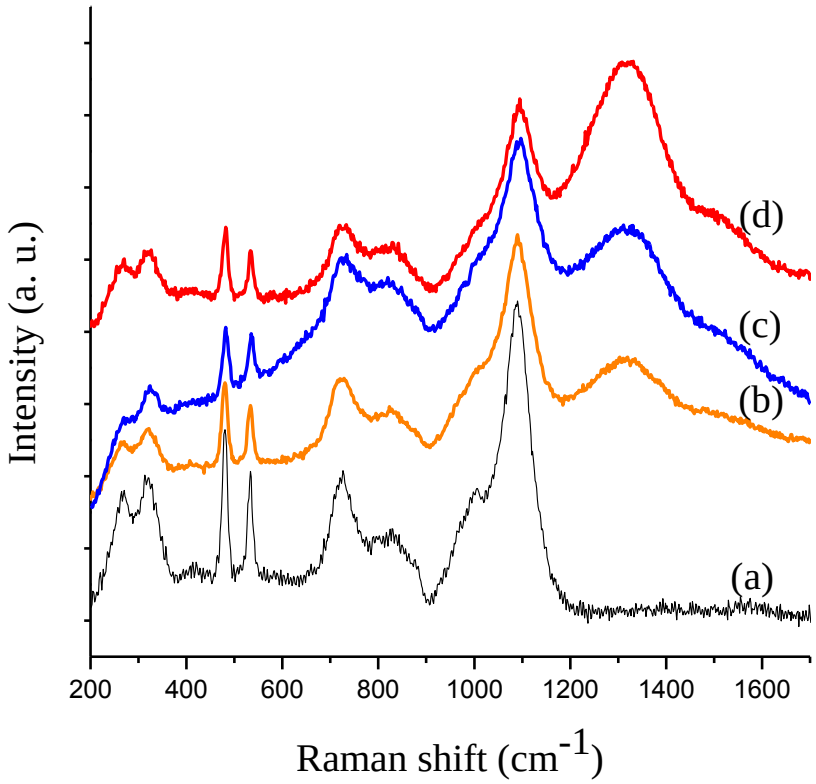

Fig. 4.5. Raman spectra from: (a) undamaged surface and indentaion regions of sintered samples at (b) 1600 ˚C for 5 min, (c) 1650 ˚C for 5 min and (d) 1700 ˚C for 5 min.

4-1-3- High-temperature mechanical test

The fully dense specimen sintered by SPS at 1700 ˚C for 3 min was chosen for further study of mechanical properties at high temperature. As it is shown before the average grain size is estimated at 0.69μm.

Figures 4.6 a and b show results from constant-load creep tests on two different B_4C samples under various temperature and stress testing conditions (as indicated). The creep tests were terminated at total homogenous deformation of ~30% and ~36% in Figs. 4.6a and b, respectively, with the samples intact. Transient creep is not observed with the change of testing conditions in Figs. 4.6 a and b, and the creep rate is found to reach a steady state immediately. In other experiment, B_4C sample was deformed by as much as ~60% without failure (Fig. 4.7 (a)); these are remarkably high creep strains for a covalently-bonded brittle ceramic and in all the cases B_4C sample was deformed homogenously as it is shown in Fig. 4.7.(b).

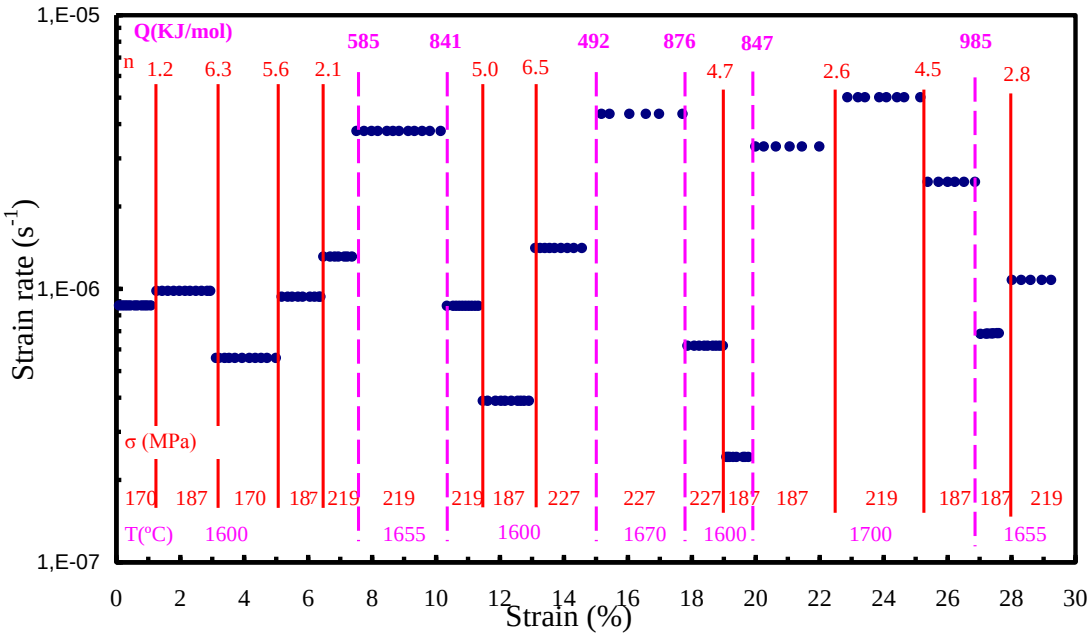

(a)

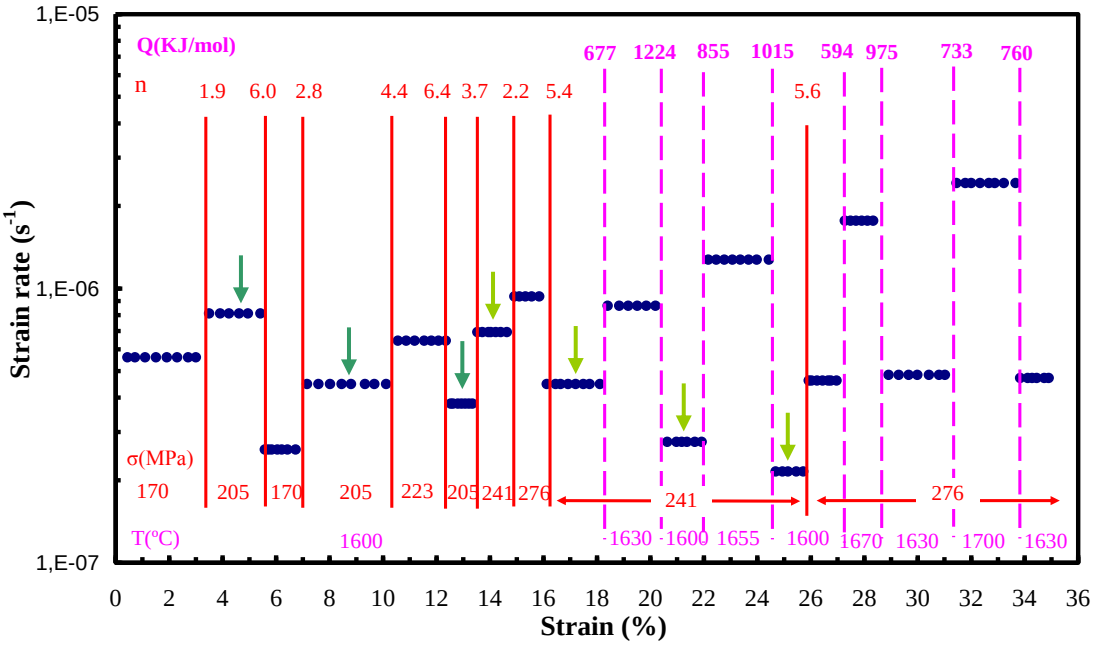

(b)

Fig. 4.6. Creep strain rate ($\dot{\varepsilon}_{ss}$) as a function of total % strain (ε) for two B_4C ceramic samples (a) and (b). The stress (σ) and temperature (T) conditions are indicated. Changes in σ and T indicated by red and pink vertical lines, respectively. Hardening effect was shown by arrows.

The estimated values of n and Q using data on either side of σ change (vertical red solid line) and T change (vertical pink dash line), respectively, are included in Figs. 4.6 a and b, and are observed to vary widely: n = 1.2 to 6.5 and Q = 492 to 1224 $kJ.mol^{-1}$. An unprecedented finding in this creep study is that the $\dot{\varepsilon}_{ss}$ for a given σ-*T* test condition,

following a higher $\dot{\varepsilon}_{ss}$ excursion, is always lower ("hardening") than the original $\dot{\varepsilon}_{ss}$ even when the original σ-T test condition is restored. A progressive hardening effect is observed. This effect should be enhanced at larger values of strain. Such tendency is displayed in Fig. 4.6 (a). Deformation stages at the same applied stress and temperatures are indicated by arrows which confirm strain hardening.

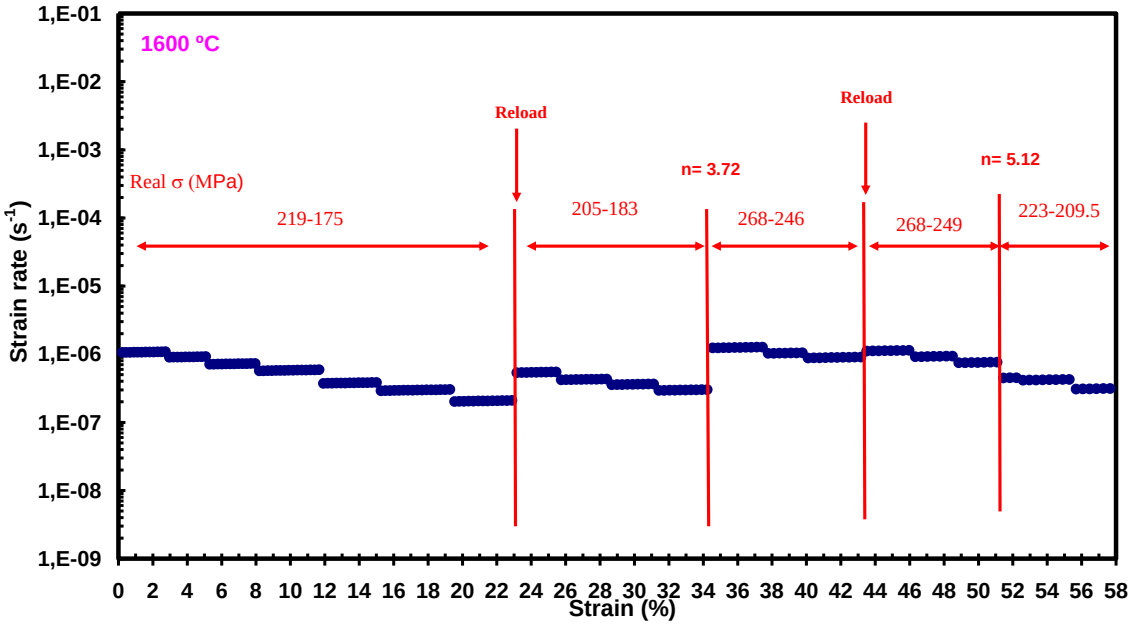

(a)

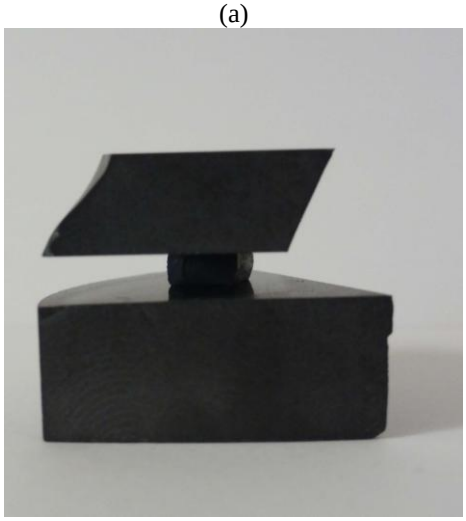

(b)

Fig. 4.7. Extreme deformation of B_4C around ~60% without failure

Figure 4.8 is a SEM micrograph of deformed B_4C (~30% total strain), evidence of cavity formation is ignorable; although grain pullout during polishing is obvious. The measured average grain size by SEM image is estimated at 0.76 μm. A comparison of Figs 4.8 and 4.2(e) confirms that the microstructural scale of the B_4C ceramic has not

changed after creep deformation. Figures 4.9 are bright-field TEM images of deformed B_4C (~30% and ~60% total strain) which show evidence of twinning, a feature which is omnipresent in this material. However, there is evidence for dislocation debris in some grains, which is not seen in the as-processed material (Fig. 4.3).The presence of trapped dislocations in twins has been observed by TEM in most grains (Fig. 4.9 (a-b,d-f)) as well as the presence of a complicated network of dislocation segments most probably sessile ones (See. Fig. 4.9 (c)).

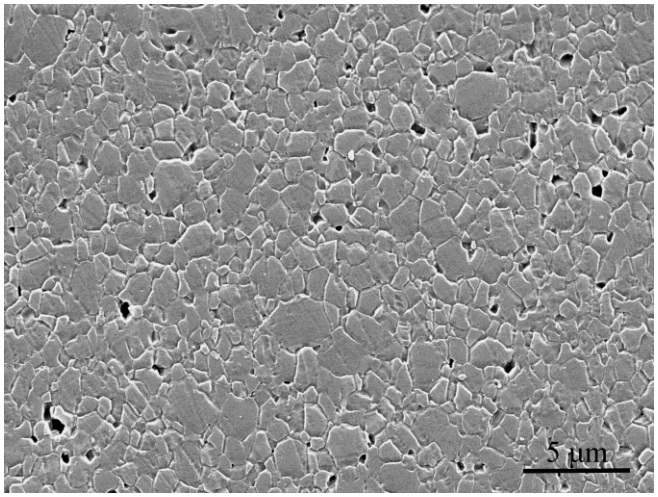

Fig. 4.8. SEM micrograph of 30% crept B_4C sample.

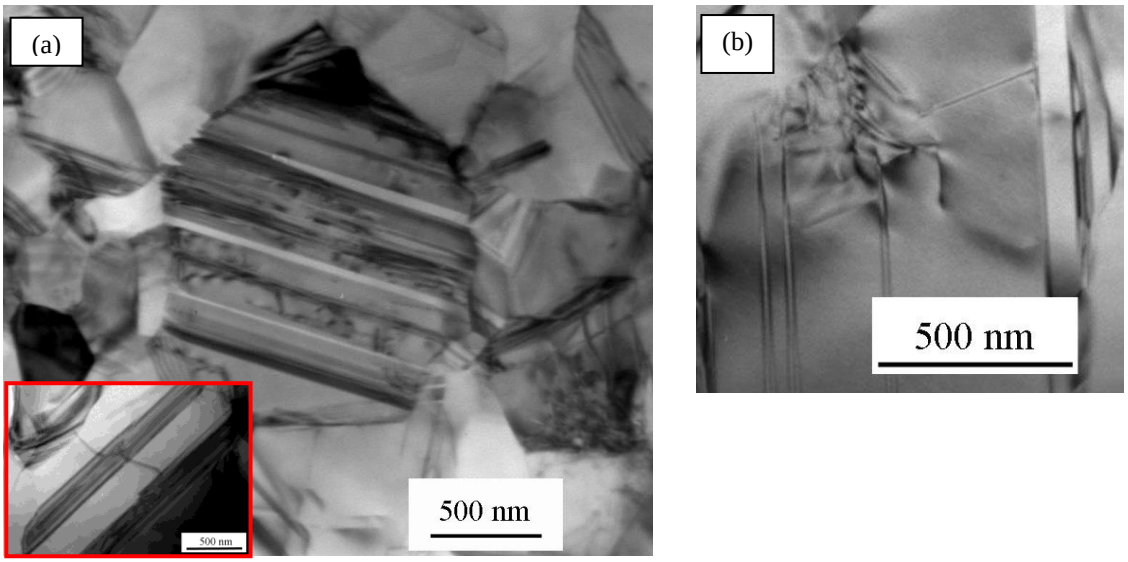

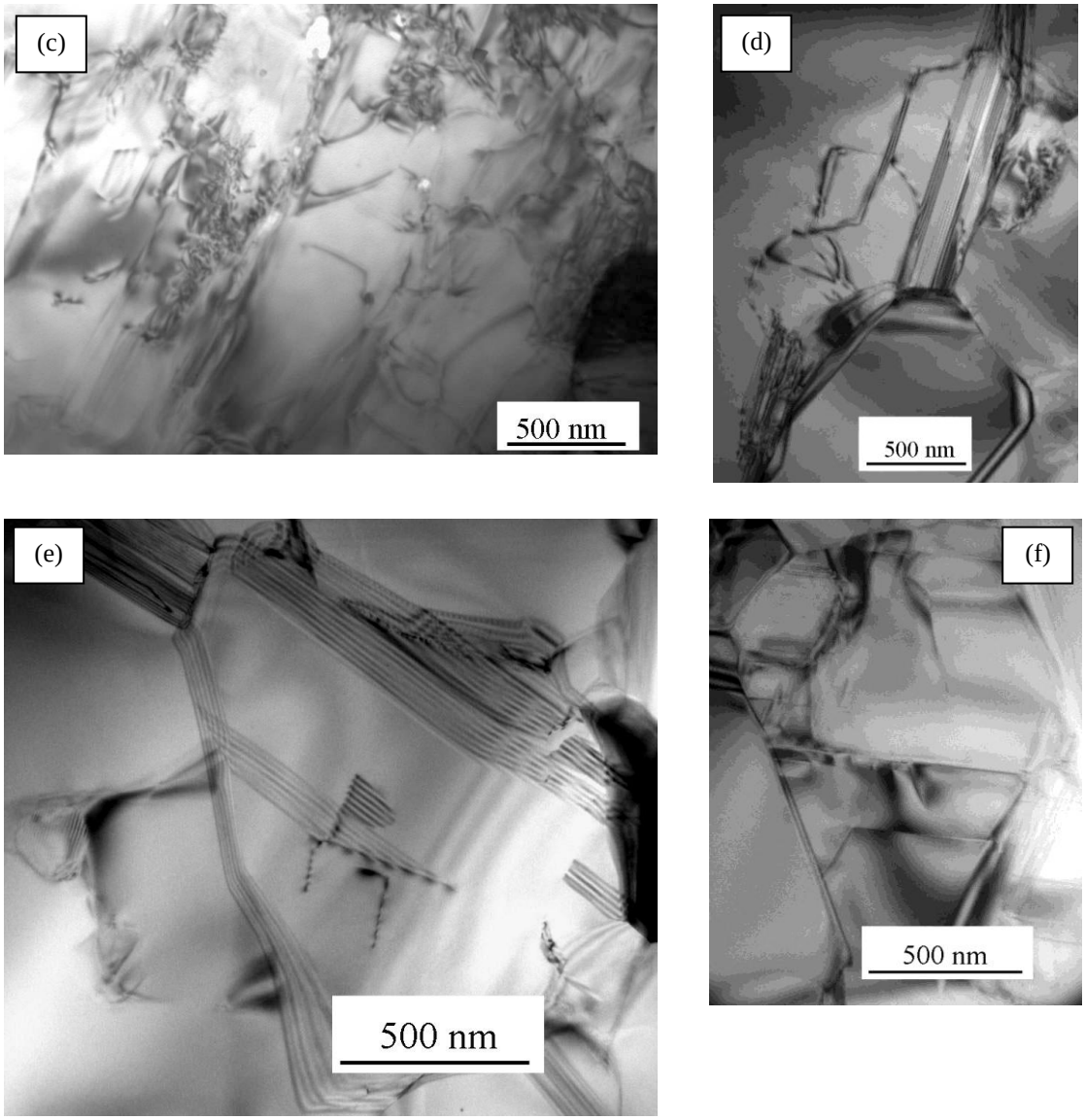

Fig. 4.9. bright-field TEM micrographs of creep-deformed B_4C ceramic: (a-d) ~60% total strain and (e-f) ~30% total strain

Fig. 4.10 is a dark-field TEM image of dislocations recorded under weak-beam condition showing a substructure of complex nodes and curved lines, a feature commonly associated both with junction formation caused by the interaction of dislocations from multiple slip planes and with the presence of small amount of solute impurities [98]. Such a substructure is associated with high-temperature recovery creep in normal ceramics [99]. The Burgers vector (*b*) of the dislocations is identified using the $g \cdot b=0$ invisibility criterion, and it is found to be $b=\langle 110 \rangle$ gliding on {111} planes. Specifically, dislocations (Fig. 4.10) 1, 4 and 5 have $b=$ [110], and 2, 3 and 6 have $b=$ [101]. Most grains show the presence of dislocation debris, with estimated dislocation density within those grains of~4×10^{12} m^{-2} for B4C sample after 36% strain. A stacking fault bound by dislocation partials is also shown in Fig. 4.10. A stacking fault energy of 81 $mJ.m^{-2}$ is estimated from the width of that stacking fault, which compares favorably

with the literature value of 76 mJ.m^{-2} [100].

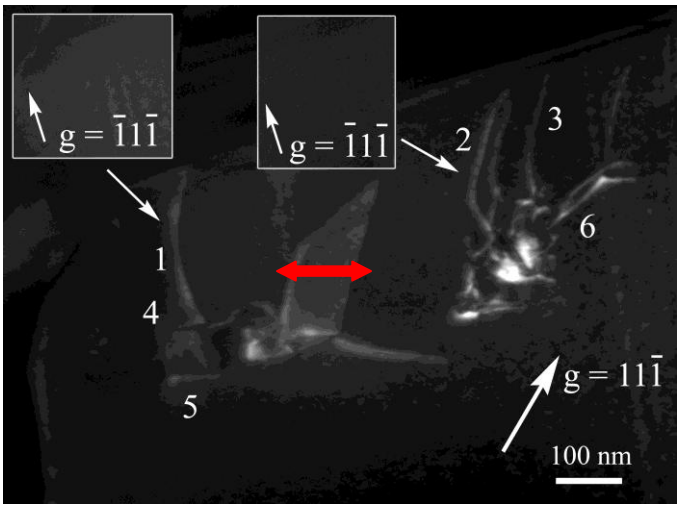

Fig. 4.10. Dark-field TEM micrograph of creep-deformed B_4C ceramic (total strain ~30%) showing dislocations 1, 4 and 5 having b=[110], and dislocations 2, 3 and 6 having b=[101]. (The red arrow indicates stacking fault.)

4-2- High-energy ball milled boron carbide powder (H. C. Starck)

The as-received sub-micrometric boron carbide powders have been subjected to high-energy ball milling to study the influence of reduced grain size of initial powders on siniterability and mechanical properties.

4-2-1- Processing by SPS and characterization

Rietveld refinements corresponding to the B_4C powder after milling is provided in Fig. 4.11. The phase fraction and crystallographic results after iterative fitting for these two samples are displayed in Table 4.4. Rietveld refinement corresponding to the powders after milling fitted on the basis of an anisotropic broadening modeling. This assumption points out micro-deformation in powders during high energy ball milling. The results show that there is 2.59 ±0.05 wt% tungsten carbide after milling that is the consequence of contamination during milling. Some weak XRD peaks could not be indexed.

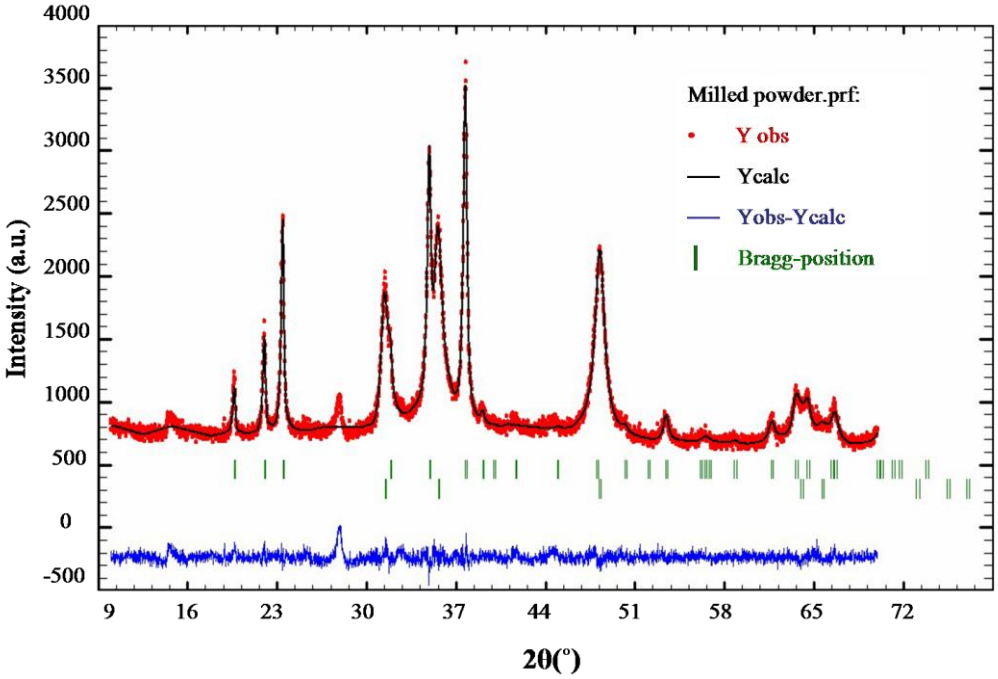

Fig.4.11. Rietveld refined XRD data for milled boron carbide powder. The selected phases according Bragg-position are with following order: B_4C (pdf card 00-035-0798) and WC (pdf card 00-051-0939). Some weak XRD peaks could not be indexed.

Table 4.4. Rietveld refinement of boron carbide powder after milling, annealing and sintering at 1700 ˚C-100 ˚C/min-3 min.

Information			Powder after milling	Powder after milling and annealing	Sintered sample at 1700 ˚C for 3 min
Phase fraction (%wt)	B_4C (R-3m)		97.41(8)	97.28(9)	97.04(12)
	WC (P-6M2)		2.59(5)	0.30 (2)	-
	B_5W_2 ($P6_3/mmc$)		-	0.79(3)	-
	B_2W ($P6_3/mmc$)		-	2.20(2)	2.96(7)
	C ()		-	0.45(7)	
Lattice parameters (Å)	B_4C (R-3m)	a	5.611(1)	5.609(1)	5.600(1)
		c	12.097(2)	12.107(2)	12.092(1)
	WC (P-6m2)	a	2.908(1)	2.948(1)	-
		c	2.844(1)	2.809(1)	-
	B_5W_2 ($P6_3/mmc$)	a	-	3.010(1)	-
		c	-	13.894(2)	-
	B_2W ($P6_3/mmc$)	a	-	2.986(1)	2.987(1)
		c	-	13.887(2)	13.889(1)
Density (g/cm^{-3})	B_4C (R-3m)		2.581	2.578	2.590
	WC (P-6M2)		15.652	15.385	-
	B_5W_2 ($P6_3/mmc$)		-	12.851	-
	B_2W ($P6_3/mmc$)		-	12.729	12.713
Chi2			1.60	2.66	2.14

Preliminary SPS experiments revealed that the ball-milled B_4C powder has poor sinterability despite the high-energy ball-milling having refined the crystal sizes notably. Indeed, it was even more difficult to densify than the as-received

submicrometric powder (See. 4-1-1). An example of this poor sinterability is shown in Fig. 4.12. This was attributed to the formation of extra amorphous B_2O_3 on the surface of the B_4C nanocrystals during milling, which is known to favour coarsening over densification[85]. Since boron oxide is in amorphous phase can not be detected by XRD (Fig. 4.11). Consequently, to enhance its sinterability, the ball-milled B_4Cpowder was annealed at 1350 ˚C (heating and cooling ramps of 5 ˚C/min) for 8 h under a flowing atmosphere of ultrahigh purity Ar, which is a heat-treatment that has already proven to be effective for the elimination of the B_2O_3 impurities in other boride ceramics [87]; the basis is that B_2O_3melts at ~510 ˚C and experiences significant evaporation beyond 1000 ˚C, so that even in the absence of chemical reactions the B_2O_3 surface impurities can be removed through the phase-change reaction $B_2O_3(l) \rightarrow B_2O_3(g)$[17].

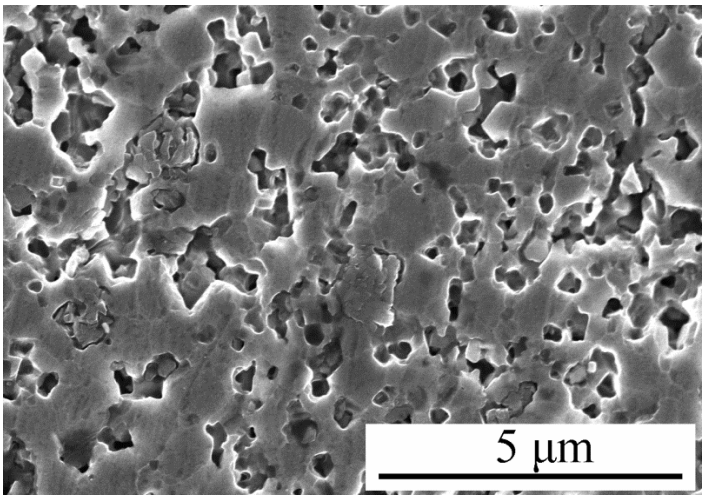

Fig. 4.12. SEM micrograph of the SPS sintered sample at 1700 ˚C for 3 min of the B_4C powder subjected to 180 min of high-energy ball-milling.

SEM image of the B_4C powders after the high-energy ball-milling and the subsequent annealing is shown in Fig. 4.13. It can be seen that the powder mostly comprises primary B_4C particles with an average size of ~220 nm and equiaxed shape. The Rietveld refinement of the corresponding XRD pattern shown in Fig. 4.14 confirmed that this powder is essentially formed by B_4C (97.3 ± 0.9 wt.%) with small amounts of WC (0.30 ± 0.02 wt.%), C (0.45 ± 0.07 wt.%), W_2B_5(0.79 ± 0.01 wt.%), and WB_2(2.20 ± 0.02 wt.%) (Table. 4.4); some weak XRD peaks could not be indexed, which most likely indicates the additional presence of trace amounts of unidentified W-rich phase(s). Unlike WC, graphite and these two latter boride phases are not direct products from the contamination by the milling media, and indeed were not detected in the B_4C powder ball-milled but not annealed, whose quantitative-phase composition was only

97.41 ± 0.08 wt.% B_4C plus 2.59 ± 0.05 wt.% WC as shown before (Table. 4.4). Consequently, the detection of C, W_2B_5, and WB_2 reflects the occurrence of reactions between B_4C and WC during the annealing treatment of the ball-milled powder at 1350◦C for8 h in Ar. This might have happened via the set of reactions:

$5B_4C + 8WC \rightarrow 4W_2B_5 + 13C$

$4W_2B_5 + C \rightarrow 8WB_2 + B_4C$

(or, $W_2B_5 \rightarrow WB_2 + B$ plus $4B + C \rightarrow B_4C$)

and perhaps also via

$B_4C + 2WC \rightarrow 2WB_2 + 3C$,

with both reaction paths leading to excess of C. This is consistent with the detection of graphite in the XRD pattern of Fig. 4.14, although it should be mentioned that part of the graphite generated could also have contributed to eliminating B_2O_3 impurities via the carbothermal-reduction reaction:

$B_2O_3 + 7C \rightarrow B_4C + 6CO(g)$

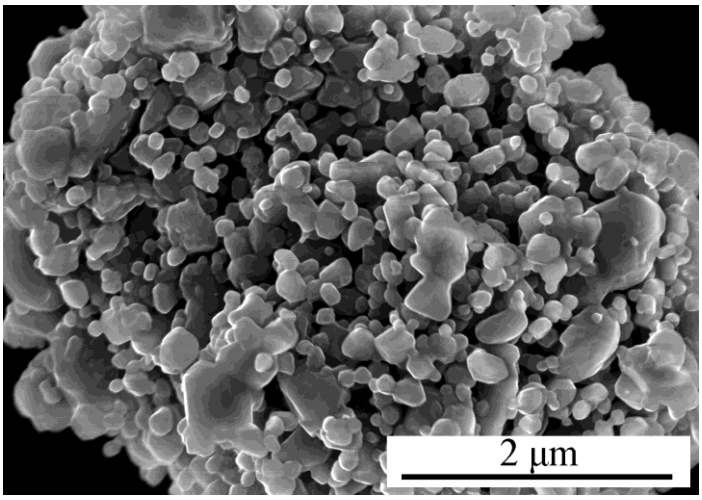

Fig. 4.13. SEM image of ultafine B4C powder obtained by high-energy ball-milling followed by annealing.

It is also interesting to note that the analysis of the peak broadening indicated that the B_4C crystallites have an average size of ~200 nm, which is very similar to the particle size measured by SEM. It is therefore reasonable to infer that the ultrafine B_4C particles obtained by the high-energy ball-milling plus annealing are essentially single crystals. Also, despite the annealing treatment, these B_4C single-crystal particles are still expected to be passivated with an amorphous B_2O_3 surface layer, which is the typically scenario in non-oxide compounds. Note that the annealing treatment alone cannot provide an oxygen-free powder because the ultrafine B_4C particles will spontaneously

passivate in contact with air. Its key function is thus only to remove the oxygen impurities introduced during the high-energy ball-milling in air. This is exactly what is observed in the comparison of XPS spectra in Fig. 4.15, which confirms the surface oxidation of the B_4C particles during milling and the elimination of oxides with the annealing down to the oxygen level in the as-received condition. The B_2O_3 removal was further corroborated by measuring the powder weight change with the annealing, which reflected a mass loss of ~13.75%. Unfortunately, it is not possible to unambiguously detect the presence of WB_2 and W_2B_5 by XPS using the B 1s core level due to their severe overlap with the signal from B_4C and to the small relative abundance of these two phases, but the XRD pattern leaves no room for doubt.

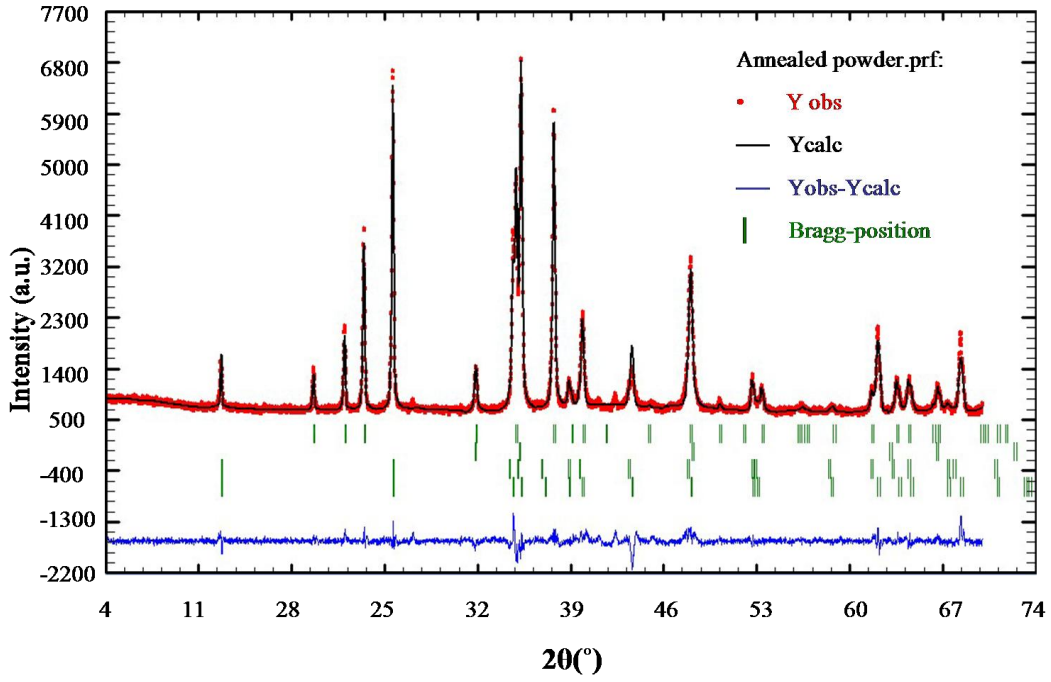

Fig. 4.14. XRD pattern of the ultra-fine B4C powder obtained by high-energy ball-milling followed by annealing. The selected phases according Bragg-position are with following order: B_4C (pdf card 00-035-0798), WC (pdf card 00-051-0939), WB_2 (pdf card 01-073-1244), W_2B_5 (pdf card 00-038-1365) and graphite (pdf card 00-056-0159).

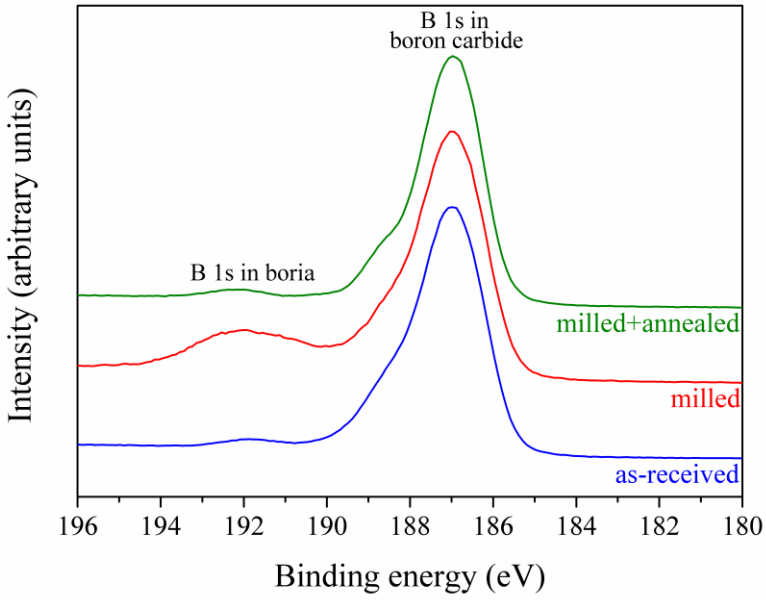

Fig. 4.15. High-resolution XPS spectra of the B 1s (singlet) core-level for the B4C powders in the as-received condition, after the high-energy ball-milling and after the high-energy ball-milling plus annealing. For the saske of comparision, the XPS spectra have been normalized by imposing the same maximum intensity for B 1s peak from B4C and then shifted along the vertical axis to facilate their observation.

Fig. 4.16 shows representative SEM images of the microstructures obtained under some of the different SPS conditions. It can be seen in Fig. 4.16(a) that the specimen obtained at 1800◦C is nominally dense (>98.5%), although unfortunately this high SPS temperature results in a coarse microstructure with an average B_4C grain size of ~17 μm. These large B_4C grains contain microtwins in their interior (originated during SPS because the B_4C particles in the powder used were single-crystals), which is not surprising because B_4C has a low stacking fault energy (See 4.1.3) and is prone to twinning[100]. On the contrary, Fig. 4.16 (b-d) shows that the SPS temperatures from 1700 ˚C downwards are increasingly effective in retaining ultrafine-grained microstructures, although the temperature of 1600◦C seems to be clearly insufficient to achieve complete densification (i.e., at least 98.5%). Indeed, it became evident during the observation of the SEM images that the SPS temperature of 1700◦C offered the best compromise in the objective of densification with retention of ultrafine grains. To confirm this mere visual appreciation and to clarify the role played by the three SPS parameters varied here (i.e., target temperature, holding time, and heating ramp), the degrees of densification and average grain sizes were measured quantitatively by the Archimedes method and SEM, respectively. The results are listed in Table 4.5.

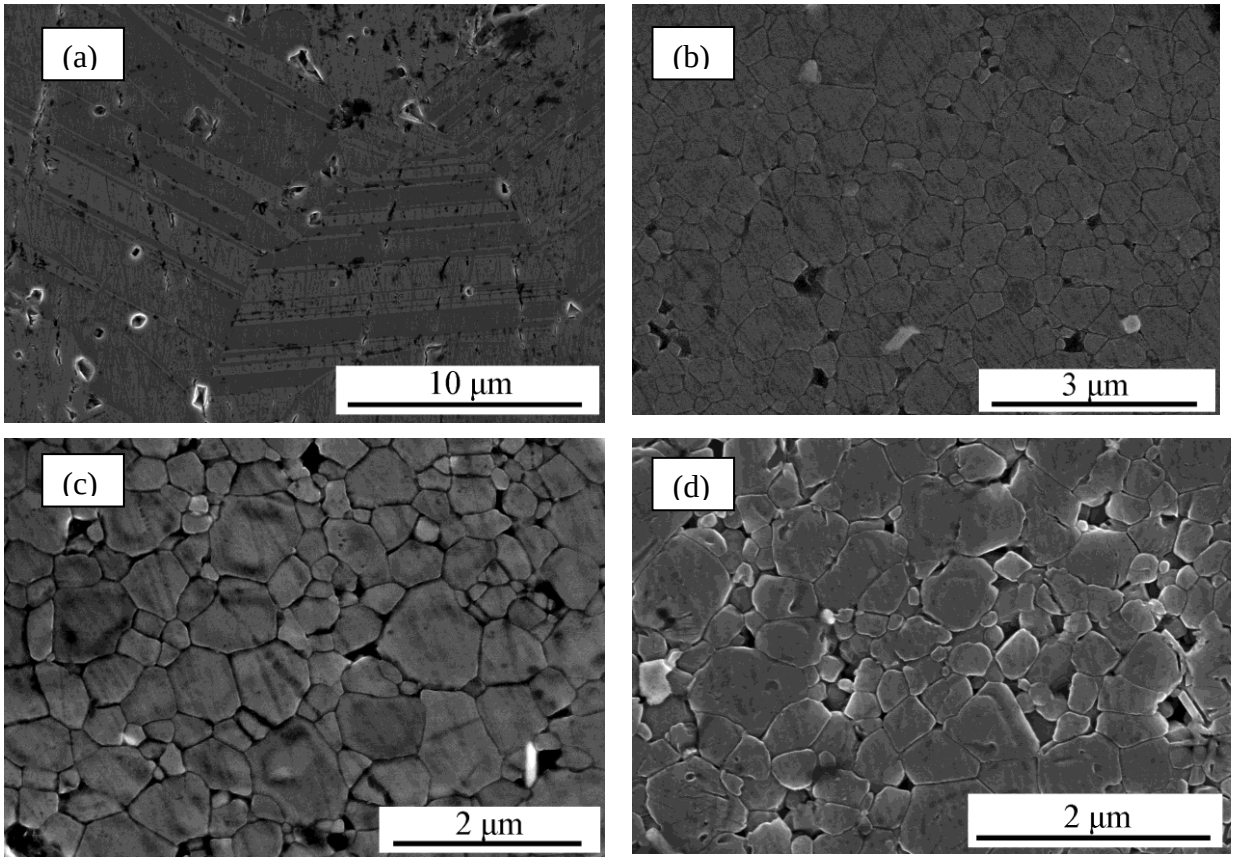

Fig. 4.16. SEM micrographs of the polished surface of the ceramics obtained from the ultrafine B4C powder with high-energy ball-milling and annealing by SPS at 75 MPa and: (a) 1800 ˚C for 3 min with heating ramp of 100 ˚C/min, (b) 1700 ˚C for 3 min with heating ramp of 200 ˚C/min, (c) 1700 ˚C for 3 min with heating ramp of 100 ˚C/min, and (d) 1600 ˚C for 3 min with heating ramp of 200 ˚C/min. The darker grains are B4C and the brighter grains are WB2. Chipping induced during sample preparation is also observed.

Table. 4.5. processing conditions, microstructural features of ultra-fine B_4C

Sample no.	Temperature (˚C)	Time (min)	Heating rate (˚C/min)	Relative density (%)	Mean grain size	Max. grain size
S1	1800	3	100	99.20	17.2 μm	33.15 μm
S2	1700	9	100	98.7	460 nm	1.35 μm
S3	1700	3	100	98.7	370 nm	1.22 μm
S4	1700	3	200	98.8	450 nm	1.42 μm
S5	1700	1	100	97.1	340 nm	935 nm
S6	1700	1	200	97.4	385 nm	1.38 μm
S7	1650	3	100	96.3	320 nm	898 nm
S8	1650	3	200	97.0	360 nm	983 nm
S9	1650	1	200	95.4	320 nm	886 nm
S10	1600	3	100	93.6	300 nm	848 nm
S11	1600	3	200	95.1	320 nm	973 nm

Firstly, the comparison of the samples labelled as (i) S3–S4, (ii) S5–S6, (iii) S7–S8, and (iv) S10–S11 (each pair of which has the same target temperature and holding time) indicates that the densification is not affected while the grain size increases with increasing heating ramp from 100 to 200 ˚C/min. This latter is somewhat surprising

considering that the higher the heating rates the shorter the time that the powder is exposed to high temperatures. It can, however, be understood by invoking the greater driving force for diffusion induced by the larger thermal gradients as the heating rate increases[101, 102], and the greater retention of boria at higher temperatures (because the pore structure collapses faster into a closed porosity)[85], both of which effects promote grain growth. This was confirmed here by monitoring the vacuum level during SPS. As it is shown in Fig. 4.17 the release of gas was more gradual (Fig. 4.17 (a)) and was shifted towards lower temperatures (Fig. 4.17 (b)) when the heating rate was set at 100◦C/min. Additionally, the effect of electric current as enhancing agent for sintering and grain growth becomes greater with increasing heating rate.

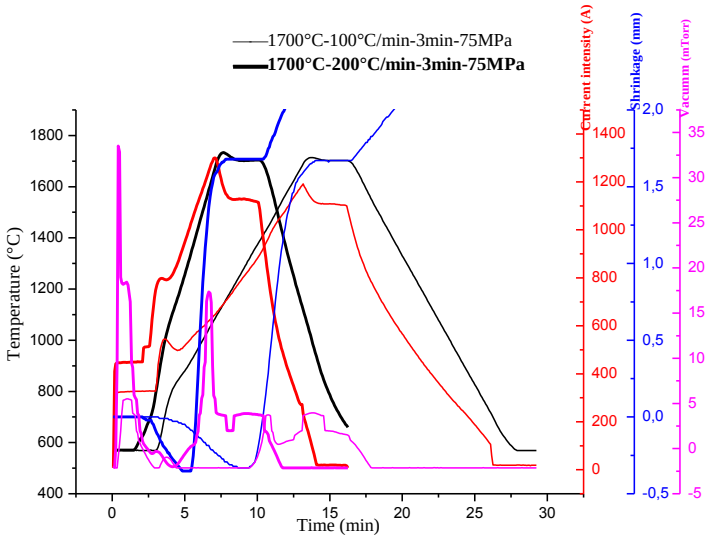

(a)

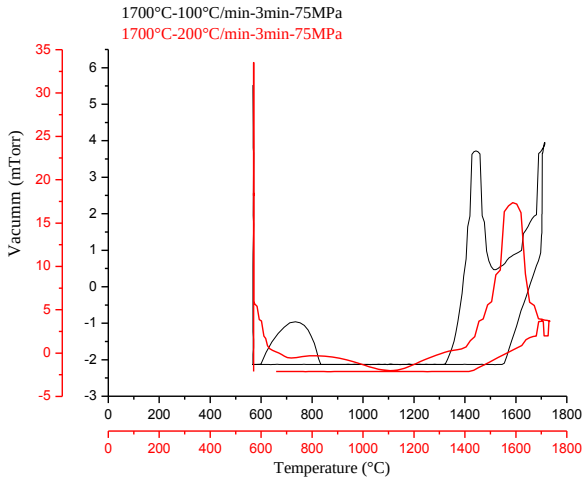

(b)

Fig. 4.17. (a) Representative densification behaviour of B_4C sample during SPS at 1700 ˚C for 3 min with two different heating rates of 100 ˚C/min and 200 ˚C/min and (b) vacuum level during SPS for these two samples.

Secondly, the comparisons (i) S2–S3–S5, (ii)S4–S6, and (iii) S8–S9 (each group of which has the same target temperature and heating ramp) indicate that the densification improves and the grain size increases with increasing holding time (Fig. 4.18(a)), which are the expected trends according to solid-state sintering theory[103]. And thirdly, the comparison (i) S1–S3–S7–S10,(ii) S4–S8–S11, and (iii) S6–S9 (each group of which has the same heating rate and holding time) indicates that the densification improves and the grain size increases with increasing target temperature(Fig. 4.18(b)), which again are the expected trends[103] because the diffusion coefficients obey an Arrhenius type law. It is also noted that the growth is normal up to 1700◦C, but exaggerated at 1800◦C. Considering normal growth regime: (i) S3–S7–S10,(ii) S4–S8–S11, and (iii) S6–S9 (each group of which has the same heating rate and holding time), the grain-growth kinetics in this regime follows the D_t^2 or D_t^3 models (i.e., $D_t^n - D_0^n = K_0 \exp(-Q/RT)t$, where D_0 is the initial grain size at holding time $t = 0$, D_t the grain size at holding time t, K_0 is a constant, Q the activation energy for grain growth, R the gas constant, and T the absolute temperature). It would be quite interesting compute accurately the activation energy for grain-boundary diffusion, and thus for grain growth, in B_4C under the current SPS conditions from the plots of $Ln\left(\frac{D_t^n - D_0^n}{t}\right)$ vs $\frac{1}{T}$. It can nevertheless be anticipated that if the D_t^2 kinetics is the appropriate one, then the activation energy for grain growth under SPS would presumably lie in the interval 200–300 kJ/mol (4.18(c)), whereas in the case of the D_t^3 kinetics, the interval would probably be 400–500 kJ/mol (4.18 (d)).

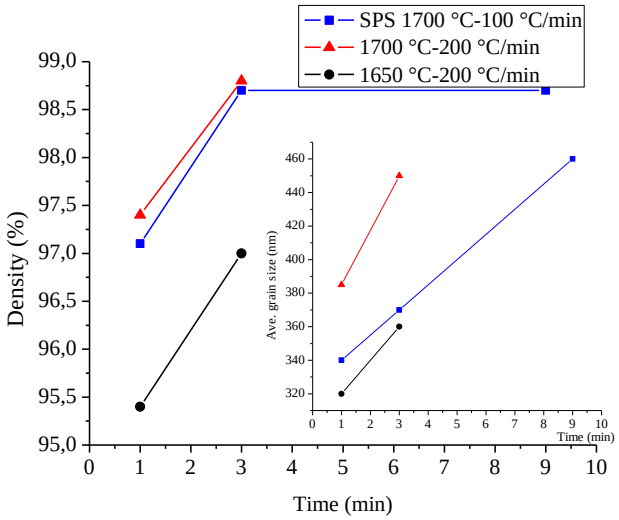

(a)

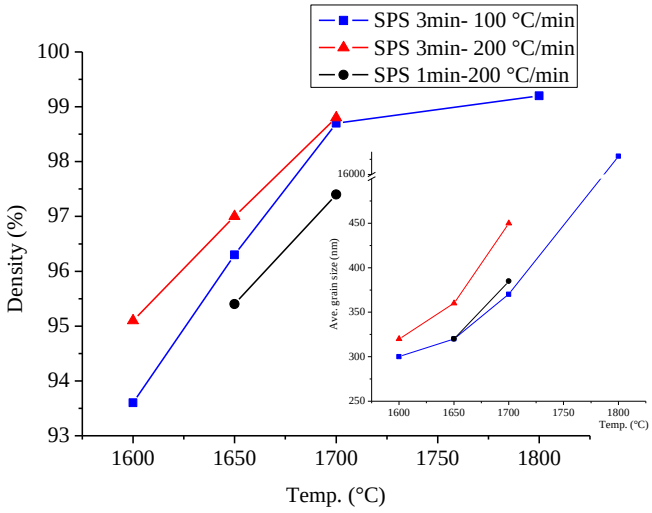
SPS 3min- 100 °C/min
SPS 3min- 200 °C/min
SPS 1min-200 °C/min
Density (%)
Temp. (°C)
Ave. grain size (nm)
Temp. (°C)

(b)

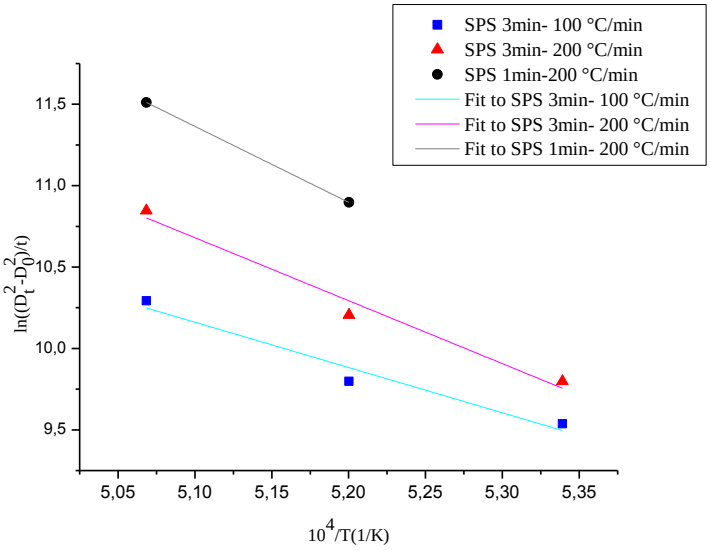
SPS 3min- 100 °C/min
SPS 3min- 200 °C/min
SPS 1min-200 °C/min
Fit to SPS 3min- 100 °C/min
Fit to SPS 3min- 200 °C/min
Fit to SPS 1min- 200 °C/min
ln((D_t^2-D_0^2)/t)
10^4/T(1/K)

(c)

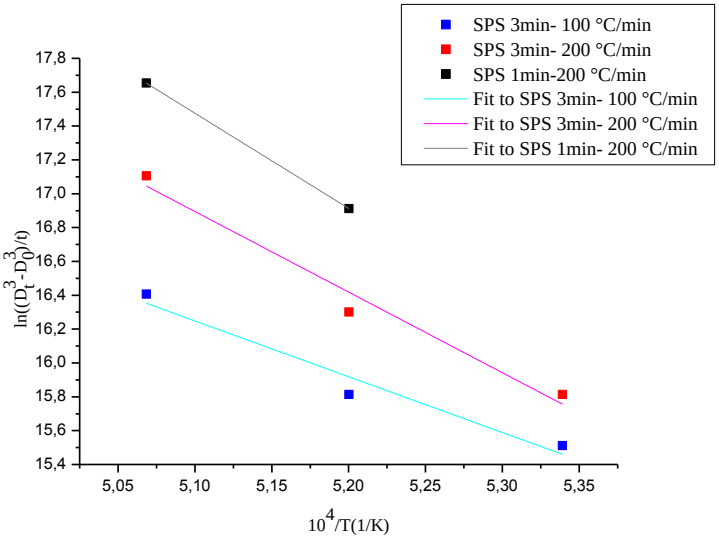
SPS 3min- 100 °C/min
SPS 3min- 200 °C/min
SPS 1min-200 °C/min
Fit to SPS 3min- 100 °C/min
Fit to SPS 3min- 200 °C/min
Fit to SPS 1min- 200 °C/min
ln((D_t^3-D_0^3)/t)
10^4/T(1/K)

(d)

Fig. 4.18. (a) Variations of density and Ave. grain size versus time for the same target temperature and heating ramp and (b) variations of density and Ave. grain size versus time for the same heating rate and holding time (c) plots of $Ln\left(\frac{D_t^2 - D_0^2}{t}\right)$ vs $\frac{10^4}{T}$ for the same heating rate and holding time and (d) plots of $Ln\left(\frac{D_t^3 - D_0^3}{t}\right)$ vs $\frac{10^4}{T}$ for the same heating rate and holding time.

The comparison of the results in Table 4.5 with the data reported earlier (See. Table. 4.3) for the ceramics prepared from the as-received powder by SPS at the same uniaxial pressure is also very interesting, and demonstrates the usefulness of the high-energy ball-milling plus annealing to improve the sinterability of B_4C. Thus for example, the as-received powder with particle sizes of 0.5 μm only reaches 90% density at 1600 ˚C for 5 min, whereas the powder prepared here reaches 94% density at the same temperature with only 3 min of SPS. At 1650 ˚C the two powders already reach the same degree of densification, but the as-received powder requires longer SPS times. Furthermore, the ball-milling plus annealing is also essential to retain ultra fine-grained microstructures.

The quantitative results in Table 4.5 also show the SPS at 1700 ˚C for 3 min with 100 ˚C/min to be the most appropriate for successful additive-free processing of ultrafine-grained, dense (i.e., >98.5%) B_4C. Consequently, this sample characterize microstructurally with more detail. Fig. 4.19 is a representative TEM image of its microstructure. It confirms that the ceramic has an equiaxed ultrafine-grain structure, with high dihedral angles at triple joints, and grain boundaries free of glassy phase, as is expected for solid-state sintered materials. The B_4C grain size is the same as that measured by SEM (i.e., ~370 nm), so that the grain growth factor is about 1.68 (lower factors were actually achieved, but at the expense of porosity). A few of the B_4C grains are seen to be twinned or nano-twinned. Indeed, the average B_4C crystallite size determined from the peak broadening during the Rietveld analysis of the XRD pattern of this sample (Fig. 4.20) is ~325 nm; once again, despite the correctness of this measurement maybe debatable numerically, it is clear that the crystallite size is beyond the nanoscale which rules out the occurrence of wholesale nano-twinning. There are also some smaller grains, which were identified as WB_2. These grains retained the small size of the WB_2 particles in the powders, or of the WC or W_2B_5 particles from which they were formed, because they are isolated in the microstructure and therefore there is hardly any W diffusion available for their growth during the rapid SPS. The extensive TEM observations with XEDS analyses never revealed the presence of any other type of grain, indicating that the WC contamination introduced during milling was eventually

all transformed to WB_2 during the SPS. This is also entirely consistent with the Rietveld analysis (See Table 4.4), which led to a quantitative phase-composition of 97.1 ± 0.1 wt.% B_4C plus 2.9 ± 0.1 wt.% WB_2 (once again with trace amounts of W-rich unidentifiedphases(s)). Finally, a few nano-pores are also observed, but the residual porosity is marginal (i.e., less than 1%).

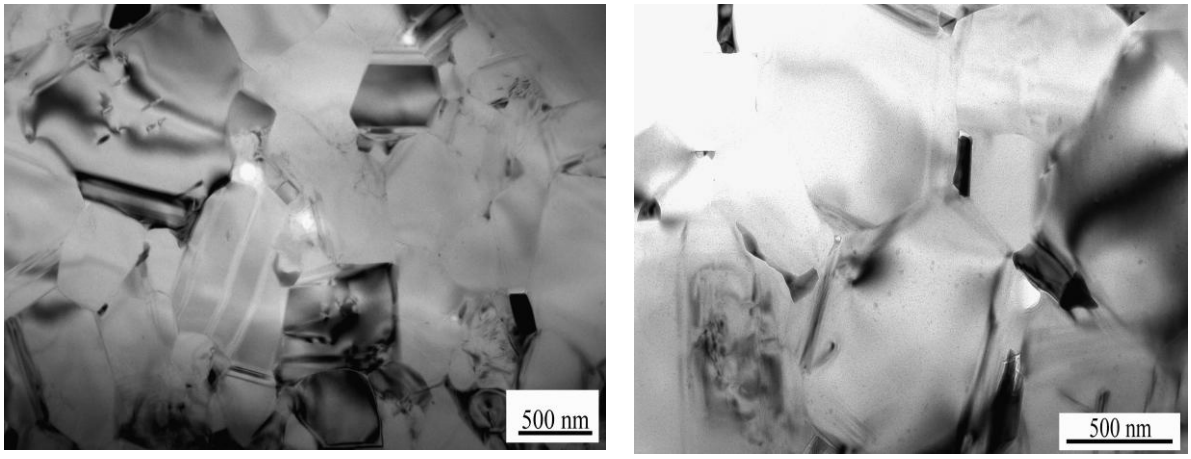

Fig. 4.19. Representative TEM micrograph of the ceramic resulting from the SPS at 1700 ˚C for 3 min with heating ramp of 100 ˚C/min of the ultra-fine B_4C powder prepared by high-energy ball-milling plus annealing.

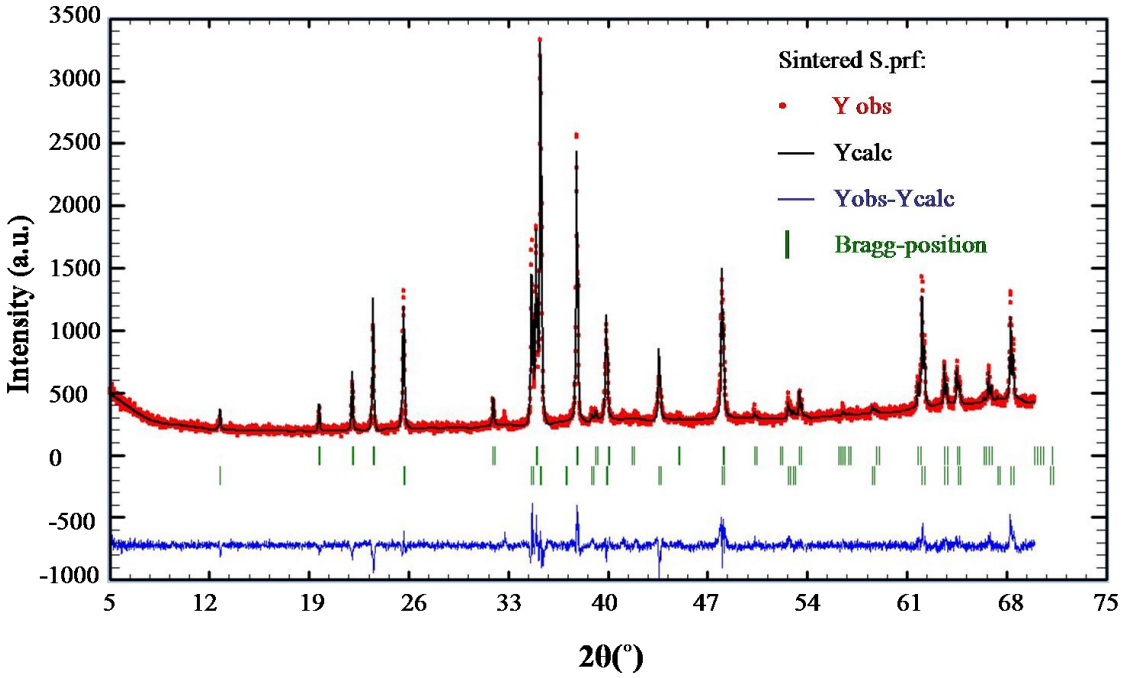

Fig. 4.20. XRD pattern of the ceramic resulting from the SPS at 1700 ˚C for 3 min with heating ramp of 100 ˚C/min of the ultra-fine B_4C powder prepared by high-energy ball-milling plus annealing. The selected phases according Bragg-position are with following order: B_4C (pdf card 00-035-0798) and WB_2 (pdf card 01-073-1244).

Fig. 4.21 shows bright-field transmission electron microscope (TEM) images of sintered B_4C at 1800 ˚C for 3min of the ultra-fine B_4C powder prepared by high-energy ball-milling plus annealing. While some twinned B_4C grains are seen in Fig 4.21 (a), a low density of dislocations is observed in some grains (Fig. 4.21 (b)). The presence of pores in grain boundaries and trapped in grains (Fig. 4.21 (a) red arrows) and pores contained of fine B_4C particles (Fig. 4.21 (a) inset) are also observed by TEM. The detailed study by TEM shows that most of the pores contain fine particles with mostly hexagonal section (Fig. 4.21(a) inset). It is notorious that these submicrometric particles have the size of initial powder. This is a piece of evidence of fast motion of grain boundaries that occurred during SPS sintering at temperatures as high as 1800 °C. It is well-known that the grain growth is a temperature-activated process that takes place during sintering. Grain boundary movements of different grains and porosity closure are closely related to each other. If the kinetics of pores shrinkage is slower than that of neighboring boundaries migration, they will be trapped inside the coarse grains. On the other hand, trapped pores will effectively limit the final densification. The presence of individual grains which contained a high density of voids and particles in B_4C specimens was reported before[104]. It is well-known that well defined crystallographic shapes of pores belong to the rhombohedral system because defects in boron carbide crystals are arranged in rhombohedral planes of the type $\{10\,\bar{1}\,1\}$[104-106].

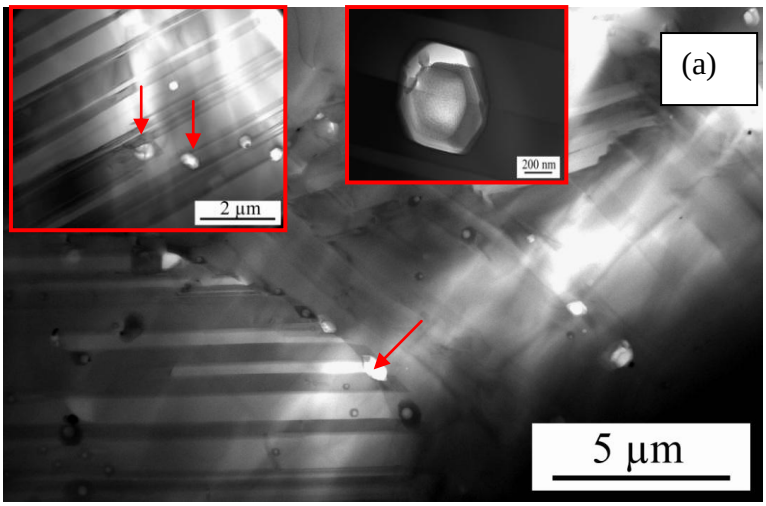

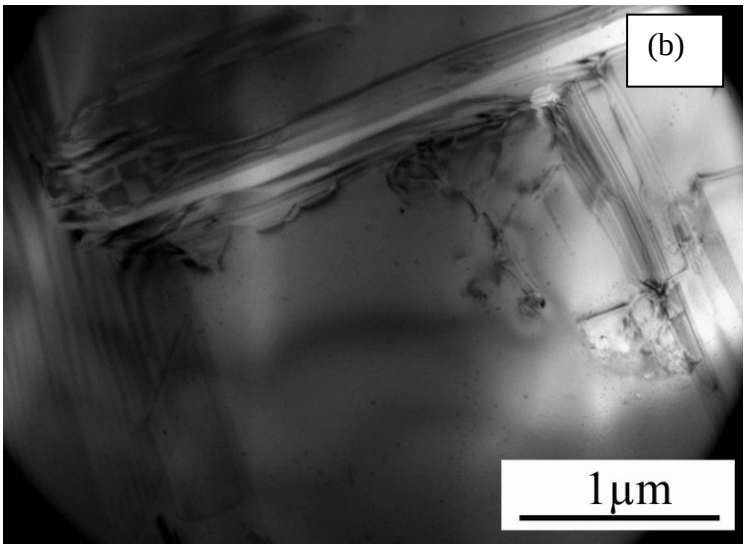

Fig. 4.21. TEM micrographs of sintered B_4C at 1800 ˚C for 3min of the ultra-fine B_4C powder prepared by high-energy ball-milling plus annealing.

4-2-2- Room temperature mechanical tests

The sintered samples with higher density and minimized average grain size were considered for further study of hardness by Vickers indentation (Table. 4.6). As is observed in Table 4.6, the sample sintered at 1700 ˚C for 3 min with heating ramp of 100 ˚C/min is the hardest of all ultrafine-grained B_4C ceramics prepared here. This is due either to its smaller grain size, its greater degree of densification, or the combination of both factors. This ultrafine-grained B_4C ceramic is thus slightly harder than its counterpart of 690 nm average grain size fabricated from the as-received powder under identical SPS conditions (i.e., 36.4 GPa (See. Table. 4.3)), which is because the hardness scales inversely with the grain size (i.e., the Hall–Petch law) [107].

Conversely the toughness, measured by the crack length technique, displays similar values to those already reported in Table 4.3. Because in both cases the fracture mode is essentially transgranular with little intergranular crack propagation, as has been seen in Fig. 4. and verified here by SEM observations of the crack propagation pattern (Fig. 4.22). SEM image showed the relatively straight propagation of the crack with barely any deflection, and the relative lack of crack bridging. Therefore it can be concluded that the average grain size of 370 nm is not small enough to change the crack propagation to intergranular mode and as a consequence the toughness is not improved in this case.

The fracture surface of the sample sintered at 1700 ˚C for 3min is shown in Fig. 4.23. The cleavage steps and features much larger than the 370 nm average grain size prove

that the fracture mode is essentially transgranular. The WB_2 grains seem to fracture intergranularly, but this is insufficient to effectively impact on the fracture behaviour. Higher toughness values were measured for the ultrafine-grained ceramics prepared at 1650 ˚C, but that is simply an artefact associated with their greater residual porosity.

Table 4.6. Mechanical properties of the additive-free B_4C ceramics prepared by SPS

Sample No.	Sintering condition: Temp. ˚C - Time(min)-Heating ramp (˚C/min)	Relative density (%)	Ave. grain size (nm	Hardness (GPa)	Fracture toughness (MPa $m^{1/2}$)
S3	1700-3-100	98.7	370	37.8	3.1
S4	1700-3-200	98.8	450	37.0	2.9
S5	1700-1-100	97.1	340	36.5	3.1
S6	1700-1-200	97.4	385	37.4	3.0
S7	1650-3-100	96.3	320	34.9	3.6
S8	1650-3-200	97.0	360	36.4	3.4

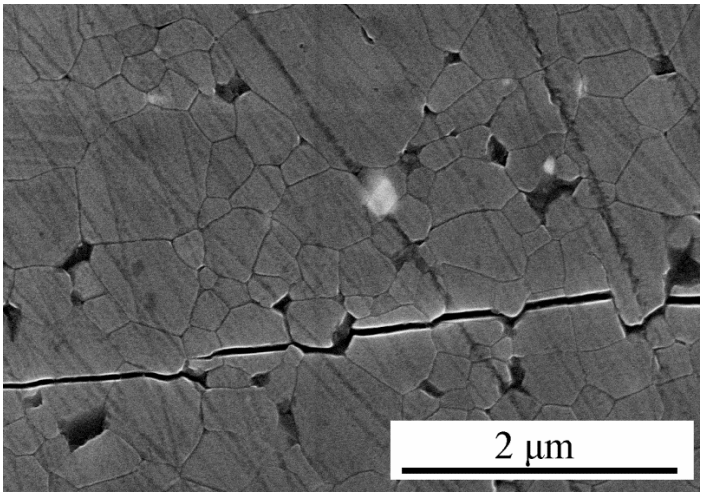

Fig. 4.22. SEM micrograph of the crack propagation resulting from the SPS at 1700 ˚C for 3min of the ultra-fine B_4C powder prepared by high-energy ball-milling plus annealing.

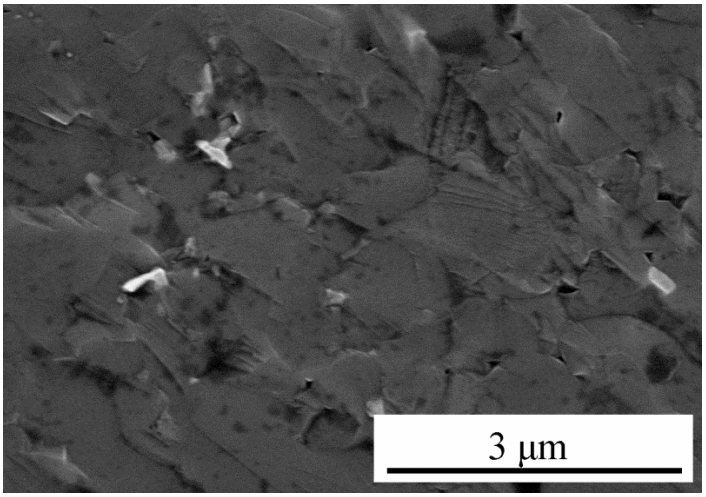

Fig. 4.23. SEM micrograph of the fracture surface of broken ceramic resulting from the SPS at 1700 ˚C for 3min of the ultra-fine B_4C powder prepared by high-energy ball-milling plus annealing. The darker grains are B4C and the brighter grains are WB_2.

4-2-3- High-temperature mechanical test

The ball-milled and annealed boron carbide powder sintered by SPS at 1800 °C for 3 minutes and also the specimen sintered at 1700 ˚C for 3 min were chosen for further study of mechanical properties at high temperature. In both cases, a pressure of 75 MPa was applied upon heating and the heating rate was 100 °C/min. As it is shown before (Table. 4.5) the average grain size is estimated around 17 micron and 370 nm, respectively.

Figures 4.24 (a) show results from constant-load creep tests on B_4C sample sintered at 1800 °C for 3 with coarse grains of 17 micron under various temperature and stress testing conditions (as indicated). For this sample, the final deformation was around 13%, and the deformation was homogeneous. No transient creep following a sudden stress or a temperature change was detected. The values of the activation energies and stress exponents are, within the experimental error, Q= 650±15 KJ/mol and the stress exponent can vary from values near 2 until values as high as 3. The average value is n=2.7±0.4. However, more definitive values of Q and n were determined using constant-stress and constant-temperature creep tests, results from which are plotted in Fig. 4.24(b) and 4.24(c), respectively. Fig. 4.24(b) is the Arrhenius plot of $\dot{\varepsilon}_{ss}$ vs. 1/T (σ = 255 MPa; T range 1600–1800˚C), revealing an activation energy Q ~ 632 kJ/mol. In this experiment, the total deformation was ~18% at the end of the creep test. Fig. 4.24(c) plots $\dot{\varepsilon}_{ss}$ vs. σ at T = 1650˚C and 1700˚C, giving n values of 3.1 ± 0.3and 3.0 ± 0.3, respectively. The Q and n values determined from Figs. 4.24(a) and (b-c) appear to be in reasonable agreement.

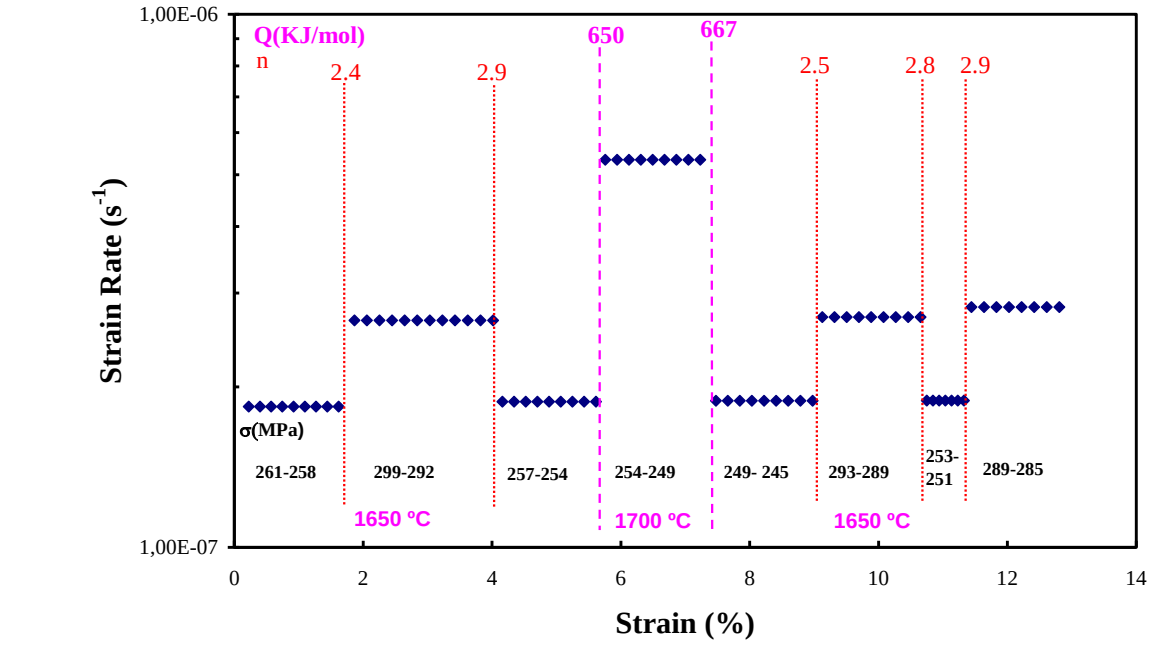

(a)

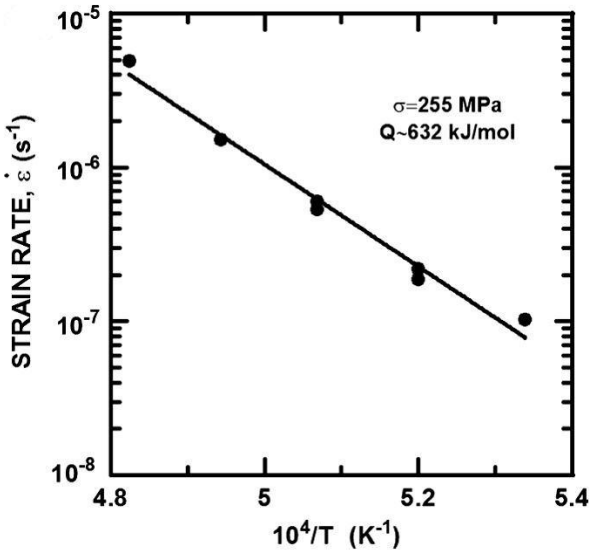

(b)

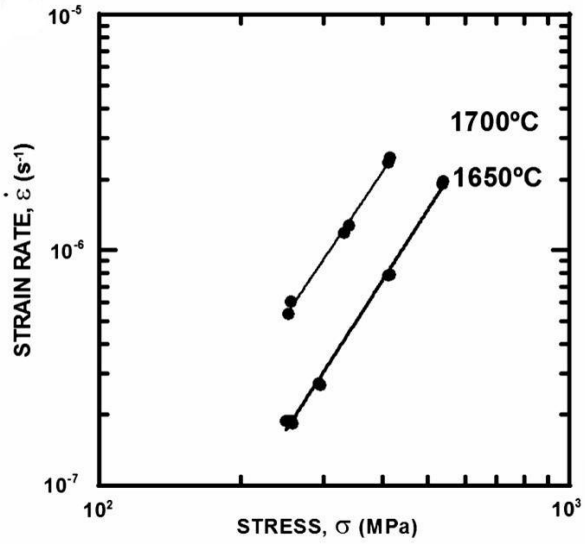

(c)

Fig. 4. 24. (a) Creep strain rate ($\dot{\varepsilon}_{ss}$) as a function of total % strain (ε) and (b) Arrhenius $\dot{\varepsilon}_{ss}$ vs. 1/T plot (σ = 255 MPa; T range 1600–1800◦C) (c) Plot of $\dot{\varepsilon}_{ss}$ vs. σ at 1650˚C and 1700˚Cfor B_4C ceramic sample from the SPS at 1800 ˚C for 3min of the ultra-fine B_4C powder prepared by high-energy ball-milling plus annealing.

SEM observation of 13% crept specimen sintered at 1800 ˚C for 3min of the ultra-fine B_4C powder prepared by high-energy ball-milling plus annealing (Fig. 4.25) shows also non-equiaxed grained microstructure with similar average grain size of around 17±3 μm. Thus, no grain growth is detected after the creep test. Close observation of scanning electron micrographs indicates the presence and predominance of twin structures (deformation twins). After creep, almost most of the grains are found to exhibit twin

structures in several directions in individual grains. Twining in B_4C is reported to occur along rhombohedral planes of the types $\{10\,\bar{1}\,1\}$[105, 106].

Figures 4.26 are bright-field and dark-field TEM images of deformed B_4C (~13% total strain). Besides twinning, a high density of dislocation density is present. Typically dislocations in boron carbide single crystals are straight lines, adjacent segments of which are alternately parallel to different rhombohedral axes, as it can be seen in Fig. 4.26 (a). Long cross-slipping dislocation segments of screw character are observed. When density increases, the dislocation debris shows a complicated substructure of complex nodes and curved lines – a feature commonly associated both with junction formation caused by the interaction of dislocations from multiple slip planes or with fine B_4C particles (blue and red arrows, respectively in Fig. 4.26 (b-d)). Also the twinned crystal planes act as sub-boundary-like obstacles to dislocation motion, leading to strengthening of the material under progressing strain (Fig. 4.26 (e)). In large regions free from twin planes, a tendency for self-organization in cells is observed (figure 4.26 (e)). Such a microstructure is classically associated with high-temperature recovery creep. It is reported that the dislocation microstructure in boron carbide consists of dislocations with **b**=<1 1 0> gliding in {1 1 1} planes[100, 104]. Complex nodes in this material are comprised of perfect and imperfect dislocations which do not all lie in the same plane and, when this involves mixture of in the (111) plane. A key microstructural observation is the presence of many pile-ups blocked by lattice obstacles, such as twins or grain boundaries (figure 4.26 (f)).

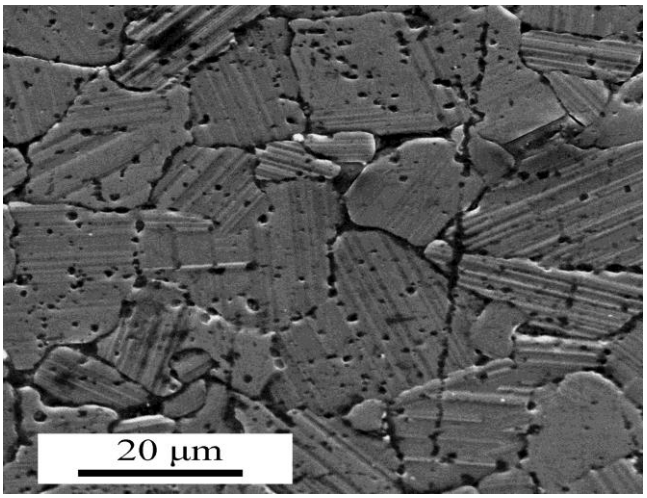

Fig. 4.25. SEM micrograph of 13% crept B_4C ceramic SPS sintered at 1800 ˚C for 3 of the ultra-fine B_4C powder prepared by high-energy ball-milling plus annealing.

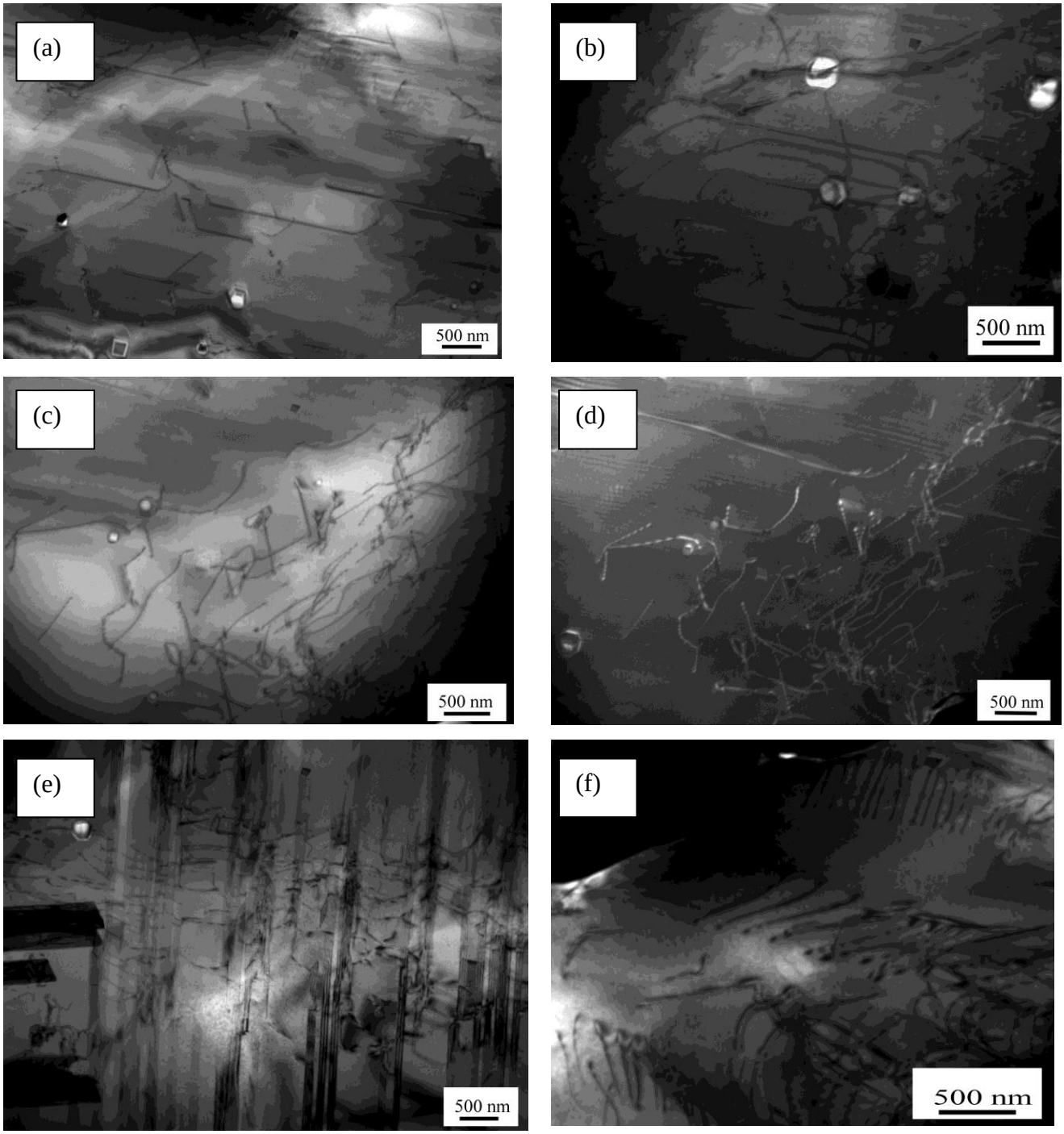

Fig. 4.26. TEM micrograph of 13% crept B_4C ceramic SPS sintered at 1800 ˚C for 3 of the ultra-fine B_4C powder prepared by high-energy ball-milling plus annealing.

The creep test was also performed for two different samples sintered at 1700 ˚C for 3 min with average grain size of 370nm. The creep tests were terminated at total homogenous deformation of ~45% and ~56% as shown in Figs. 4.27 a and b, respectively, with the samples intact. The estimated values of n and Q calculated by using data in Figs. 4.27 a and b, and are observed to vary widely and to higher values

compare with its counterpart of 690 nm average grain size fabricated from the as-received powder under identical SPS conditions (Fig. 4.6) : n = 3.5 to 9.3 and Q = 993 to 1245 kJ.mol^{-1}.

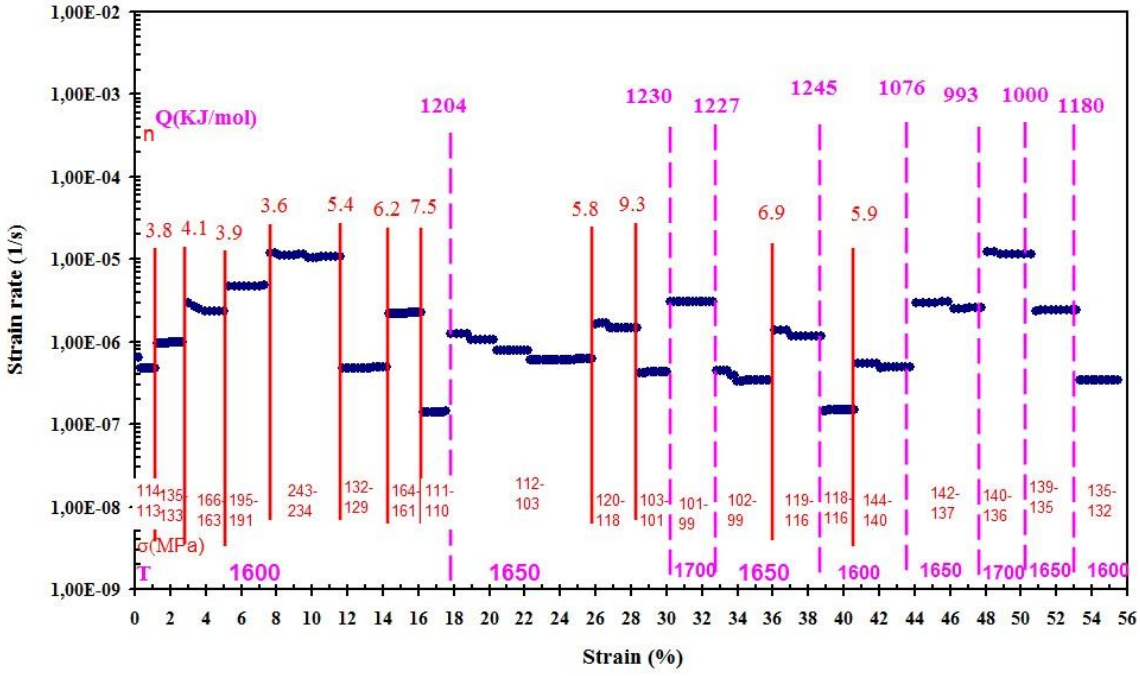

(a)

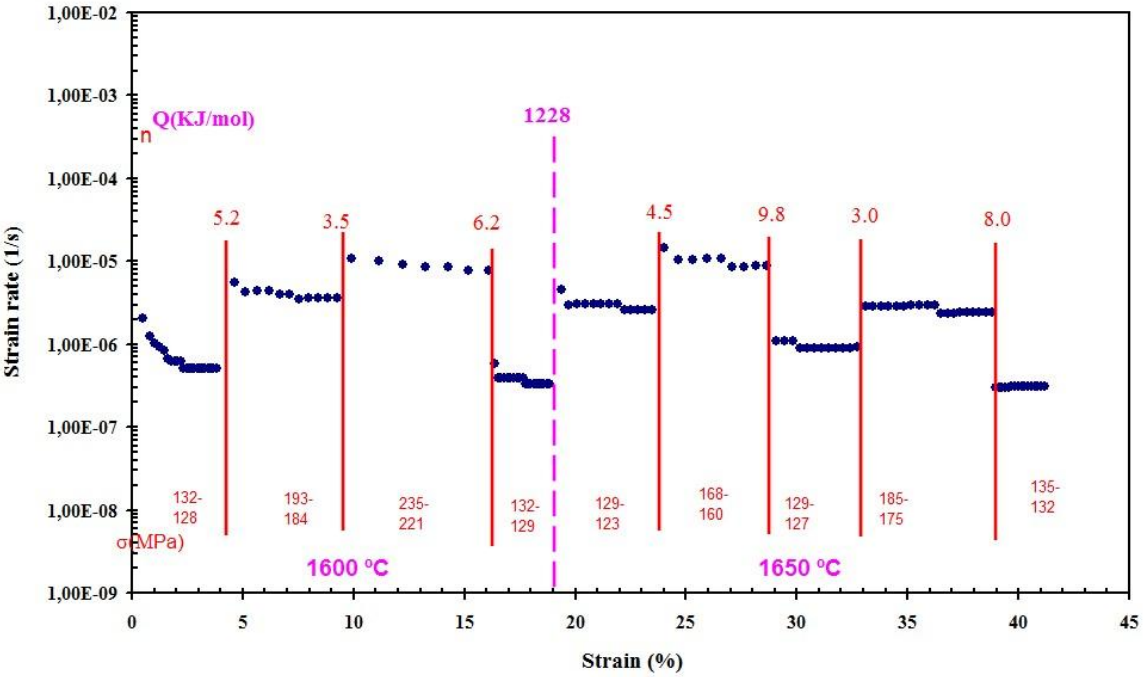

(b)

Fig. 4. 27. Creep strain rate ($\dot{\varepsilon}_{ss}$) as a function of total % strain (ε) for two B_4C ceramic samples (a) and (b) from the SPS at 1700 ˚C for 3min of the ultra-fine B_4C powder prepared by high-energy ball-milling plus annealing.

SEM micrograph of 56% crept specimen sintered at 1700 ˚C for 3min of the ultra-fine B_4C powder prepared by high-energy ball-milling plus annealing is shown in Fig. 4.28. Evidence of cavity formation is ignorable. The measured average grain size of crept sample by SEM image is estimated at 0.5 μm while grain size distribution is from 140nm to 1.30μm. A comparison of Figs 4.28 and 4.16(c) confirms that the microstructural scale of the B_4C ceramic has not changed after creep deformation. A it is mentioned before, the darker grains are B_4C and the brighter grains are WB_2.

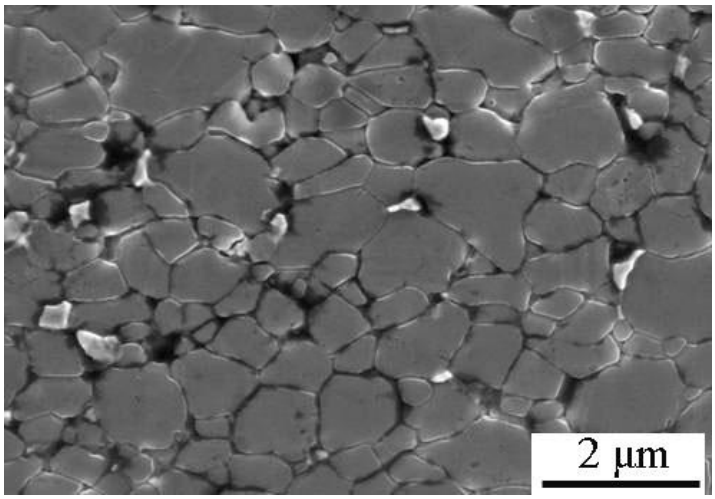

Fig. 4.28. SEM micrograph of 56% crept B_4C ceramic SPS sintered at 1700 ˚C for 3 of the ultra-fine B_4C powder prepared by high-energy ball-milling plus annealing.

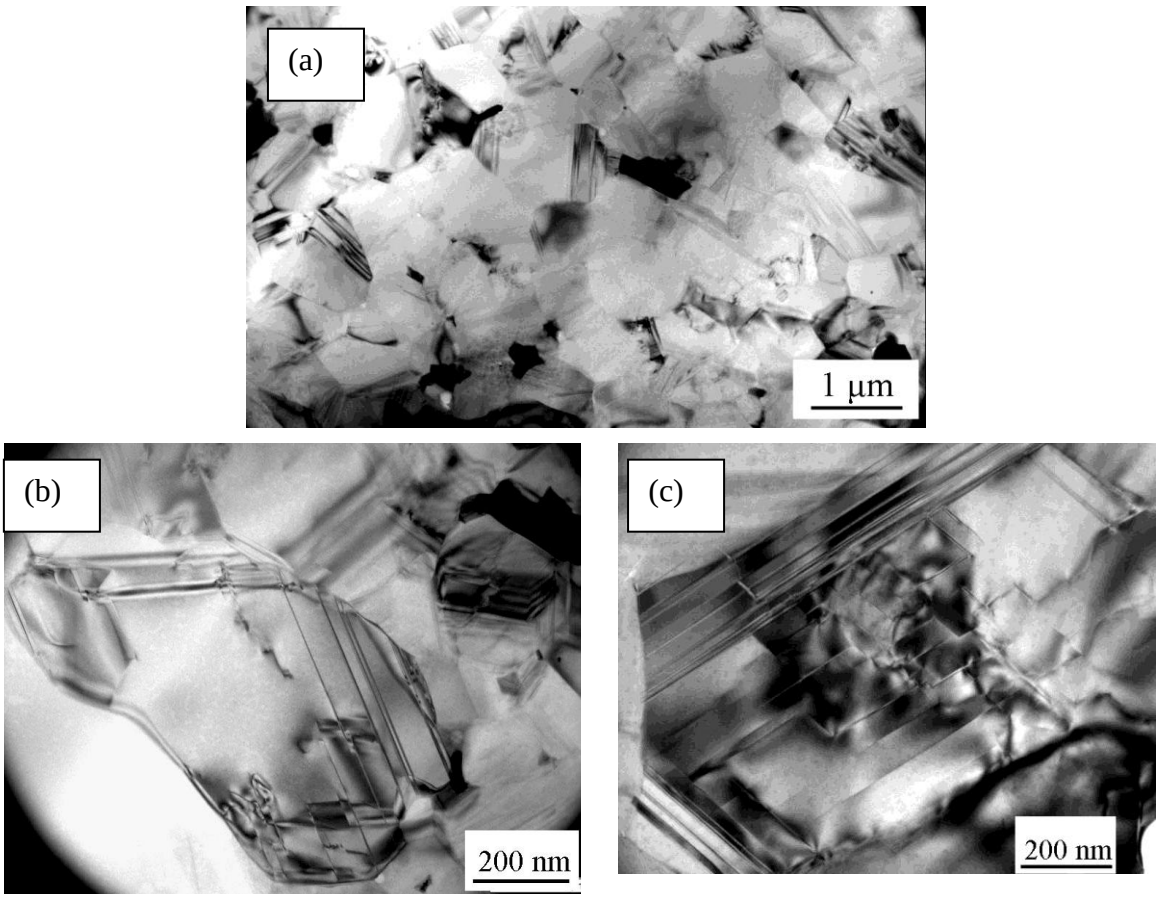

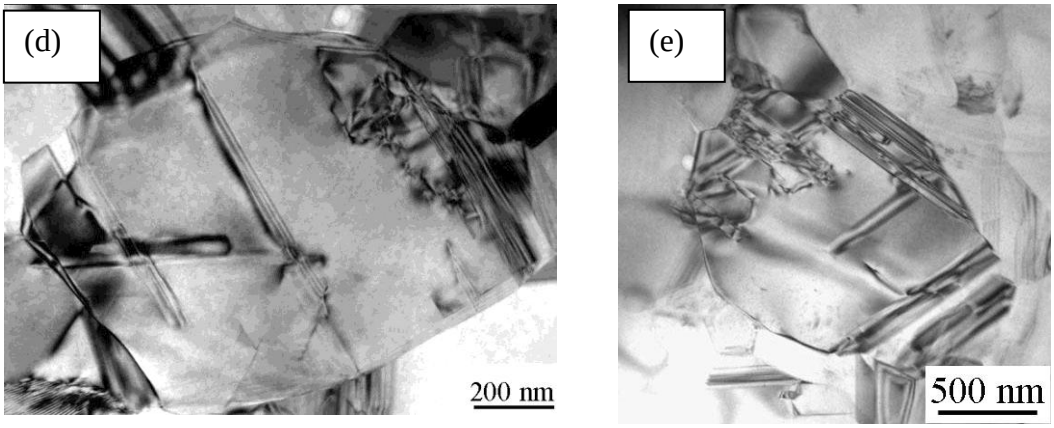

Fig. 4.29. TEM micrograph of 45% crept B_4C ceramic SPS sintered at 1700 ˚C for 3 of the ultra-fine B_4C powder prepared by high-energy ball-milling plus annealing.

Figures 4.29 are bright-field TEM images of deformed B_4C (~45% total strain) which show evidence of twinning, a feature which is omnipresent in this material. Evidence of cavity formation is ignorable (4.29 (a)). However, there is evidence for dislocation debris in some grains, which is not seen in the as-processed material (Fig. 4.19).The presence of trapped dislocations in twins has been observed by TEM in most grains (Fig. 4.29 (b-c)) as well as the presence of a complicated network of dislocation segments most probably sessile ones (See. Fig. 4.29 (d-e)).

4-3- B_4C composites with addition of SiC and SiC plus graphite

4-3-1- Processing by SPS and characterization

As it was pointed out before in order to improve mechanical properties at room temperature, two different composites were prepared; one B_4C with 15 wt.% SiC, and the other B_4C with 15 wt.% SiC and 2 wt.% graphite. The powder preparation was explained before (See. 3.1). Different samples were prepared by SPS which are listed in Table. 4.7.

Table. 4.7. Processing conditions, microstructural features.

Sam. No.	Composition (wt%)	Sintering conditions		Relative density (%)	Grain size (nm)	
		Temp. (˚C)	Time (min)		B_4C	SiC
B6 (From Table 4.1)	100%B_4C	1700	3	100	688	-
B10 (From Table 4.1)	100%B_4C	1650	5	96.8	≤688	
BS1	B_4C-15%SiC	1700	3	99.4	537	50-250
BS2	B_4C-15%SiC	1650	5	96.6	≤537	
BSG1	B_4C-15%SiC-2%G	1700	3	100	615	90-300
BSG2	B_4C-15%SiC-2%G	1650	5	98.8	≤615	

It can be seen that both composites of B4C with SiC and plus graphite similar to pure B_4C are completely dense when the SPS temperature is 1700 ˚C, while the composite

with only SiC has a quite small residual porosity (i.e., less than 0.6%). However, with decreasing SPS temperature down to 1650 ˚C the three materials become slightly porous (i.e., no more than ~3.5% porosity). Nevertheless, it can be seen in Table 4.7 that the composite of B_4C with SiC plus graphite densified better than the pure B_4C ceramic, and this latter slightly better than the composite with only SiC.

Taken altogether, the degrees of densification in Table 4.7 indicate that the high-energy co-ball milling of B_4C with SiC is detrimental for the sinterability of B_4C, but become beneficial if the same co-ball milling is performed in presence of graphite. The former is a surprise because the key role of the co-ball milling of B_4C with SiC are the refinement of the primary particle sizes to the nanoscale with formation of nano-agglomerates and the homogeneous dispersion of B_4C and SiC also at the nanoscale.

According to the theory of the solid-state sintering[103] this should have resulted in a marked improvement of the SPS kinetics. Here, on the contrary, the sinterability not only did not improve but indeed worsened slightly. The reasonable explanation for this poorer sinterability is that the larger specific surface area available for passivation resulting from the particle size refinement entails greater formation of surface oxides (B_2O_3 on the B4C particles and SiO_2 onto the SiC particles), and these oxides are detrimental for the densification because they promote the mass transport mechanisms of evaporation-condensation or surface diffusion[39, 85]. The as-received submicrometric B_4C powder is also passivated with a B_2O_3 layer, but the concentration of B_2O_3 is much lower and there is no SiO_2. In this context, the addition of graphite to the B_4C–SiC mixture may have a doubly beneficial effect for the densification. Firstly, graphite would contribute to reach a more intimate contact favouring the diffusion between the powder particles during the first moments of SPS because on one hand it is an effective process-control agent that minimizes the formation of agglomerates during the milling of brittle ceramics[108], and on the other hand it can lubricate the contacts during the compaction stage thus promoting a better particle packing. Secondly, the graphite nano-flakes dispersed between the B_4C and SiC particles, because graphite is also very brittle and is refined as well during the high-energy ball-milling would help to eliminate part of the undesirable oxides by carbothermal reduction[85].

The SEM examination of the composites supports the density results achieved from the Archimedes method. As shown in Fig. 4.30, the two composites are fully dense or near-fully dense with the SPS at 1700 ˚C; furthermore, the degree of porosity increases with decreasing SPS temperature to 1650 ˚C, a trend that is however less notorious for the composite of B_4C with SiC plus graphite. The SEM images of the composites also show

that the SiC grains are distributed uniformly in the B_4C matrix, and have ultra-fine sizes. They seem to be slight larger in the composite with graphite (i.e., 50–250 nm vs. 90–300 nm), and quite independent on the SPS temperature (1650 or 1700 ˚C). The former is consistent with the better sinterability of the composite with graphite, whereas the latter reflects the large dispersion in the grain sizes.

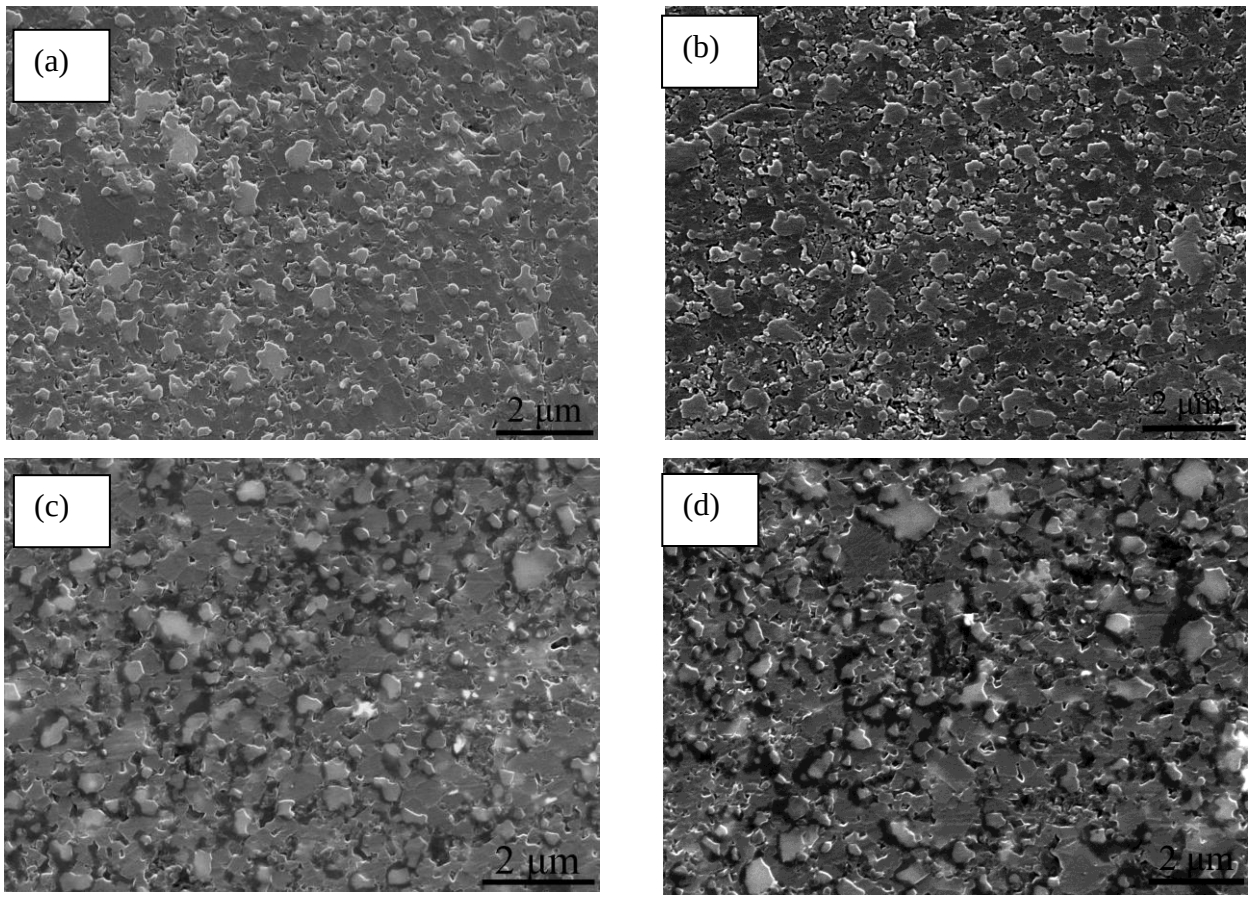

Fig. 4.30. SEM micrographs of the polished surface of the B_4C-SiC composites prepared by SPS at (a) 1700 ˚C and (b)1650 ˚C. The B_4C–SiC–G composite with SPS (c) at 1700 ˚C and (d) 1650 ˚C. The darker grains are B4C and the brighter grains are SiC.

The TEM observations coupled with the XEDS analyses performed on the B_4C–SiC composites, as the ones shown in Fig. 4.31, confirmed the homogeneous dispersion of SiC ultra-fine grains between the B_4C grains, and also revealed another feature of interest, i.e., that the B_4C grains are much larger than the SiC grains. In particular, it is ~540 and 610 nm for the composites without and with graphite, respectively, which is at least twice as large as the SiC grain size. As before, the B4C grain size is also independent on the SPS temperature. The larger B_4C grain size in relation to SiC is consistent with the fact that B_4C is indeed the connected phase in the microstructure, and therefore diffusion of B and C leading to B_4C grain growth is easier. In any case, it can be concluded that SPS is very effective in obtaining fine-grained B_4C-based

ceramics, with the high-energy ball milling assisting in the microstructural refinement (Comparing grain size of pure B_4C with Composites (Table 4.7)).

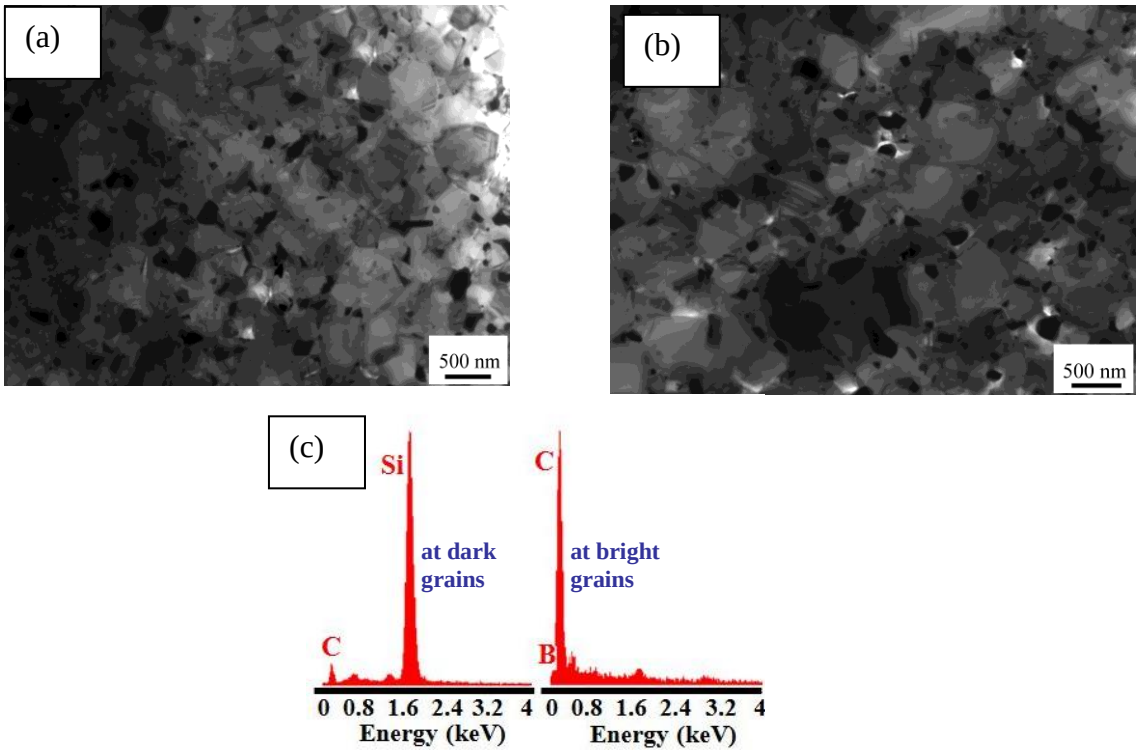

Fig. 4.31. Bright-field TEM micrographs of (a) the B_4C–SiC composite and (b) the B_4C–SiC-G composite, together with (c) the XEDS spectra taken in spot mode at bright and dark grains.

4-3-2- Room temperature mechanical tests

Table 4.8 lists the hardness and toughness values measured by Vickers indentation for B_4C-SiC and B_4C-SiC-G composites. The counterpart of pure B_4C fabricated from the as-received powder under identical SPS conditions also added for comparison (From Table 4.3). Clearly, the hardness decreases with decreasing SPS temperature, which is due to the increase in residual porosity. In agreement with the porosity evolution, the greater fall in hardness occurs in the B_4C ceramic (19.3%), followed by the B_4C–SiC composite (16.3%), and lastly by the B_4C–SiC–C composite (12.3%). Furthermore, for the same SPS temperature the pure ceramic is harder than the composites, which is consistent with the fact that both SiC and graphite are softer than B_4C (i.e., dispersion softening). Specifically, the pure B_4C ceramic is 9 and 5% harder than the B_4C–SiC composite with the SPS at 1700 and 1650 ˚C, respectively, and however, as much as 34% and 23% harder than the B_4C–SiC–C composite. Again, the lower differences in hardness with decreasing SPS temperature correlate well with the porosity data. And finally, the B4C–SiC composites are harder without the graphite addition than with the graphite addition; in particular 24% and 18% harder with the SPS at 1700 and 1650 ˚C.

Given that the composites are denser with graphite, the diminished hardness is due to the larger size of the B_4C and SiC grains (Hall–Petch relationship[107]) and most likely to the presence of residual graphite in the microstructure that softens the composite directly and may also weaken the interfaces.

Table 4.8. Comparison of mean grain size, hardness and fracture toughness values of B_4C-SiC composites and B_4C-SiC-G composites with the counterpart boron carbide samples.

Specimens	Relative density (%)	Mean grain size of B_4C (nm)	Range of SiC grain size (nm)	Mechanical properties		
				Elastic modulus (GPa)	Hardness (GPa)	Toughness (MPa.m$^{0.5}$)
B6 (From Table 4.3)	100	688	-	445	36.4	3.6
B10 (From Table 4.3)	96.8	≈≤688	-		29.4	4.2
BS1	99.4	537	50-250	440	33.6	5.7
BS2	96.6	≈≤537			28.1	6.0
BSG1	100	615	90-300	430	27.2	5.3
BSG2	98.8	≈≤615			23.8	5.5

The toughness exhibits however different trends than the hardness. Firstly, apparently the toughness increases slightly with decreasing SPS temperature from 1700 to 1650 ˚C. However, this is an artefact associated with the residual porosity which helps to dissipate part of the Vickers indentation energy in densification, leaving less elastic energy available to drive crack propagation compared to the full-dense materials. Thus, actually the B_4C ceramic has a toughness of 3.5 MPa m$^{0.5}$, whereas the B_4C–SiC composites have toughness's close to 5.5 MPa m$^{0.5}$ without and with the graphite addition (5.7 and 5.3 MPa m$^{0.5}$, respectively). Secondly, with these numbers it can be concluded that the SiC addition makes B_4C-based ceramics tougher, especially if not combined with graphite addition (i.e., ~65% vs. 50% tougher). This increase in toughness is especially remarkable because the grain sizes in the two B_4C–SiC composites are smaller than in the pure B_4C ceramic, and it is the microstructural coarsening, not the microstructural refinement, that indeed benefits the toughness. Given that the difference in the factor $(E/H)^{0.5}$ does not account for the difference in toughness and that the experimental observation indicated that the radial cracks emanating from the Vickers imprints are much shorter in the B4C–SiC composites, it can be concluded that the SiC grains necessarily induced a marked toughening effect. The examination under the optical microscope of the cracks emanating from the Vickers indents supported this conclusion because the cracks in the pure ceramic were relatively

straight with no deflection while the cracks in the composites with SiC were wavier and more deflected, probably by the SiC grains. The SEM observation of the crack propagation carried out to explore this issue in more detail, as the one presented in Fig. 4.32, shows signs of SiC grains acting as bridges in the B_4C–SiC composites and exerting frictional tractions, from where it can be inferred that the toughening mechanism in the B_4C–SiC composites is essentially crack bridging at the wake of the crack tip by the SiC grains.

The addition of SiC to the B_4C matrix also has a marked influence in the fracture mode. Certainly, as seen previously in Fig. 4.4(a) the fracture surface of the pure B4C ceramic shows evidences of features much larger than its average ~690 nm grain size, indicating that the fracture is transgranular. The fracture surface of the two B_4C–SiC composites shown in Fig. 4.33 (a) and (b) looks clearly different, being rougher with features consistent both in size, population, and distribution with the SiC grains. This reflects that in the B_4C–SiC composites the B_4C matrix fractured transgranularly, whereas the SiC grains did it intergranularly.

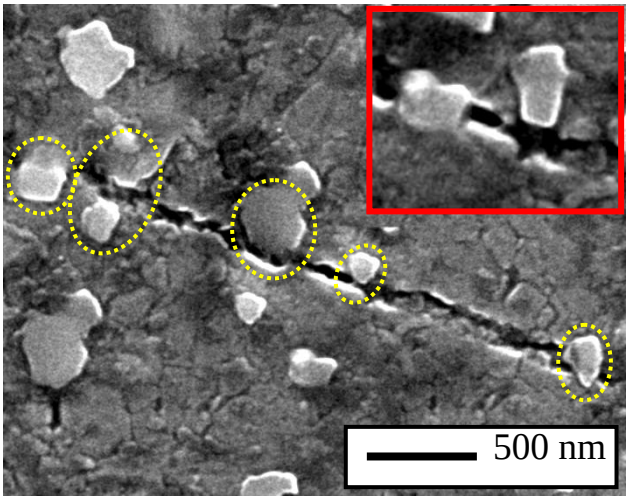

Fig. 4.32. SEM micrograph of the crack propagation in the B_4C-SiC composite with SPS at 1700 ˚C. The darker grains are B_4C and the brighter grains are SiC. Some active or disengaged bridjes have been indicated. The insert is a higher magnification detail showing bridging SiC grains.

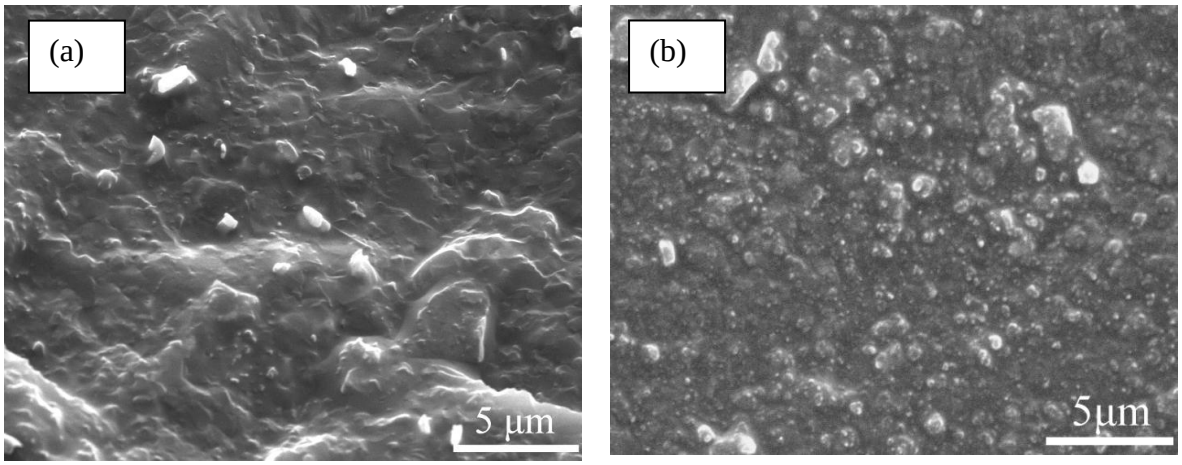

Fig. 4.33. SEM micrographs of the fracture surfaces of the broken: (a) B_4C-SiC composite and (b) B_4C-SiC-C composite prepared by SPS at 1700˚C.

The origin of both crack bridging and change in fracture mode is the thermo-elastic mismatch between B_4C and SiC. It is well-known that thermal expansion mismatch between particle and matrix causes residual stress within and around the particles when the composite cools down from its fabrication temperature. For the case of a single, spherical particle of radius R in an infinite isotropic matrix, a uniform stress, -σ, arises within the particle, and radial and tangential stresses of $-\sigma R^3/r^3$ and $\sigma R^3/2r^3$, respectively, arise around the surrounding matrix, where r is the distance from the centre of the particle to a point in the matrix [109]. These equations represent a satisfactory approximation for the residual thermal stress set up during cooling of the composite containing low concentrations of particles. The stress, σ, is given by the Eshellby analysis [109]:

$$-\sigma_{rad} = 2\sigma_{tan} = \frac{(\alpha_{B4C} - \alpha_{SiC})\Delta T}{\left(\frac{1+\upsilon_{B4C}}{2E_{B4C}} + \frac{1-2\upsilon_{SiC}}{E_{SiC}}\right)}$$

where α and E are the thermal expansion coefficient and Young's modulus, υ is Poission's ratio, ΔT is the temperature difference between processing and room temperature. The parameters α, υ and E of B_4C and SiC are given in Table 4.9. Thus, in the present composite systems where $\sigma_m > \sigma_p$, the particle is subjected to a compressive stress and the matrix to radial compressive and tangential tensile stresses. If the densification temperature is 1700 ˚C, ΔT= 1675 ◦C, predicts radial compressive stresses within the B_4C matrix of ~1.2 GPa and tangential tensile stresses of ~0.6 GPa at the B_4C–SiC interfaces. Therefore, this calculation indicates that the B_4C–SiC interfaces are indeed weak, and this weakness is ultimately responsible for the improved fracture behaviour. In other words, it is expected that the tangential tensile stresses can induce

radial microcracks in the interface around each SiC particles in matrix followed by a partial or full relaxation of the stress. Due to fact that the size of these cracks is small, their presence has positive effects on fracture toughness. So, the toughening mechanisms appear to be deflection of crack propagation, possibly some microcracking and SiC pull-out which are resulted of residual stress generated by the difference in the thermal expansion coefficient between B_4C and SiC in the composites.

Table. 4.9. the values of α, υ and E for B_4C and SiC

Mareials	$\alpha(10^{-6}\ K^{-1})$	E (GPa)	υ
B_4C[110]	6.53	445	0.19
β-SiC[111]	4.5	400	0.19

4-3-3- High-temperature mechanical test

Two boron carbide-15 wt% silicon carbide composites, one doped with 2wt% graphite and the other without graphite sintered by SPS at 1700˚C for 3 min were chosen for high-temperature mechanical test. Fig. 4.34 is a typical creep curve for B_4C-SiC-G composite, where the strain and strain rates were measured at different applied stress stages and temperature jumps. Mechanical tests show that the stress exponent is significantly lower than those measured in pure born carbide specimens. The values are systematically less than unity, with one exception which n value is reached to 3. The activation energy values exhibit a larger scattering: values ranged from 672 until 853 kJ/mol. A mean value for such quantity should be 750 ±250 kJ/mol.

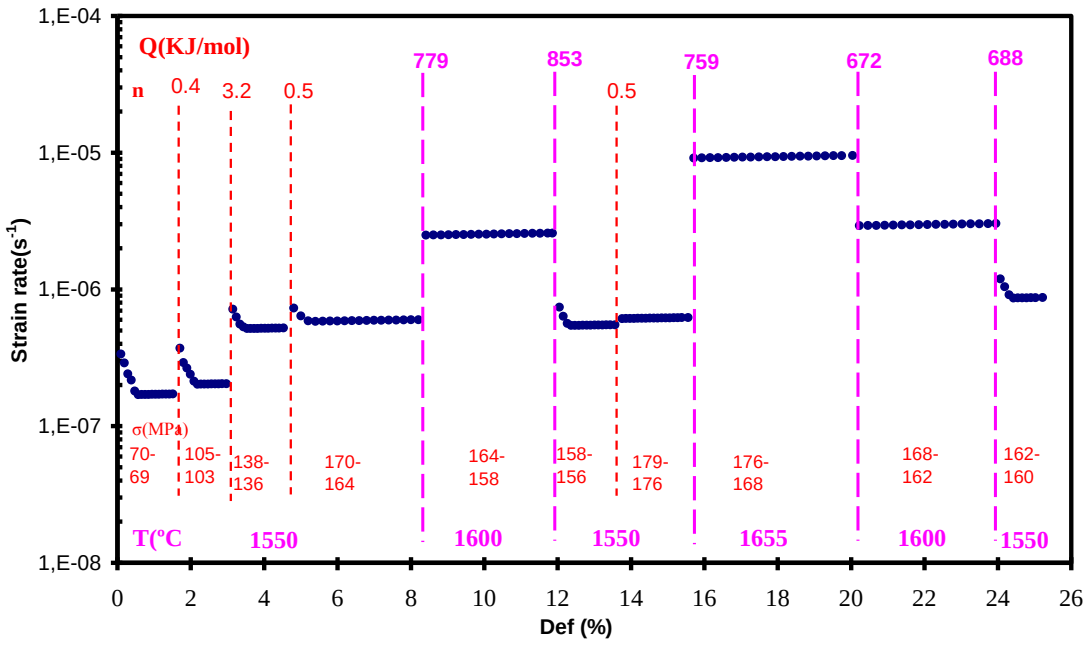

Fig. 4.34. Creep strain rate ($\dot{\varepsilon}_{ss}$) as a function of total % strain (ε) for B_4C-SiC-G composite sintered by SPS at 1700 ˚C for 3min

SEM micrograph of 26% crept B_4C-SiC-G composite is presented in Fig. 4.35. The average size of the B_4C grain after creep deformation is found to be 0.65 μm for composite with graphite, which shows no appreciable difference in the grain sizes. In this case there is some evidence of cavitations.

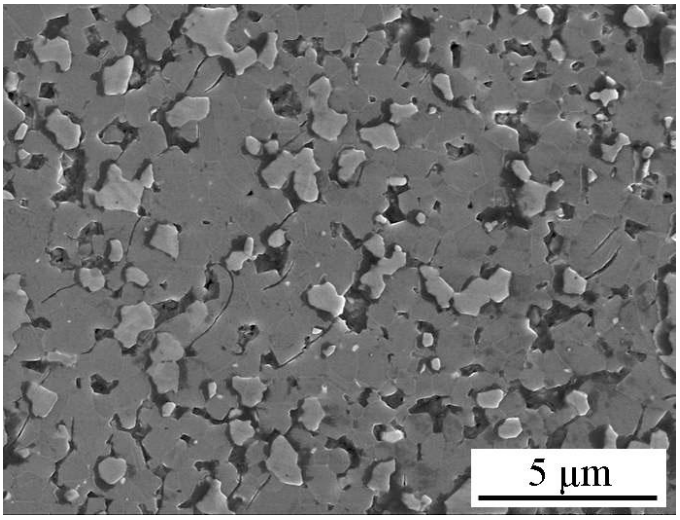

Fig. 4.35. SEM micrograph of 26% crept B_4C-SiC-G composite SPS sintered at 1700 ˚C for 3 min.

Fig. 4.36 shows bright-field and dark-field TEM images of the creep-deformed B_4C-SiC-G composite. A few of the B_4C grains are seen to be twinned. The presence of cavitation is more evident in the crept B_4C-SiC-G composite rather than pure crept boron carbide (Fig. 4.36 (a-b)). The presence of dislocation activity in the creep-deformed B_4C-SiC-G composite was observed just in few grains which was not predominant features in the crept B_4C-SiC-G composite sample (Fig. 4.36(c)).

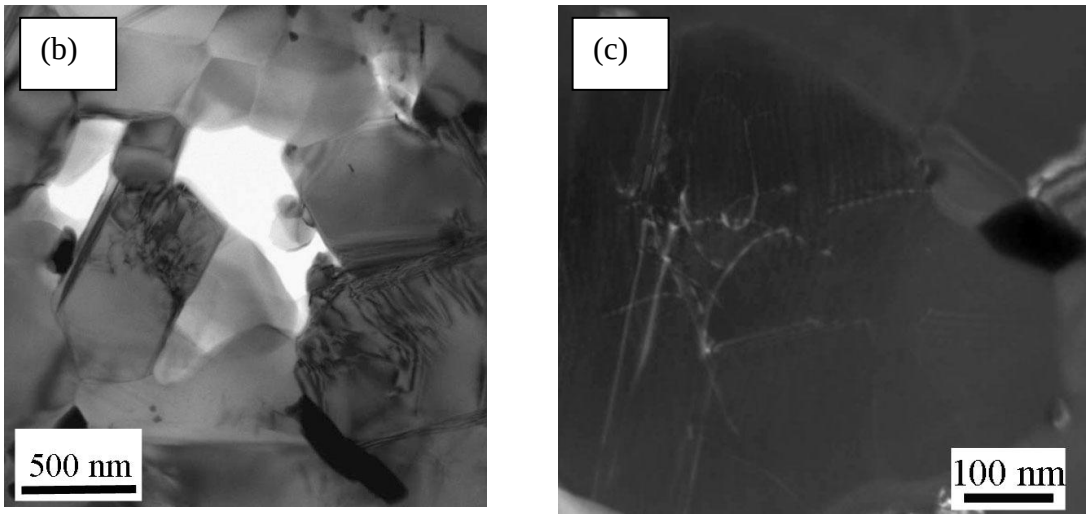

Fig. 4.36. Bright-field and dark-field TEM images of the creep-deformed B_4C-SiC-G composite SPS sintered at 1700 ˚C for 3 min.

In consistency with the model proposed for high-temperature creep, it seems reasonable to suggest that deformation is the result of the combination of grain boundary sliding together with dislocation recovery. Grain boundary sliding is not accommodated by vacancies diffusion: it requires cavities to open up between grains.

Nevertheless, there is a big difference which must be pointed out: the graphite phase facilitates grains to slide each other, making the contribution of grain boundary sliding the dominant one. This is in good agreement with several pieces of evidence:

1-The stress exponents are very close to the value expected by creep with glassy phase, i.e. n=0.5.

2-The smaller scattering in the values of Q are the consequence of better reproducibility of the strain rate values after cyclical jumps. Such partial reproducibility is the consequence of more efficient grain rotations and sliding which consider for the majority of the full strain.

Figures 4.37 show results from constant-load creep tests on B_4C-SiC composite sintered at 1700 °C for 3 under various temperature and stress testing conditions (as indicated). For this sample, the final deformation was around 30%, and the deformation was homogeneous. Both stress exponents and activation energy values display very large scattering: the stress exponents are scattering from unity to values as high as 4 which can be associated to dislocation recovery combined with grain boundary sliding. The several stages show a remarkable non-reproducibility after cyclic jumps, which is at the origin of the large scattering in activation energies. Now without graphite, grain

boundary sliding is much less efficient. This is the reason why stress exponents tend to recovery creep expected values for such quantity.

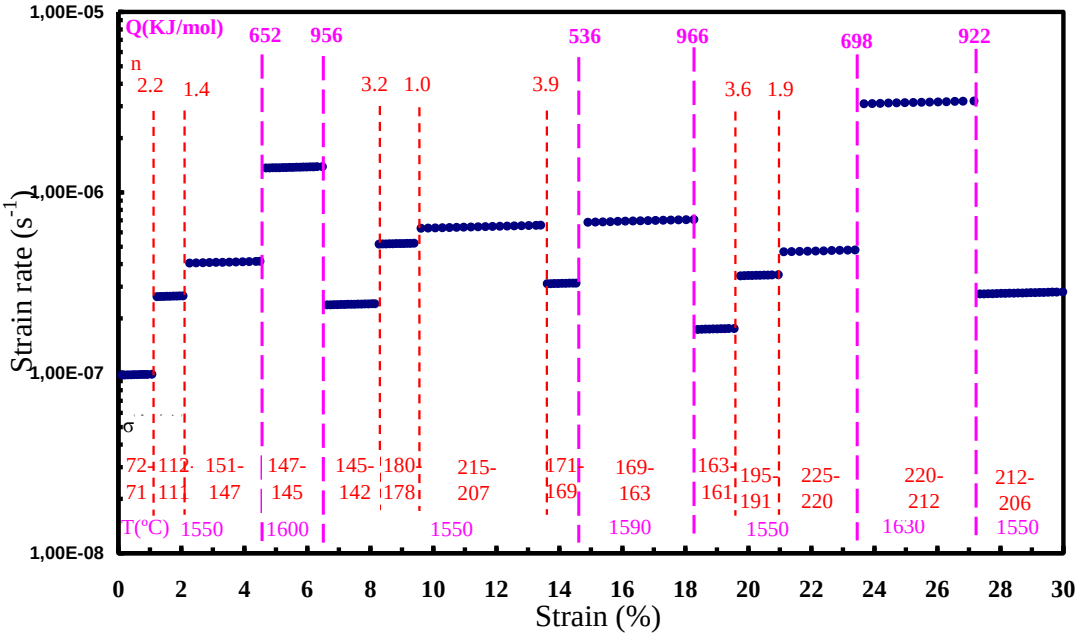

Fig. 4.37. Creep strain rate ($\dot{\varepsilon}_{ss}$) as a function of total % strain (ε) for B_4C-SiC composite sintered by SPS at 1700 ˚C for 3min

The activation energy values exhibit a simillar scattering: values ranged from 536 up to values as high as 966 kJ/mol. This scattering do not allow us to conclude about a mean value for such quantity. In general terms, if only positive jumps are considered (i.e. jumps to higher values of stress), they approach to 630 kJ/mol. This is in agreement with the mean value found in composite with graphite and it would mean that such numerical value is intrinsically linked to a basic atomistic process: mass transport along or to the grain boundaries or through the grains during dislocation recovery.

SEM micrograph of 30% crept B_4C-SiC composite is presented in Fig. 4.38. The average size of the B_4C grain after creep deformation is found to be 0.55 μm, which shows no appreciable difference in the grain sizes. For crept composite without graphite, there is no evidence of cavitations which was observed in crept composite with graphite.

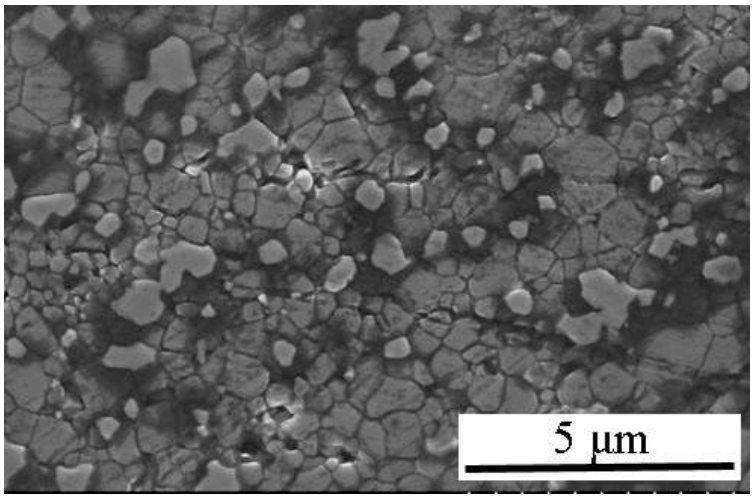

Fig. 4.38. SEM micrograph of 30% crept B_4C-SiC composite SPS sintered at 1700 ˚C for 3 min.

Figures 4.39 are bright-field and dark field TEM images of deformed B_4C-SiC composite (~30% total strain) which show evidence of some twinning, a feature which is favourable in boron carbide (4.39 a). However, the density of twinning is less than crept pure boron carbide. Also, there is evidence for dislocation debris in some grains. The presence of trapped dislocations in twins has been observed by TEM in few grains (Fig. 4.39 (b-c)) as well as the presence of a complicated network of dislocation segments most probably sessile ones (See. Fig. 4.39 (d-e)).

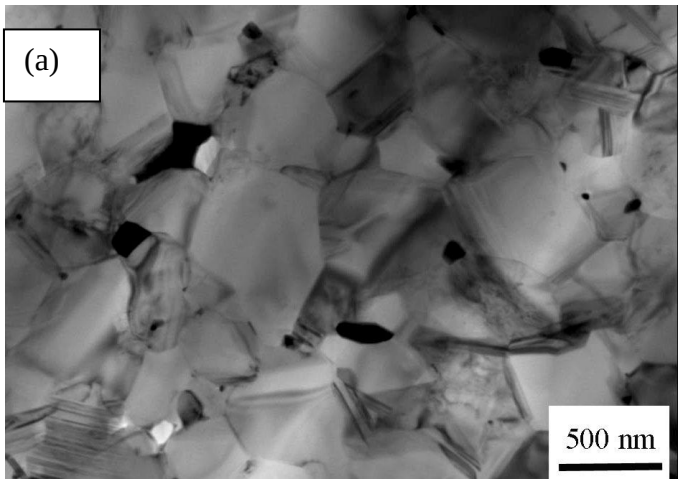

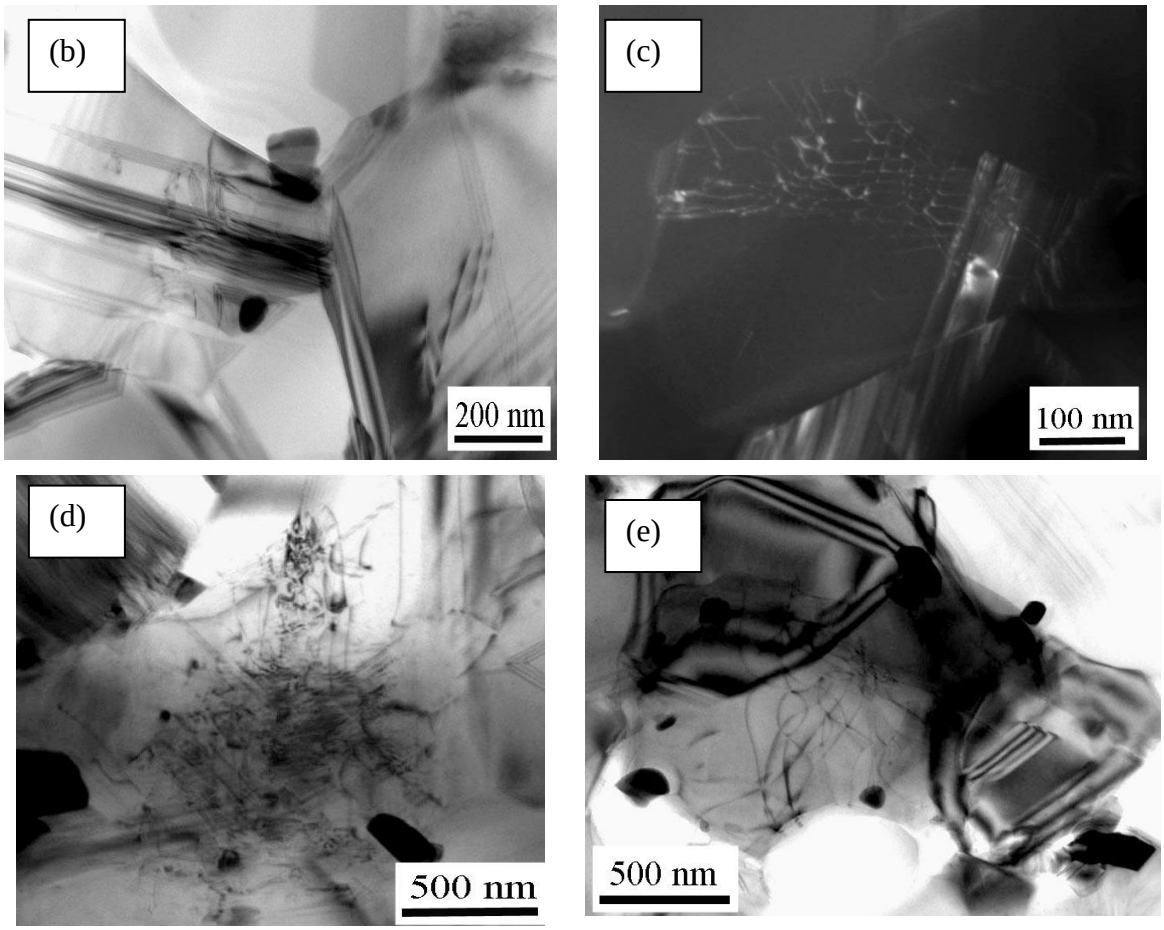

Fig. 4.39. Bright-field and dark-field TEM images of the creep-deformed B_4C-SiC composite SPS sintered at 1700 ˚C for 3 min.

4-4- Nano-B_4C powders (Tekna)

4-4-1- Processing by SPS and characterization

Nano boron carbide powders with average particle size from 40-80 nm were sintered in different procedures in order to improve sinterability of nano-B_4C powder with avoiding grain growth. Three different general approaches were investigated for the possible densification of this B_4C nanopowder with nanograin retention, the three involving the use of spark-plasma sintering. Specifically, the first approach was the SPS of the as-received nanopowder using conventional single-step cycles at 1600, 1700, or 1800 °C for 3 min. The second approach entailed a pre-sintering annealing of the as-received nanopowder at 1150 or 1300 °C (with 5 °C·min^{-1} heating ramp) for 8 h in flowing Ar gas, followed by SPS of the so-annealed nano-powders using conventional single-step cycles at 1600 or 1700 °C for 3 min. And the third approach was the SPS of the as-received nanopowder but this time using two-step cycles, with a first step always at 1200 °C for 10 min followed by a second step at either 1550 °C for 3 min or at 1600 °C for 1 or 3 min. In all cases the SPS was performed in vacuum with 100 °C·min^{-1} heating

ramp and 75 MPa pressure, using graphite dies of 15-mm inner diameter. Table 4.10 shows the processing conditions for the different specimens.

Table.4.10. Processing conditions of nano crystalline boron carbide, density and microstructural features of sintered boron carbide

Sample No.	Sintering condition		Density (%theoretical)	Ave. Grain size	Range of grain size
1	As-rec. Pow: SPS 1800 ˚C-3min-75 MPa-100 ˚C/min↑↓		98.0	2.5 μm	0.83-5 μm
2	As-rec. Pow: SPS 1700 ˚C-3min-75 MPa-100 ˚C/min↑↓		97.1	215 nm	70-430 nm
3	As-rec. Pow: SPS 1600 ˚C-3min-75 MPa-100 ˚C/min↑↓		94.6	100 nm	45-295 nm
4	Anneal: 1300 ˚C-8hr- 5 ˚C/min↑↓	SPS: 1700 ˚C-3min-75 MPa-100 ˚C/min↑↓	99.1	450 nm	170nm-1.5 μm
5	Anneal: 1150 ˚C-8hr-5 ˚C/min↑↓	SPS: 1700 ˚C-3min-75 MPa-100 ˚C/min↑↓	98.5	250 nm	100-580 nm
6	Anneal: 1150 ˚C-8hr-5 ˚C/min↑↓	SPS: 1600 ˚C-3min-75 MPa-100 ˚C/min↑↓	97.5	180 nm	80-460 nm
7	Two step SPS with 75MPa-100 ˚C/min↑↓: First stop 1200 ˚C-10 min Second stop 1700 ˚C-3min		98.7	200 nm	80-415 nm
8	Two step SPS with 75MPa-100 ˚C/min↑↓: First stop 1200 ˚C-10 min Second stop 1600 ˚C-3min		97.0	130 nm	45-350 nm
9	Two step SPS with 75MPa-100 ˚C/min↑↓: First stop 1200 ˚C-10 min Second stop 1600 ˚C-1min		96.6	Not measured	Not measured
10	Two step SPS with 75MPa-100 ˚C/min↑↓: First stop 1200 ˚C-10 min Second stop 1550 ˚C-3min		96.0	Not measured	Not measured

Examination of these results (See Table. 4.10: rows 1 to 3) and images (Figs. 2A and 2B) indicates that the as-received B_4C nanopowder can be reasonably densified by a single-step SPS cycle, but requiring the use of at least 1800 °C to reach no less than 98% densification which unfortunately resulted in remarkable grain growth (i.e., from the ∽40 nm particle size of the as-received nanopowder to the ~ 2.5 μm grain size of the SPSed ceramic). Near-full dense ceramics (i.e., ∽97% relative density) can be also obtained at 1700 °C, but still with a mean grain size in the ultrafine range (i.e., ~215 nm), not strictly in the nanoscale. Certainly, nano-grained B_4C ceramics can be obtained at a lower SPS temperature (i.e., mean grain size of ~100 nm at 1600 °C), but already with uncompleted densification (i.e., ~95% relative density). This limited low-

temperature SPS sinterability has already been observed before in milled B_4C powder (4-2-1), and has been attributed to the B_2O_3 impurities promoting coarsening over densification.

The presence of B_2O_3 impurities in the as received B_4C nano-powders is confirmed by XRD analysis of nano-B_4C powders (Fig. 4.40(a)). In order to improve the sinterability of nano-B_4C and removing of B_2O_3 two main procedures were proposed and performed: First one was SPS sintered samples which nano-powders were pre-heat treated in furnace under a flowing atmosphere of Ar. Second was two step sintering by SPS in which there were two dwell times. First one in lower temperature than sintering is activated with aim of removing boron oxide and second dwell time is at sintering temperature. The details of sintering process related to all prepared samples are provided in Table. 4.10.

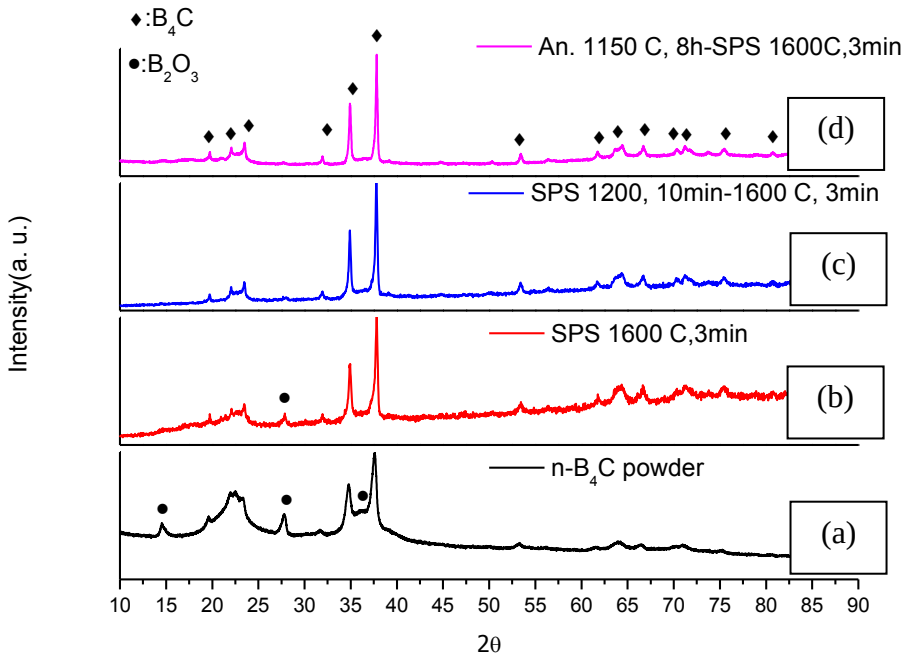

Fig. 4.40. (a) XRD patterns for n-B_4C powders, (b) SPS sintered n-B_4C at 1600 ˚C for 3 min from as-received n-B_4C powders, (c) two step SPS sintered n-B_4C at 1200 for 10 min and later on 1600 ˚C for 3 min and (d) SPS sintered n-B_4C at 1600 ˚C for 3 min from annealed n-B_4C powders at 1150 ˚C for 8h.

The experimental density of sintered samples in different conditions was reported in Table 4.10. It can be seen that retarding of densification in nano-powder is remarkable, because smaller particle size resulted in the larger specific surface area and higher possibility of formation of boron oxide on the B_4C particles. But, sintering by SPS could improve densification of this nano-powder rather than conventional technique[50].

The highest density can be obtained in samples which nano-powders were pre-heat treated or in samples with two step SPS with limited grain growth.

XRD analysis of SPS sintered samples at the maximum temperature of 1600 ˚C prepared in three different conditions; i.e. sample No. 3, 6 and 8 from Table 4.10, is shown in Fig. 4.40. The presence of boron oxide in directly SPS sintered sample at 1600 ˚C is detected in XRD pattern (Fig. 4.40(b)). However the peaks related to boron oxide are smaller compare with nano-powders and the amorphous halo is reduced (Fig. 4.40(a-b)). In the case of the sample which was prepared with two step SPS at 1200 ˚C for 10 and later at 1600 ˚C for 3 min, the amount of boron oxide is smaller that the limit of detection by XRD (Fig. 4.40(c)). The same result was observed for the sample which was prepared from the annealed powder at 1150 ˚C for 8 h (Fig. 4.40(d)). Both cases are effective to remove the boron oxide, giving rise to improved sinterability of nano-powder considerably (See Table. 4.10).

The cross-sectional microstructure of both polished and electrolytically etched specimens are shown in Fig. 4.41. The average grain size was measured for all sintered samples by SEM. An enhanced grain growth was observed in the sample sintered at 1800 ˚C for 3min (Fig. 4.41(a)). Enhanced grain growth happened at this temperature, together with some pores trapped inside the grains and along the grain boundaries. However density did not reach to theoretical density. Isolated islands contained of nano-grains with diameter of around 40 nm were observed in some grain boundaries (white arrows) and some individual nano grains or pores trapped inside coarse grains (Fig. 4.41(a-inset)). The average grain size in this sample ignoring these nano-grains (a small fraction compares to the number of coarse grains) is 2.5μm. Also the twinning is obvious in this SEM micrograph that is resulted from pressure during SPS. Reducing sintering temperature results in a notable decrease in grain size. Sintering at 1600 ˚C is the optimal sintering temperature with reduced grain growth in which average grain size is around 100 nm with very narrow grain size distribution from 45 to 300 nm Fig. 4.41(b). On contrary, in this sintering temperature, density drop to 94.6%. In this sample, the prosity is interconnected to form elongated pores, although some dense regions consisting of several grains have formed. Also the glassy phase in grain boundaries and in porosities was observed by SEM (Fig. 4.41(b)). In the sample sintered at the same temperature of 1600 ˚C with pre-heat treatment on nano-powders, obvious improvement in density up to 97.5% was observed and the average grain size is around 180nm (Fig. 4.41(c)). This improvement was also observed in two step SPS sintered sample at same temperature of 1600 ˚C which results in average grain size of

around 130nm which is lower than sintered sample from annealed powder (Fig. 4.41(d)). Both methods for removing boron oxide are successful and fine grains with smaller and more uniformly distributed pores are produced. Among these two proposed procedures, two step SPS is very easy and a time-saving method which is efficient to remove boron oxide in shorter time and n-B4C with smaller grain size and optimal density obtained.

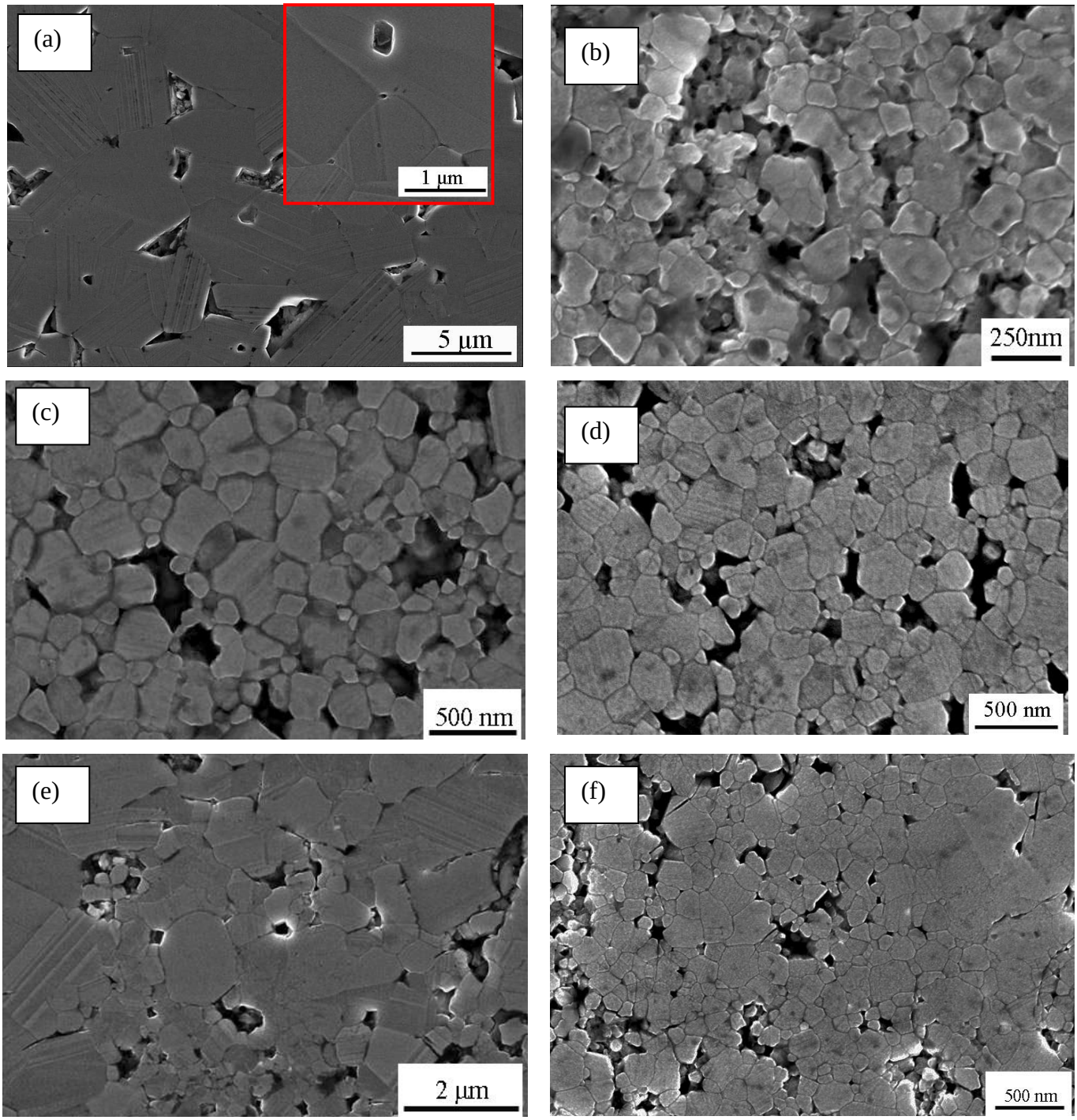

Fig. 4.41. SEM micrographs of sintered nano-crystalline boron carbide: (a) SPS sintered B_4C at 1800 ˚C for 3 min from as-received n-B_4C powders, (b) SPS sintered n-B_4C at 1600 ˚C for 3 min from as-received n-B_4C powders, (c) SPS sintered n-B_4C at 1600 ˚C for 3 min from annealed n-B_4C powders at

1150 ˚C for 8h, (d) two step SPS sintered n-B_4C at 1200 for 10 min and later on 1600 ˚C for 3 min, (e) SPS sintered n-B_4C at 1700 ˚C for 3 min from annealed n-B_4C powders at 1350 ˚C for 8h, (d) two step SPS sintered n-B_4C at 1200 for 10 min and later on 1550 ˚C for 3 min.

Unfortunately in all the samples there is evidence of limited abnormal grains in microstructures. This can be attributed to two possible explanations: First, the presence of boron oxide as a glassy phase which promotes grain growth by providing a rapid diffusion path on particle surface or by vapor-phase transport because of volatility of boron oxide[85]. In order to eliminate this abnormal grain, annealing of nano-powders at higher temperature of 1300 ˚C for 8 h before SPS was tried. This temperature is high enough to remove boron oxide completely (See. 4.2.1). However, abnormal grains on microstructure were also observed (Fig. 4.41 (e) white arrow). The second possibility of coarsening is the consequence of high curvature of nano-grains which result in diffusional currents from sites of higher curvature, e.g., nano-grains to sites of lower curvature, e.g., large pores and provide abnormal grains there. With the aim of limiting abnormal grains, sintering at lower temperature of 1550 ˚C and less dwell time for 1 min was tested but it was not completely efficient and abnormal grains were observed (Fig. 4.41(f)) and on the other hand density was dropped. In processing of nano-boron carbide, the grain curvature gradients are very high. These gradients are the driving force for coarsening as soon as sintering is activated. In this sense, a fast technique like SPS can help limiting the coarsening of grains in short time of sintering and it is observed that the numbers of abnormal grains are very limited compared to the number of nano-grains (See Fig. 4.41 (f)).

Further details of the microstructure are shown in TEM micrographs of SPS sintered sample at 1600 ˚C and two step SPS sintered sample at 1200-1600 ˚C (Fig. 4.42). The most important feature is the presence of nano-twinning in the majority of the grains (Fig. 4.42a inset) which was not observed in nanocrystalline boron carbide prepared by hot press[50]. Another microstructural feature is the presence of nano porosity in triple point of grain boundaries that are higher concentration and bigger in size for the sintered sample with as-received nano-powders. Also the glassy phase was observed in grain boundaries and triple points in this sample which was observed also in X-ray analysis (Fig. 4.42b).

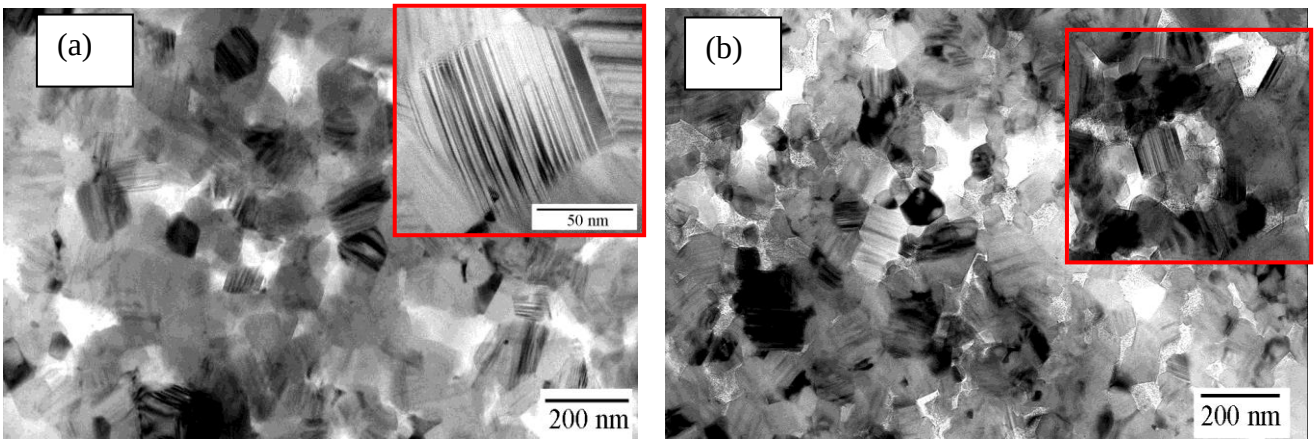

Fig. 4.42. Bright-field TEM micrographs of sintered nano-crystalline boron carbide: (a) two step SPS sintered n-B_4C at 1200 for 10 min and later on 1600 ˚C for 3 min and (b) SPS sintered B_4C at 1600 ˚C for 3 min from as-received n-B_4C powders.

4-4-2- Room temperature mechanical tests

The sintered samples with higher density and minimized average grain size were considered for further study of hardness by Vickers indentation (Table. 4.11). The results showed that the Vickers hardness is improved to the value as high as 32 GPa, considerably higher than those found in nano-crystalline sintered by hot press at the same temperature at the pressure of 980MPa for 1h[50]. Improvement in hardness can be attributed to the efficiency of two step SPS and /or pre-heat treatment of nano-powder to remove amorphous boron oxide and higher density of the nano-boron carbide prepared by SPS. Also the presence of high density of twin boundaries results in a superior hardness compared with hot press naocrystalline boron carbide in which twinning was not observed[50]. It is reported a higher density of twin boundaries exhibits more superior mechanical properties[112]. The hardness values from n-B4C samples are lower than micrometric boron carbide powder sintered by SPS which is the consequence of lower density obtained with nano-powders (Compare table 4.11 with 4.3 and 4.6).

Fracture toughness of n-B_4C was measured by the crack length extending from the corners of Vickers indentations (Table.4.11). Results show high values of 4.1-4.6 MPa.$m^{1/2}$ which is similar to those obtained by hot press from nano-powders[50]. These values are considerably higher than those of microcrystalline boron carbide (Compare table 4.11 with 4.3 and 4.6) which is expected because of nano-grains specially grains below 100 nm are very effective in deflection of crack path, an efficient mechanism for energy dissipation at the crack tip (Fig. 4.43 (a)). Also there is some evidence of nano-grains acting as bridge on crack path (Fig. 4.43 (b-inset)). The other energy dissipative process is nano-grain pull-out that was observedin crack path as shown in Fig. 4.43(b).

On the other hand, the presence of porosity, which acts as crack arrestors, results in higher values of fracture toughness. It can be observed from SEM image (Fig. 4.43 (a)), however, the crack propagated is in transgranular mode for grains higher than 100 nm, in contrary grains less than 100 nm are able to change the crack path to intergranular mode.

Table. 4.11. Comparison of mean grain size, hardness and fracture toughness values for nano crystalline boron carbide.

Sample No.	Sintering condition	Density (%theoretical)	Ave. Grain size	Range of grain size	Hardness (GPa)	Fracture toughness (MPa.m1/2)
3	As-rec. Pow: SPS 1600 ˚C-3min-75 MPa-100 ˚C/min↑↓	94.6	100 nm	45-295 nm,	22.8	4.61
6	Anneal: 1150 ˚C-8hr-5 ˚C/min↑↓ | SPS: 1600 ˚C-3min-75 MPa-100 ˚C/min↑↓	97.5	180 nm	80-460 nm	32.5	4.12
8	Two step SPS with 75MPa-100 ˚C/min↑↓: First stop 1200 ˚C-10 min Second stop 1600 ˚C-3min	97.0	130 nm	45-350 nm	31.0	4.29

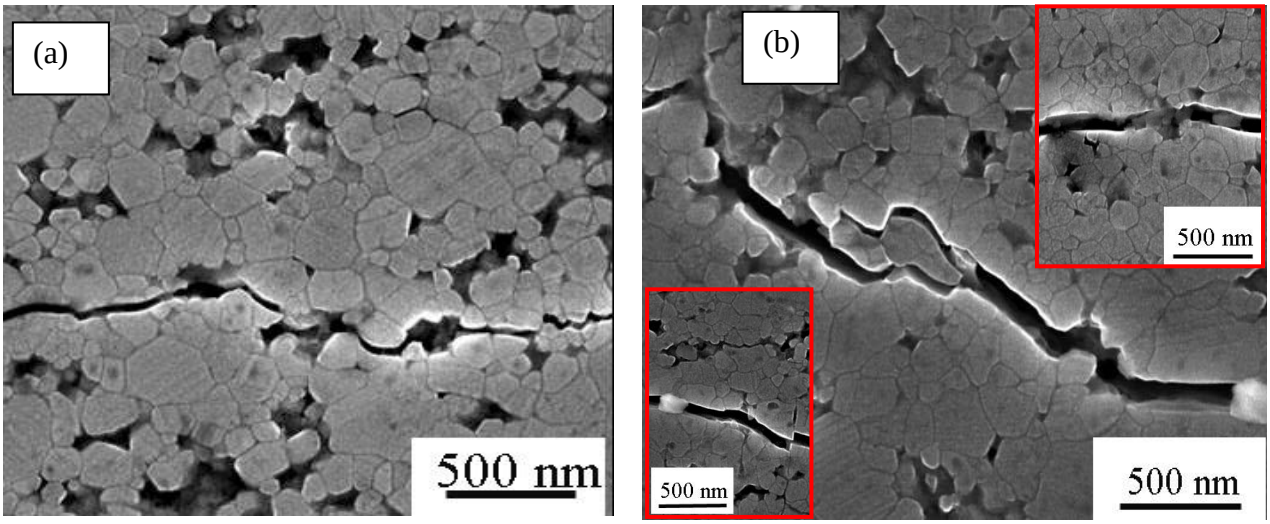

Fig. 4.43. SEM micrograph of crack propagation for sintered nano-crystalline boron carbide: two step SPS sintered at 1200 for 10 min and later on 1600 ˚C for 3 min

The fractured surface of n-B_4C samples sintered by SPS at 1600 ˚C from as-received nano-powders and two step SPS sintered sample at 1200-1600 ˚C are shown respectively in Fig. 4.44 a and b. In the SPS-ed sample from as-received nano-powders, fracture surface has intergranular behavior with the presence of elongated pores which reveals the weak interfaces between nano grains, with the presence of boron oxide amorphous phase in grain boundaries. In consequence the higher fracture toughness is obtained in this n-B4C sample. For the sample with two step SPS, the fracture

toughness microstructural observation shows a rough fracture surface with features of nano grains of lower than 100nm extended on the fracture surface(Fig. 4.44 (a)), which are fractured transgranularly and intergranular cleavage steps higher than 100nm.

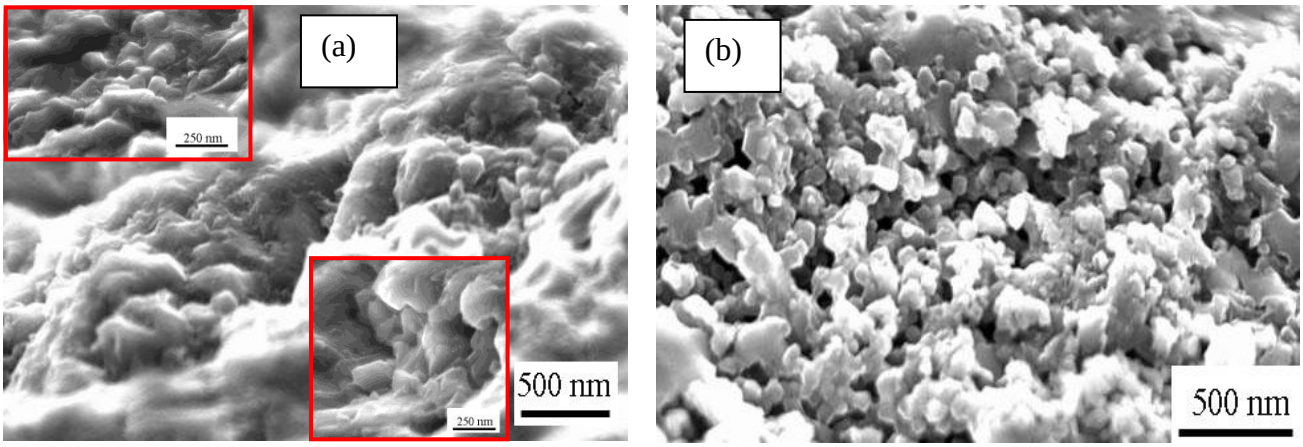

Fig. 4.44. SEM micrograph of fracture surface of sintered nano-crystalline boron carbide: (a) two step SPS sintered n-B_4C at 1200 for 10 min and later on 1600 ˚C for 3 min and (b) SPS sintered B_4C at 1600 ˚C for 3 min from as-received n-B_4C powders.

4-4-3- High-temperature mechanical test

In order to study mechanical properties of nano-B_4C, several creep tests were performed in which samples sintered with different conditions were used. Fig. 4.45 shows a creep result as a strain rate versus strain plot for SPS sintered B_4C at 1800 ˚C for 3 min from as-received n-B_4C powders. As it is mentioned before average grain size of sintered sample was 2.5 μm. The total deformation was around 35% and the sample deformed homogenously. The scattering of stress exponent values is less compare with B_4C samples with sub-micrometric grains (Fig. 4.6 and Fig. 4.27) and they are between 2.4 to 4.6. In the case of activation energy the same trend is observed that value of this parameter is between 666 to 830 kJ/mol.

SEM and TEM photographs of 35% crept sample from SPS sintered B_4C at 1800 ˚C for 3 min from as-received n-B_4C powders are shown in Fig. 4.46 and 4.47, respectively. Densification was performed during compression creep test and in consequence the amount of porosity is decreased compare to sintered B4C (Fig. 4.41 (a)). The measured average grain size of crept sample by SEM image is estimated around 3.7 μm. A comparison of Figs 4.46 and 4.41(a) confirms that the microstructural scale of the B_4C ceramic has not changed after creep deformation. One important feature in SEM observation of 35% crept sample with coarsened microstructure is the presence of transgranular microcracks which is consequence of large deformation. Normally cracks extended from the large grains in to the fine grains. This was not found in fine

crystalline microstructure deformed boron carbide samples even with larger deformation. The presence of twinning that is not surprising can be observed in 35%crept sample by SEM and TEM micrographs (Fig. 4.46 and 4.47) and the most important feature in TEM micrograph is the interaction of twinning and dislocations (Fig. 4.47).

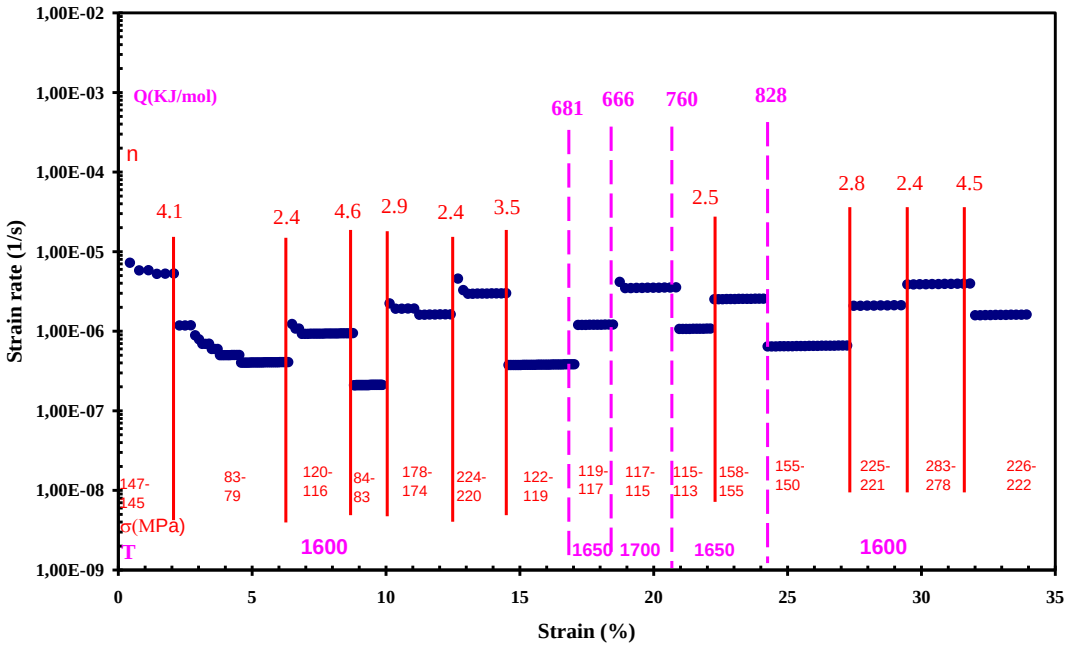

Fig. 4.45. Creep strain rate ($\dot{\varepsilon}_{ss}$) as a function of total % strain (ε) for SPS sintered B_4C at 1800 ˚C for 3 min from as-received n-B_4C powders.

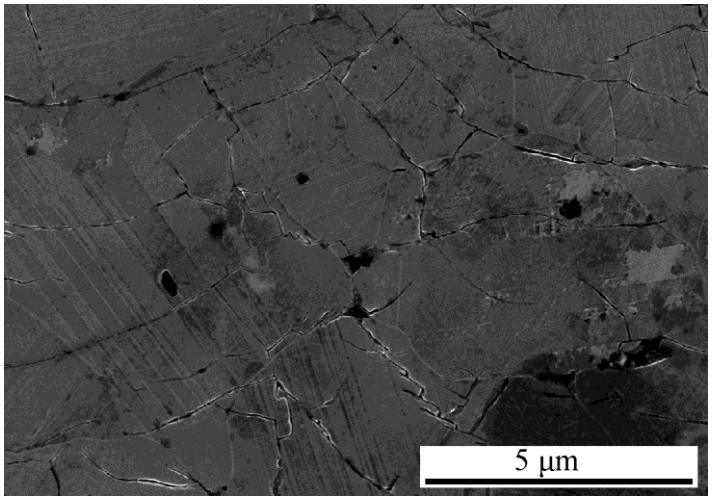

Fig. 4.46. SEM micrograph of 35% crept B_4C ceramic SPS sintered at 1800 ˚C for 3 min from as-received n-B_4C powders.

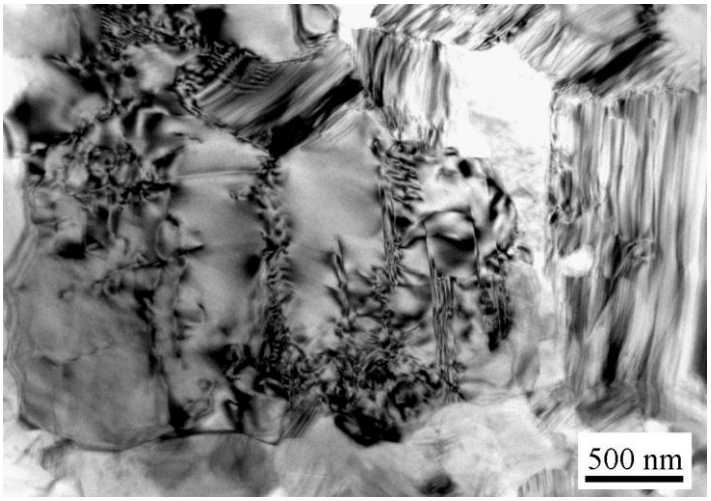

Fig. 4.47. TEM micrograph of 35% crept B_4C ceramic SPS sintered at 1800 ˚C for 3 min from as-received n-B_4C powders.

In order to investigate the role of nano-crystalline structure on high temperature mechanical properties, the nano-B_4C samples with higher density and minimized average grain size were considered which were; two step SPS sintered n-B_4C at 1200 for 10 min and later on 1600 ˚C for 3 min, SPS sintered n-B_4C at 1600 ˚C for 3 min from as-received n-B_4C powders and SPS sintered n-B_4C at 1600 ˚C for 3 min from annealed n-B_4C powders at 1150 ˚C for 8h. The more details of microstructural features are provided previously in Table. 4.11.

Figures 4.48 a and b show results from constant-load creep tests on two individual nano-B_4C samples prepared from two step SPS sintered at 1200 for 10 min and later on 1600 ˚C for 3 min. The average grain size of sintered n-B_4C was around 130 nm. The creep tests were terminated at total deformation of ~35% in Figs. 4.48 a and b, respectively, with the samples intact. Surprisingly, nano-B_4C samples in these conditions were deformed inhomogeneously with S-shape (Fig. 4.49) and shiny edges in lateral surfaces parallel to compression force axis were observed. Transient creep was observed specially in few first sections of deformation with the change of testing conditions which were related more to densification of samples and for other sections, the creep rate is found to reach a steady state immediately (Figs. 4.48 a and b). The estimated values of n and Q respectively, are included in Figs. 4.48 a and b, and are observed to vary widely and to higher values compare with values obtained from crept micrometric boron carbide (Fig. 4.6 and Fig. 4.27): n = 0.8 to 12 and Q = 725 to 1308 kJ.mol^{-1}. The unprecedented behaviour of B_4C deformation was observed also here in which the $\dot{\varepsilon}_{ss}$ for a given σ-*T* test condition, following a higher $\dot{\varepsilon}_{ss}$ excursion, is always

lower ("hardening") than the original $\dot{\varepsilon}_{ss}$ even when the original σ-*T* test condition is restored.

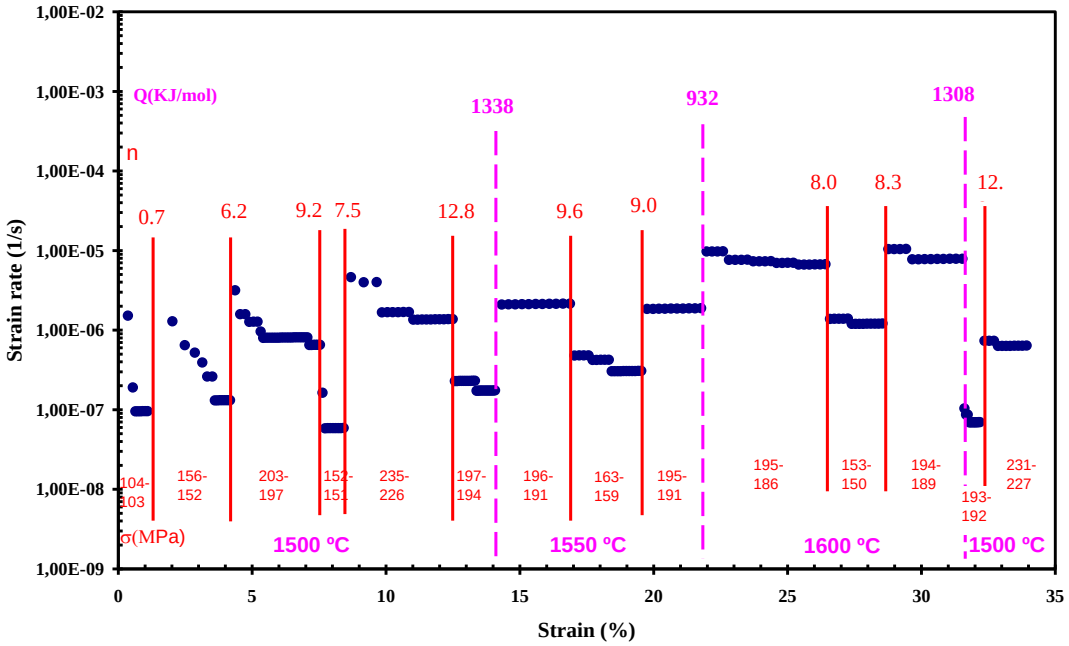

(a)

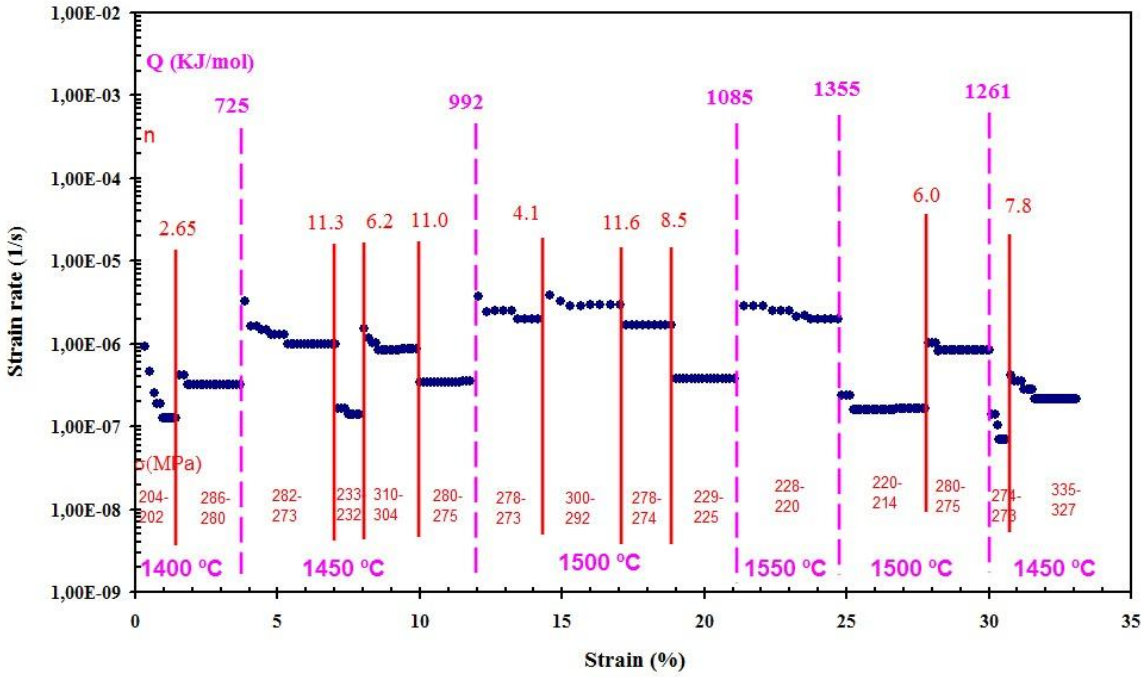

(b)

Fig. 4.48. Creep strain rate ($\dot{\varepsilon}_{ss}$) as a function of total % strain (ε) for n-B_4C samples from two step SPS sintered at 1200 for 10 min and later on 1600 ˚C for 3 min.

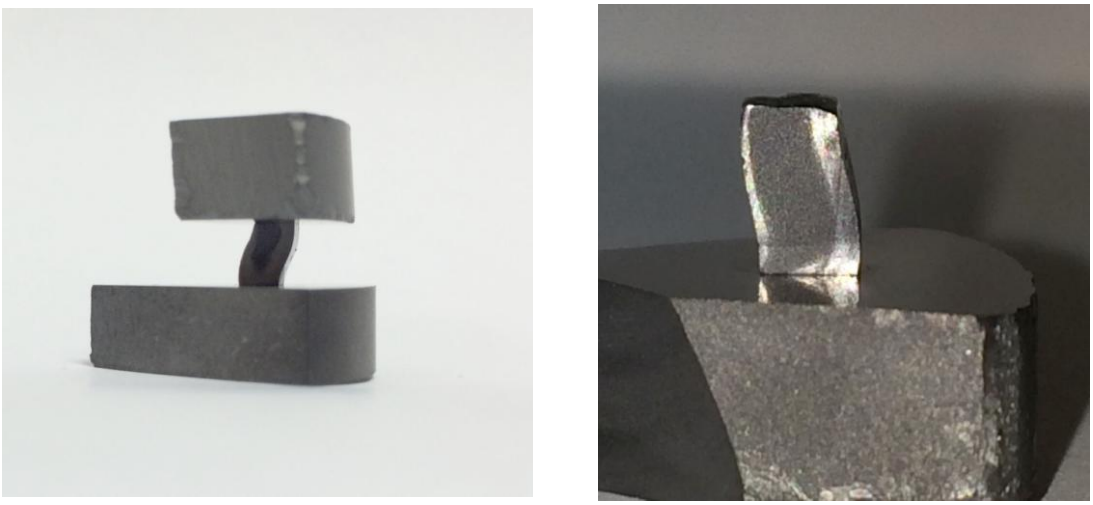

Fig.4.49. Inhomogeneously or S-shape 35% crept n-B4C sample prepared from two step step SPS sintered at 1200 for 10 min and later on 1600 ˚C for 3 min.

SEM and TEM photographs of 35% crept n-B_4C sample from two step SPS at 1200 ˚C for 10min and 1600 ˚C for 3 min are shown in Fig. 4.50 and 4.51, respectively. Densification was performed during compression creep test and in consequence the amount of porosity is decreased compare to sintered n- B4C (Fig. 4.41 (d)). The measured average grain size of crept sample by SEM image is estimated at 220nm while grain size distribution is from 55 nm to 460 nm. A comparison of Figs 4.50 and 4.41(d) confirms that the microstructural scale of the n-B_4C ceramic has not changed after creep deformation.

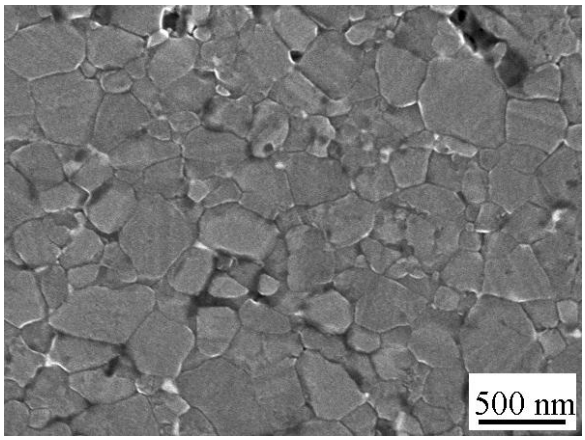

Fig. 4.50. SEM micrograph of 35% crept n-B_4C ceramic two step SPS sintered at 1200 ˚C for 10 min and 1600 ˚C for 3.

TEM images of deformed n-B_4C (~35% total strain) show evidence of high density of nano-twinning in most grains (4.51(a)). The presence of trapped dislocations with nano-twins has been observed by TEM in most grains (Fig. 4.51 (b-e)).

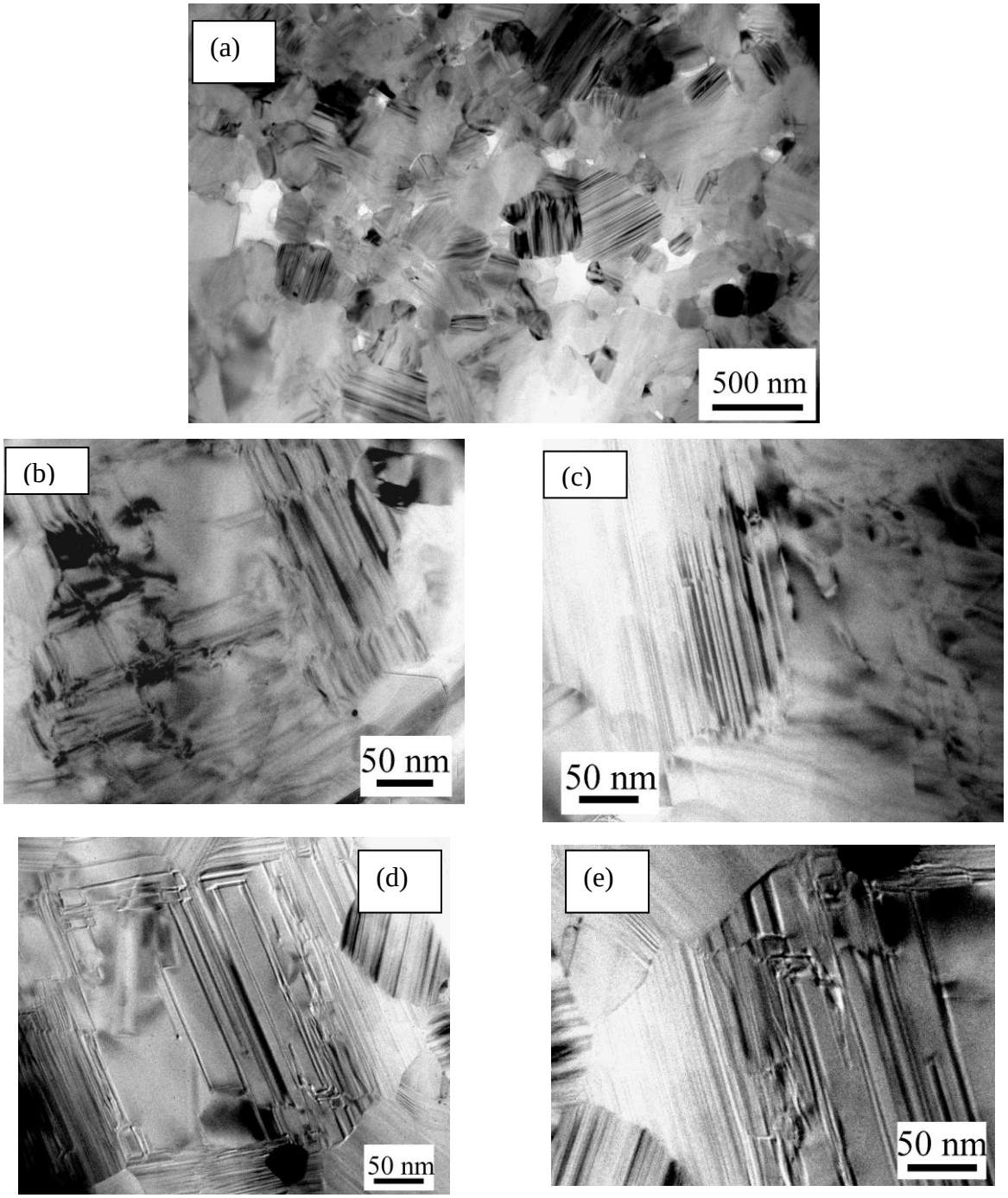

Fig. 4.51. TEM micrograph of 35% crept n-B_4C ceramic two step SPS sintered at 1200 ˚C for 10min and 1600 ˚C for 3.

In other experiments, n-B_4C samples were deformed with higher strain rate at higher temperature (Fig. 4.52 (a)) and this creep test followed few first sections of the creep test performed on micrometric B_4C sample (Fig. 4.6 (b)) in order to compare creep resistance regarding to importance of nano-scale on creep rate. In this case, creep test were terminated at total deformation of ~22% in Figs. 4.52 (a) with the samples intact. Surprisingly with applying high strain rate of 10^{-4} at high temperature of 1600 ˚C, the deformation mode changes again to homogeneous deformation. Although, some micro-

cracks were observed on lateral surface parallel to deformation axis as shown in Fig. 4.52 (b). In other test with applying high strain rate of 10^{-4} at high temperature of 1600 ˚C which is sintering temperature, deformation was continued by as much as ~125% without failure (Fig. 4.52 (c)) until deformation was exhausted. These are remarkably high creep strains for a covalently-bonded brittle ceramic and en contrary of the other n-B_4C samples homogenous deformation was observed as it is shown in Fig. 4.52 (d).

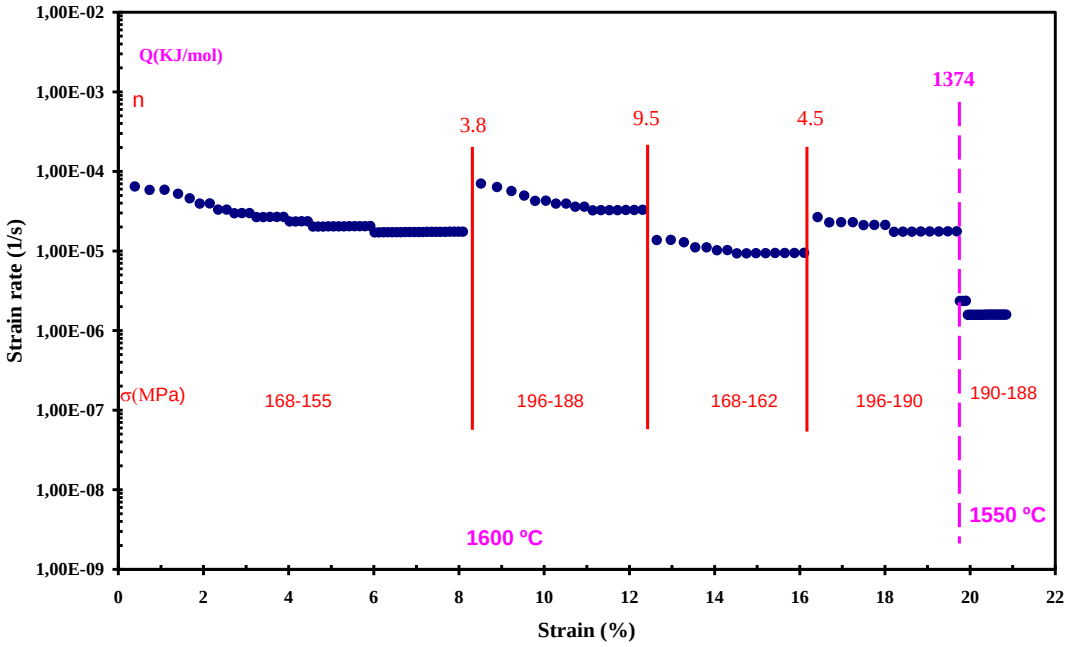

(a)

(b)

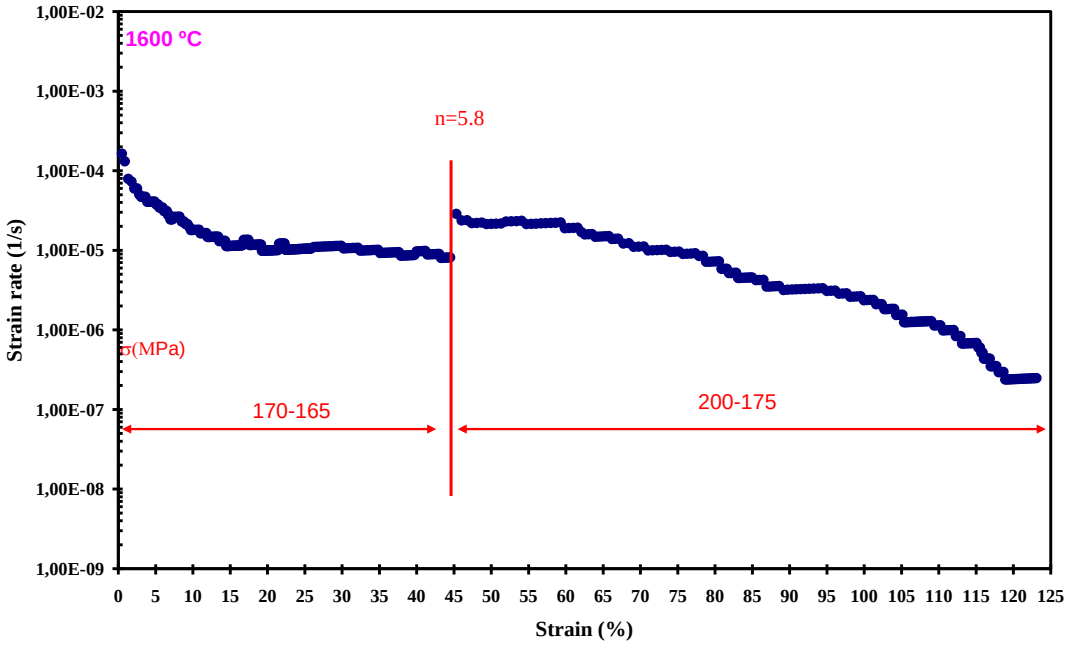

(c)

(d)

Fig. 4.52. Extreme deformation of n-B_4C without failure

As mentioned before, creep test was performed also for n-B4C sample SPS sintered at 1600 ˚C for 3 min from annealed n-B_4C powders at 1150 ˚C for 8h. The average grain size of sintered sample was 180nm. The plot of strain rate versus strain as a typical creep test for this n-B4C sample is shown in Fig. 4.53. This creep test followed few first sections of the creep test performed on n-B4C sample prepared by two step sintering (Fig 4.48 (a)). In this case, creep test were terminated at total deformation of ~20% in Figs. 4.53 with the samples intact. Again nano-B_4C sample was deformed inhomogeneously with S-shape. The deformation behaviour was very similar in which transient creep was observed similarly in few first sections of deformation with the change of testing conditions which were related more to densification of samples and for other sections, the creep rate is found to reach a steady state immediately (Figs.

4.53). The estimated values of n and Q respectively, are included in Figs. 4.53 and are observed to have similar trend (Fig. 4.48 (a)): n = 0.85 to 12.3 and Q = 1078 to 1335 kJ.mol^{-1}.

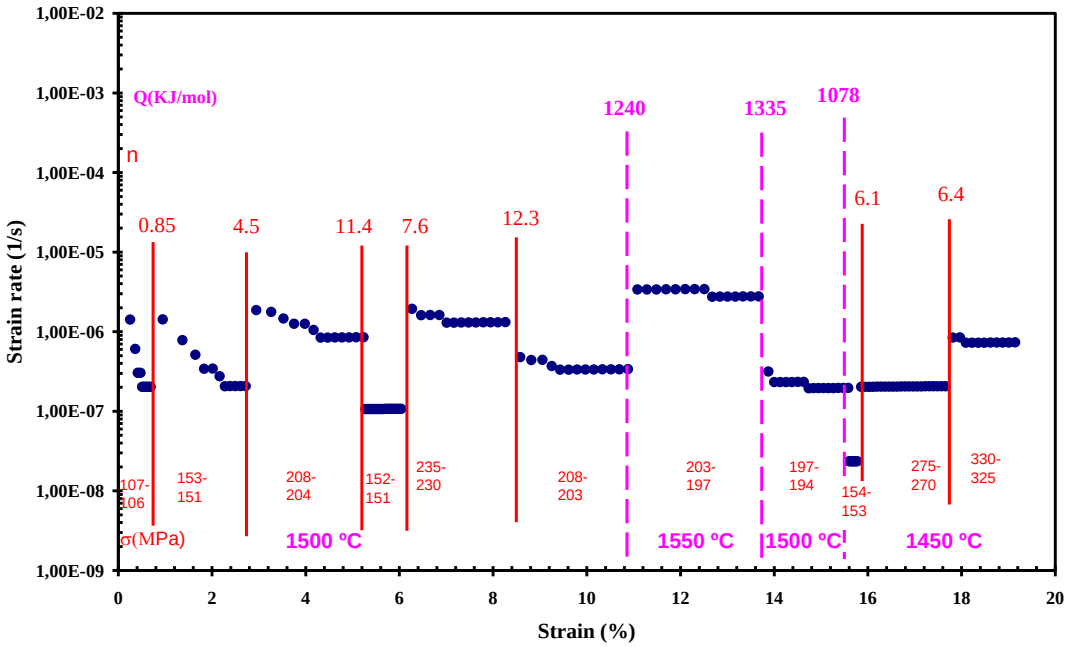

Fig. 4.53. Creep strain rate ($\dot{\varepsilon}_{ss}$) as a function of total % strain (ε) for n-B_4C sample prepared by SPS at 1600 ˚C for 3 min from annealed n-B_4C powders at 1150 ˚C for 8h.

Finally creep tests were also performed on the two individual n-B4C samples sintered by SPS at 1600 ˚C for 3 min from as-received n-B_4C powders. The results are provided in Fig. 4.54. The average grain size of sintered sample was 100nm. The first creep test (Fig. 4.54 (a)) followed few first sections of the creep test performed on n-B4C sample prepared by two step sintering (Fig 4.48 (a)). In this case, creep test were terminated at total deformation of ~26% in Figs. 4.54 with the samples intact. Again nano-B_4C sample was deformed inhomogeneously with S-shape. The transient creep was observed similarly in few first sections of deformation with the change of testing conditions even with higher percentage which were related more to densification of samples and for other sections, the creep rate is found to reach a steady state immediately (Figs. 4.54). The other important feature from creep tests is the higher strain rate at the same stress and temperature compare with counterpart crept n-B_4Csamples from two step SPS (4.48 (a)) and SPS sintered from annealed n-B_4C powders (4.53). The estimated values of n and Q respectively, are included in Figs. 4.54 and are observed to have similar trend (Fig. 4.48 and 4.53): n = 0.83 to 11.8 and Q = 945 to 1448 kJ.mol^{-1}.

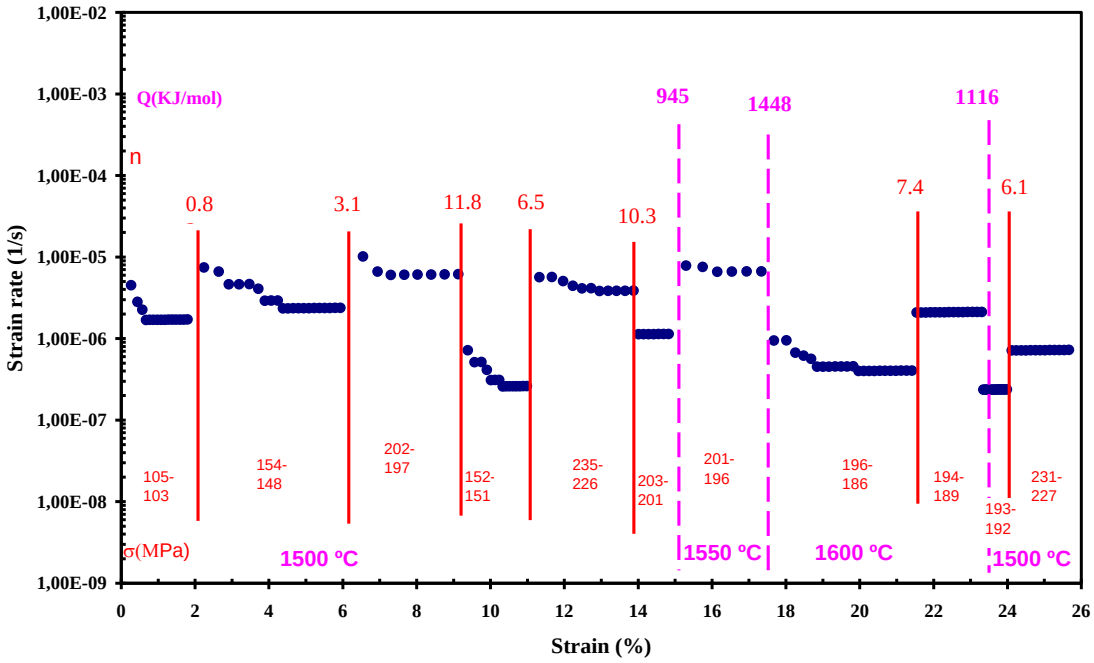

(a)

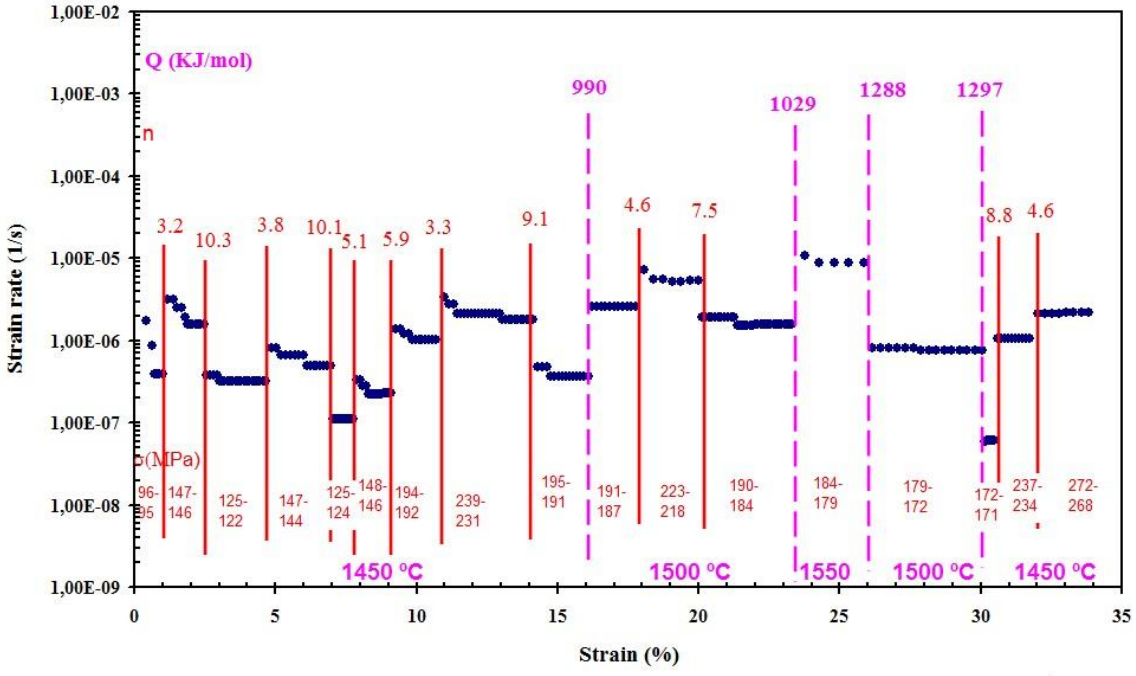

(b)

Fig. 4.54. Creep strain rate ($\dot{\varepsilon}_{ss}$) as a function of total % strain (ε) for n-B_4C samples sintered by SPS at 1600 ˚C for 3 min from as-received n-B_4C powders

SEM and TEM photographs of 26% crept n-B_4C sample sintered by SPS at 1600 ˚C for 3 min from as-received n-B_4C powders are shown in Fig. 4.55 and 4.56, respectively. Densification was performed during compression creep test and in consequence the amount of porosity is decreased compare to sintered n- B4C (Fig. 4.41 (b)). The measured average grain size of crept sample by SEM image is estimated at 180nm while

grain size distribution is from 55 nm to 350 nm. A comparison of Figs 4.55 and 4.41(b) confirms that the microstructural scale of the n-B_4C ceramic has not changed after creep deformation. Regarding to TEM, The presence of trapped dislocations with nano-twins has been confirmed in nanograins by TEM in nano-grains (Fig. 4.56).

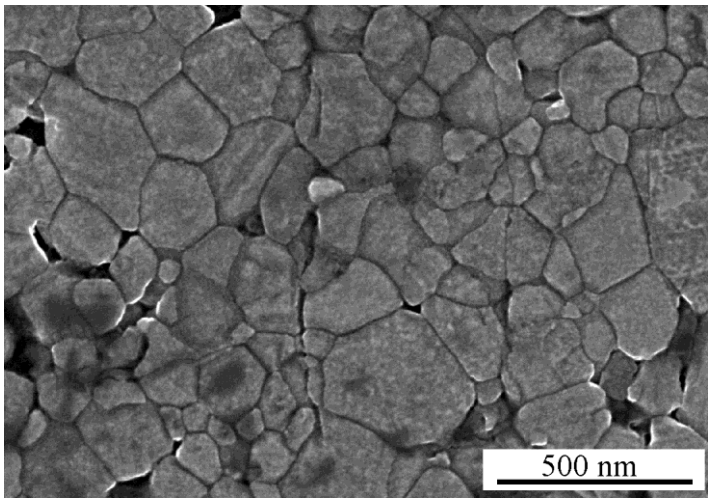

Fig. 4.55. SEM micrograph of 26% crept n-B_4C ceramic SPS sintered at 1600 ˚C for 3.

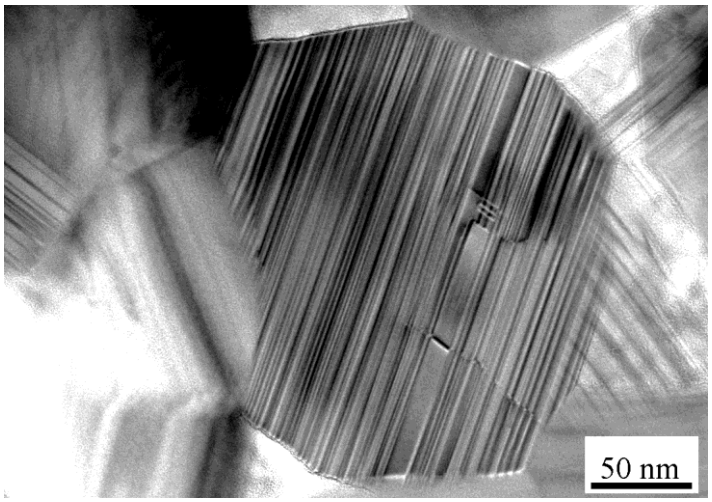

Fig. 4.56. TEM micrograph of 26% crept n-B_4C ceramic SPS sintered at1600 ˚C for 3.

Chapter V: Discussion

5- Introduction

At the first part of this chapter, some ideas of enhanced sinterability of boron carbide by spark plasma sintering (SPS) rather than conventional sintering methods are discussed. Later on, this chapter is mostly focused on comprehending and modelling of the high-temperature mechanical behaviour of boron carbide which is extensively studied and explained in details in this chapter. Regarding to room temperature mechanical properties, it was commented and discussed completely in chapter IV.

5-1- Role of spark plasma sintering in enhanced sinterability of B_4C

According to our results of processing in boron carbide by spark plasma sintering (SPS), sub-micrometric grained specimens can be prepared from initial powders with an average size equal to 500 nm, provided that temperatures as high as 1700 ˚C. While nano grained specimens were sintered by SPS at 1600 ˚C from nanometric boron carbide powders, as well. Such temperatures are significantly lower than the conventional processing methods like pressureless sintering or hot-press. There are several key factors responsible for these phenomena:

1- The initial powder size is smaller than conventionally used: such fact suggests that lower sintering temperatures can be chosen to get fully dense specimens provided the initial powder size is fine enough. On this regard, the improvement of sintering of very fine powders should be a crucial issue toward the end of very fine-grained boron carbide ceramics.

2- There is definitely an influence of either the electric current density or the Joule heating of the sintering powder on the grain growth and crystallographic change. Whether it is the result of the current density or Joule heating is still an unresolved question to us which should be studied in future. In fact, it is difficult to conclude because both thermal and electrical effects are coupled phenomena.

Another piece of evidence which can give some clues on the importance of Joule heating as opposed to current-induced plasma effects is a theoretical analysis of the local temperature sample. Due to the cylindrical symmetry of the experimental set-up, the steady-state local temperature can be rigorously calculated. The details are given in Appendix. I. Such temperature is given by:

$$T_0 = \left[\frac{1}{2\varepsilon s} \left(q_1 r_1^2 + q_2 \left(r_2^2 - r_1^2 \right) \right) T_\infty^4 \right]^{1/4} + \frac{q_2 \left(r_2^2 - r_1^2 \right)}{4k_2} + \frac{\left(q_1^2 - q_2^2 \right)}{2k_2} \ln\left(\frac{r_2}{r_1} \right) + \frac{q_1 r_1^2}{4k_1} \quad (5.1)$$

The meaning of all the symbols is given in appendix I. The essential physics indicate that the temperature depend on the power loss per unit volume dissipated inside the powder (q_1) or in the graphite die (q_2) in a complex way. According to electrodynamics, such losses are proportional to the electric conductivity and the square of the modulus of the electric field. Such electric field modulus is very approximately constant near the sample and inside the graphite die and it depends only on the electric voltage and the geometry of the die; i.e. its length. In consequence, the ratio q_1/q_2 depends on the ratio of electric conductivity σ_1/σ_2.

In the case of boron carbide, the electric conductivity is three orders of magnitude smaller than that of graphite[20], as displayed in Fig. 5.1. The ratio of thermal conductivities is less than one order of magnitude[19, 113]. That means that $q_1 << q_2$. Therefore, all the terms proportional to q_1 can be neglected in Eq. (5.1) and in consequence, for boron carbide specimens, the heating depends only on physical properties of the graphite die surrounding the sample (see Fig. 5.1). Such conclusion is in full agreement with the statements reported by Anselmi-Tamburini et al.[113] and Tiwari et al.[114] In fact, Anselmi-Tamburini et al.[113] estimated the fraction of electric current passing through the sample as a function of the sample electric conductivity. In our case, according to their results, it should be around 10% the total electric current. That means that the heating is essentially dominated by the graphite heating with a large fraction of the whole current density going through the die, the path with the smaller resistance.

There is certainly a weakness in this reasoning: in effect, the Joule heating is practically not altered by the presence of either two or five graphite foils sandwiching the sintering powder. Nevertheless the increase of resistivity produced by the graphite foils is also low, indicating that the dependence of the sinterability of boron carbide (and grain growth at 1800˚C) with electric current is quite remarkable. Such extreme dependence seems to be very astonishing and it has not clear physical basis.

In consequence, it is possible that there is an additional dependence on the pulsed electric field which is not still understood. Such idea has been pointed out by Chen et al.[115] in the analysis of the enhanced synthesis of $MoSi_2$. It is also possible that there is a non-linear effect of conductivity inducing overheating. Future work should be carried out to univocally identify the origin of exaggerated grain growth during the sintering of boron carbide at 1800˚C.

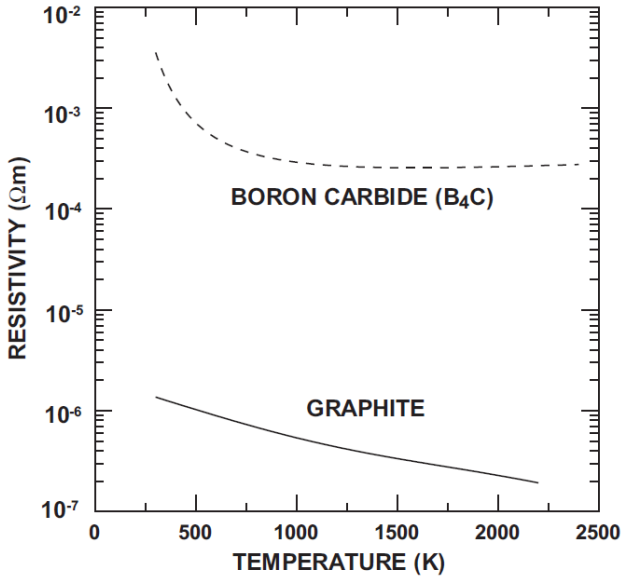

Fig. 5.1. Resistivity of graphite and boron carbide versus the temperature from data reported in literature[20, 113].

5-2- Analysing and modelling of creep behaviour in pure B_4C with different average grain size

In this study, creep behaviour of different pure boron carbide specimens with different average grain size from micron to sub-micron and finally to nano scale were compared. As it was shown in chapter IV through the analysis of creep experiments, none of the classical models in literature can explain creep behaviour of B_4C and it needs new modelling efforts which can explain such an unexpected behaviour. As a summery, there are following key features which stand out from the analysis of the creep experiments and the post-mortem microstructure:

1- Large scattering in values of both n and Q were recorded from creep experiments, making it difficult to identify the operative creep mechanisms in B_4C.

2- The scattering interval of theses two parameters decreased for coarse-grained specimens and the stress exponent and activation energy approaches to 3 and 650 $kJ.mol^{-1}$, respectively.

3- In other side, the smaller the grain size, larger scattering is observed.

4- The values of n or Q are not reproducible after a cycle of stress: remarkable hardening is found when returned back to the initial stress.

5- Microstructural observation on deformed specimens showed twins as a common feature in B_4C and extensive dislocation interactions with the twins together

with the presence of a complex network of sessile dislocation segments. While the as-processed B_4C is dislocation free, twin grains were observed.

The results from high temperature creep deformation permit to infer that dislocations are the elementary carriers of plasticity in these materials, although their dynamics must be coupled to the density of twins. The dislocation microstructure in deformed B_4C is consistent with the dislocation debris expected after multiple segment interactions during power-law creep deformation in ceramics[69, 98, 116]. Twins can be regarded as obstacles for dislocation motion. However, there is a significant difference between these defects and usual large-angle grain boundaries: whereas dislocations are fully blocked by these last ones and they are seldom transferred to another grain, twins can be overpassed by screw dislocations through cross-slipping. Such event is mechanically activated. This mechanism is the dominant one in this material, an idea playing a central role in our reasoning for modelling of the creep.

It is reasonable to assume that deformation is fulfilled predominantly by dislocation glide along the activated slip planes. The twin strain is restricted to very low strains[117]. Dislocations glide easily until they become blocked by twins. When blocked in them, their mobility decreases dramatically unless cross-slip relieves dislocation segment to an adjacent portion of crystallographic grain.

The steady-state strain rate must follow the classical Orowan relation with the dislocation density (ρ) and their average velocity ($\overline{V}$) i.e. $\dot{\varepsilon}_{ss} = \rho b \overline{V}$, together with the forest dislocation hardening law[98, 116]: $\sigma_{local} = Gb\sqrt{\rho}$, where σ_{local} is the "local stress" on dislocations. The quantity σ_{local} is the stress exerted on a dislocation minus the internal stress. The origin of this later quantity can be twofold: first, it is created by dislocation pile-ups or sessile dislocation networks stocked at the grain boundaries or twins. This is fully consistent with the microstructural observations. Secondly, it may be generated by some grain slide without accommodation. This second possibility cannot be discarded, although no evidence of grain boundary sliding was observed.

Furthermore, in steady-state regime, the coupling between twins and dislocation must impose a restriction on the dislocation microstructure: the mean free distance between dislocations is approximately equal to the mean distance between twins (t_w). The normalized twin size per grain, the ratio $\alpha \equiv t_w/d$ (being "d" the grain size), is a function of stress and temperature but it does not depend on the grain size "d". This is a consequence of the homogeneous character of strain.

Although the twinning generation process is stochastic, at the high-temperature regime α tends to follow an inversely proportional dependence with the flow stress because twins and dislocation correlates each other and the collective of dislocations obeys the hardening law. Regarding the temperature dependence, a linear dependence has been invoked[118]. In that case, this quantity follows a law $\alpha=1-(T/T_M)$, being T_M a constant. A straightforward algebra permits to prove that:

$$\frac{\partial \log \alpha}{\partial \log T} = \frac{\alpha - 1}{\alpha} \tag{5.2}$$

Finally, another interesting fact is the exponential dependence with strain at constant stress[117]; i.e. $\alpha \sim \exp(\varepsilon)$.

The mean velocity of dislocations is determined by the kinetics of dislocations overcoming twins. Since this must be a thermally and mechanically activated process and dislocations can overpass twins in both senses, it should follow the following law[119, 120]:

$$\overline{V} = K \exp\left(-\frac{\Delta F - \sigma_{local}\Omega}{kT}\right) - K \exp\left(-\frac{\Delta F + \sigma_{local}\Omega}{kT}\right) = 2K \sinh\left(\frac{\sigma_{local}\Omega}{kT}\right) \exp\left(-\frac{\Delta F}{kT}\right) \tag{5.3}$$

In this equation, ΔF is the energy barrier for atomic jump (usually the energy for self-diffusion of atomic species) plus the energy barrier for dislocations to overcome twins by cross-slip and Ω is the volume activation, usually $\Omega \sim b^3$ for short-ranged dislocation events. Finally, K is the proportionality constant.

It is generally accepted that the flow stress depends on the dislocation mean free path (DMFP) λ, i.e. the average spacing between obstacles to dislocation glide, this being determined by the predominant deformation mechanism. Different approaches can be followed to represent the DMFP. Here in the case of boron carbie, dislocations are blocked by twins which means DMFP is equal to the mean distance between twins (t_w): $\rho = \frac{1}{\lambda^2} = \frac{1}{t_w^2}$. In combination with both the hardening law, and making use of $\alpha=t_w/d$, it follows that:

$$\sigma = \frac{\mathrm{Gb}}{\mathrm{t_w}} = \frac{Gb}{\alpha d} \tag{5.4}$$

And finally with the use of the Orowan and hardening law and equations (5.3) and (5.4), strain rate can be obtained as following:

$$\dot{\varepsilon}_{ss} = A\sigma_{local}^2 \sinh\left(\frac{Gb\Omega}{\alpha kTd}\right) \exp\left(-\frac{\Delta F}{kT}\right) \tag{5.5}$$

In equation (5.5) A is a proportionality constant which does not depend on temperature or stress but it may depend on the grain size.

This is the expected mechanical equation of state for materials under coupled dislocation-twin dynamics. At given values of stress, "effective stress exponents" and "effective activation energies" emerge:

$$n^{eff} = \left(\frac{\partial \ln \dot{\varepsilon}}{\partial \ln \sigma}\right) = \frac{\sigma}{\sigma_{local}}\left[2 + \frac{\sigma_{local}\Omega}{kT}\coth\left(\frac{\sigma_{local}\Omega}{kT}\right)\right] = \frac{\sigma}{\sigma_{local}}\left[2 + \frac{Gb\Omega}{\alpha kTd}\coth\left(\frac{Gb\Omega}{\alpha kTd}\right)\right] \tag{5.6}$$

$$\begin{aligned} Q^{eff} &= \Delta F - 2\frac{kT^2}{\sigma - \sigma_i}\frac{\partial \sigma_i}{\partial T} - \left(\frac{\sigma_{local}}{\sigma}n^{eff} - 2\right)\left(T\frac{\partial \log \alpha}{\partial T} + 1\right)kT = \\ &= \Delta F - 2\frac{kT^2}{\sigma - \sigma_i}\frac{\partial \sigma_i}{\partial T} + \left(\frac{\sigma_{local}}{\sigma}n^{eff} - 2\right)\frac{1-2\alpha}{\alpha}kT \end{aligned} \tag{5.7}$$

The demonstrations of these two equations are given in appendix. II. Several physical implications can be derived from these results: the main one is the fact that the commonly-assumed power-law creep is violated. Such violation had been speculated to occur in the earth mantle under extreme conditions of pressure and temperature, but never proved in the laboratory[122].The quantities n and Q are not constant anymore and are replaced by "effective" ones. In particular, regarding the effective stress exponent, at given values of stress and temperature, it exhibits an extraordinary dependence with the grain size d. A characteristic grain size d_c can be adopted as:

$$d_c = \frac{Gb\Omega}{\alpha kT} \tag{5.8}$$

This quantity has the following physical meaning: if the grain size is much larger than the characteristic one, the equation (5.6) has an asymptotical limit equal to 3. This is the coarse-grain limit, in which the coupling between dislocations and twins is too weak. Indeed, grain sizes are large enough so that the twin area per unit volume becomes negligible. Therefore, in this limit case creep follows the conventional law of recovery. On the contrary, when the grain size is smaller than the critical value, the effective grain size diverges: the stress exponent increases without an upper bound with decreasing grain size. Numerical values for this quantity (G≅100GPa, b≅5.1 Å, T=1873 K) and α≅0.14, as estimated from TEM images, gives rise to d_c≅1600 nm.

Regarding the activation energy, the characteristic grain size also defines two very different physical regimes. In the coarse-grain limit, ($d >> d_c$), the effective activation

energy tends asymptotically to an almost constant value in full agreement with the predictions of conventional recovery creep.

A more extraordinary picture arises when $d<<d_c$. Equation (5.7) shows that the activation energy diverges: effective activation energy diverges with decreasing grain size. A straightforward consequence of this is the enhanced hardening expected when $d<<d_c$. Thus, twin-dislocation interaction turns to be very efficient for enhancement of creep resistance.

Figures 5.2 (a) and (b) display the experimental values of stress exponents and activation energy, respectively, for boron carbide polycrystals at fixed values of stress and temperature versus grain size. The continuous line is the theoretical estimate from the model developed above. The fitting is quite reasonable: the regression coefficient is 0.97 and 0.93 for Figs. 5.2 (a) and (b) respectively. In the particular case of Fig. 5.2(b), the fitting requires an input parameter: the activation energy for self-diffusion. The best fitting is found when Q=385 kJ/mol, the reported activation energy for volume diffusion of carbon in boron carbide[18, 123]. Notice that the asymptotical constant value for coarse-grain size is not necessarily equal to the self-diffusion activation energy, as it is shown in Fig (4.24) for coarse-grained B_4C and predicted for this model.

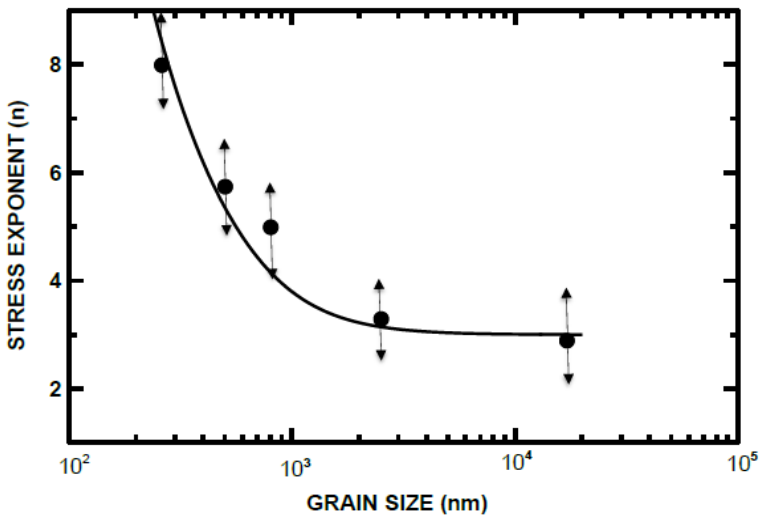

(a)

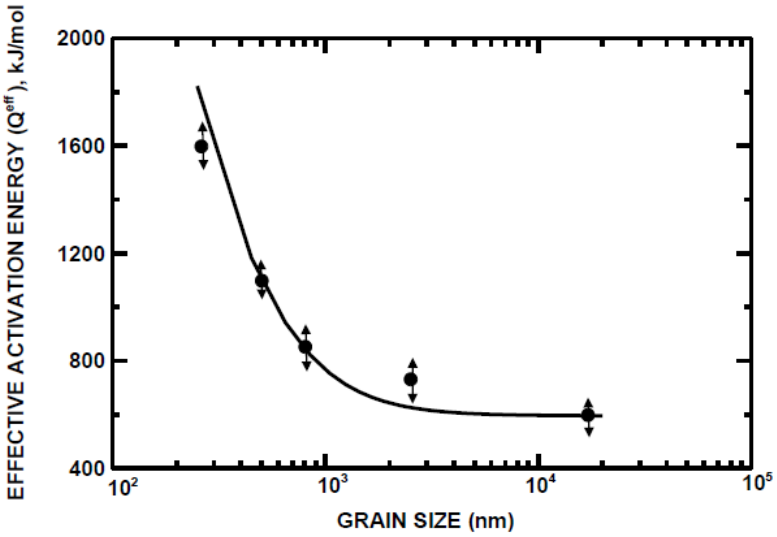

(b)

Fig. 5.2. (a) Effective stress exponent versus grain size at 200 MPa y 1600ºC. The solid line is the theoretical prediction derived from the model developed in the text. (b) Effective activation energy versus grain size at the same experimental conditions. The solid line is again the theoretical estimate derived from the model. Error bars for all data are displayed.

Finally, Fig. 5.3 is the fitting of all experimental ($\dot{\varepsilon}$,σ) points at a constant temperature to the equation (5.5). The fitting is quite reasonable, considering the usual scattering in data in plasticity studies. It is clear that power-law creep is not a universal law accounting for the high-temperature plasticity. In particular, it is violated when the singular combination of high covalent character, low stacking-fault energies and intense dislocation-twin coupling combines together. B_4C is a paradigm of the effective concurrence of all these features together at high temperatures.

Another important aspect of plasticity of this material deserves particular attention: after a stress cycle; i.e. one positive stress jump followed by some extent of strain ended abruptly by a negative stress jump and return to the previous stress level, a significant hardening is detected. The reason for this can be attributed to the internal stress field inside the polycrystalline material. The internal stress increases gradually as long as deformation proceeds. An obvious consequence of this is the reduction of the effective stress on dislocations; thus a progressive hardening effect should be observed. This effect should be enhanced at larger values of strain. Such tendency is displayed in creep plots before (See Fig. 4.6 (b)). Deformation stages at the same applied stress and temperatures are indicated by arrows. Progressive hardening is observed. By taking the values of the strain rate from a pair of stages, the change in internal stress can be obtained directly by application of equation (5.5):

$$\ln\left(\frac{\dot{\varepsilon}_2}{\dot{\varepsilon}_1}\right)=2\frac{\ln\left(1-\frac{\sigma_i(2)}{\sigma}\right)}{\ln\left(1-\frac{\sigma_i(1)}{\sigma}\right)}+\ln\left[\frac{\sinh\left(\frac{\sigma-\sigma_i(2)}{kT}\Omega\right)}{\sinh\left(\frac{\sigma-\sigma_i}{kT}\Omega\right)}\right]\cong 2\frac{\sigma_i(1)-\sigma_i(2)}{\sigma}+\frac{\sigma_i(1)-\sigma_i(2)}{kT}\Omega \tag{5.9}$$

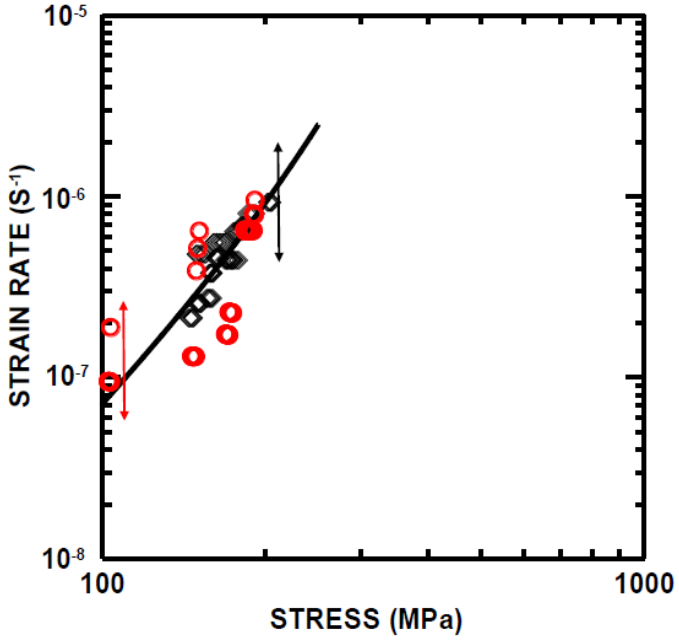

Fig. 5. Strain rate versus stress at constant temperature for the creep data showed in figures 1. Black points corresponds to data extracted from test at 1600ºC in sub-B_4C (700 nm), whereas red points are data taken from n-B_4C (130 nm) specimens at 1500ºC. Data were fitted to one non-linear law as displayed in equation (5.5). Error bars for both sets of data are provided in the figure.

For instance, making use of the two first segments indicated by arrows in Fig. 4.6(b) , the applied stress is 205 MPa. The strain rate reduced from $8.1\text{x}10^{-7}$ s^{-1} to $5.2\text{x}10^{-7}$ s^{-1}. Application of equation (5.9) gives rise to $\sigma_i(1)-\sigma_i(2)\cong$ -40 Mpa. This is the increase of internal stress between these two segments.

A straightforward consequence of this is the non-superplastic character of this material. A more exciting prospective follows after this result: The conditions for suppression of the internal stresses are a challenging research topic. If determined and used conveniently, the large extent of twinning coupled to dislocation motion will allow designing an exceptionally hard material together with a large ductility. That will be the

first example of one metal-like superhard ceramic a goal which at the aim of any research in ceramics.

5-3- Analysing and modelling of creep behaviour in B_4C composites

Creep results revealed that the mechanical response of these materials is remarkably different depending on the presence of amorphous graphite. We will treat both materials separately in order to elucidate the mechanism activated for each of them. Then we will compare the creep resistance of these two composites with pure boron carbide at a given temperature and in the same range of average grain size.

Creep behaviour in B_4C-SiC-G composite is completely different from pure boron carbide. As it was shown in chapter IV, there are several pieces of evidence from creep analysis in this composite:

1- Except one case of n=3, the stress exponents are very close to the value expected by creep with glassy phase, i.e. n=0.5.

2-The smaller scattering in the values of Q are the consequence of better reproducibility of the strain rate values after cyclical jumps. Such partial reproducibility is the consequence of more efficient grain rotations and sliding which consider for the majority of the full strain.

3- The presence of cavitations was evident in post-mortem specimen while the twinning and dislocations were not predominant features in this composite.

4-The easiness in grain motion induces an appreciable softening. We will come back to this aspect when comparing the mechanical response of both composites and pure boron carbide.

In consistency with the model proposed for high-temperature creep, it seems reasonable to suggest that deformation is the result of the combination of grain boundary sliding together with dislocation recovery. Grain boundary sliding is not accommodated by vacancies diffusion: it requires cavities to open up between grains.

Nevertheless, there is a big difference which must be pointed out: the graphite phase facilitates grains to slide each other, making the contribution of grain boundary sliding the dominant one.

Regarding to B_4C-SiC composite, the summery of creep behaviour can be written as followings:

1- The stress exponents are scattering from unity to values as high as 4 which can be associated to dislocation recovery combined with grain boundary sliding.

2- For composite without graphite, grain boundary sliding is less efficient and this is the reason why there is scattering in n values.

3- There is evidence of some twinning while the density of twinning is less than crept pure boron carbide and also the presence trapped dislocations in twins and complicated network of dislocations were proved by microstructural observation. But in this composite, the cavitation is not extensive.

All these features are consistent with activation of several micromechanical processes which occurred simultaneously. In order to be consistent with the statements proposed for B_4C-SiC-G composite, we point out that non-stationary creep can be the consequence of both grain boundary sliding together with dislocation recovery creep. Now grain boundary sliding is much less efficient. This is the reason why stress exponents tend to recovery creep expected values for such quantity.

To conclude this section, it is critical to elucidate whether the design of these new composites opens new perspectives for boron carbide-based ceramics. Fig. 5.4 shows the strain rate versus stress outputs for both B_4C-SiC-G composites and B_4C-SiC ones as well as those reported for pure boron carbide ones with similar average grain size (Fig. 4.6).

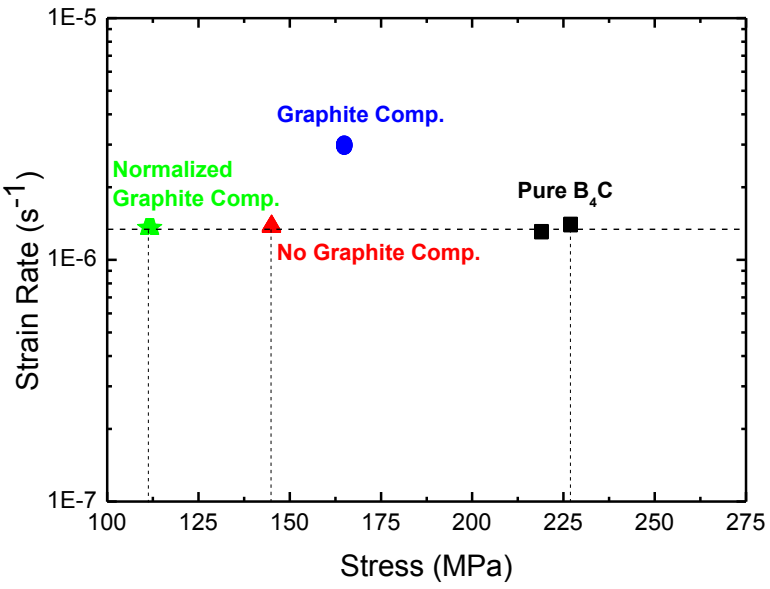

Fig. 5.4. Strain rate versus stress outputs for B_4C-SiC-G and B_4C-SiC composites and pure boron carbide ones at 1600 ˚C.

Data have been extracted from creep stages at a same temperature of reference, 1600ºC in the figure 5.4. For pure boron carbide, just data with similar strain rate of composites

were reported and compared. Black points correspond to data from pure B_4C specimens, whereas the blue and red ones are associated to B_4C-SiC-G composite and B_4C-SiC ones respectively. The green values are the expected stress values which would have been measured provided that the strain rate was the same for all three specimens. These last values have been calculated from the blue ones by normalization using a stress exponent equal to 0.5. Notice that this can be done only with the B_4C-SiC-G composite values, because a constant stress exponent has a real meaning in this material.

According to this plot the B_4C-SiC-G composites are the softer ones: for a common value of 1.4×10^{-6} s^{-1}, flow stresses are approximately 112 Mpa. This value should be compared with a level of stresses equal to 145 Mpa for B_4C-SiC composites, not to say with values as high as 225 Mpa for pure B_4C specimens. If a value equal to 1 is given to the pure specimens, the creep resistance for B_4C-SiC-G composites should be 50% that of pure specimens, and 64% for B_4C-SiC specimens.

In terms of potential application, the G-composites have an advantage which could be emphasized: grain boundary sliding is a more favourable process under creep, which would permit to increase the ductility to larger values of strain. It opens up the perspective of designing composites with complex shapes, coating or they suggest the search of a new phase, non-graphitic one which could protect boron carbide grains from oxidation under high-temperature conditions.

Chapter VI: Conclusion and ideas for further research

This research work has been focused on the spark-plasma sintering of fine-grained boron carbide polycrystals. The main achievements can be summarized as follows:

1-Sintering conditions and optimized values of pressure, temperature and time have been determined. The sintering procedure for fully-dense sample preparation with nano-grain retention is also discovered. Fully dense specimens with grain size as low as 130 nm have been prepared. Composites of boron carbide with silicon carbide and silicon carbide plus graphite were also fabricated.

2-Fracture properties of the specimens were measured by indentation techniques. Correlation between the sintering conditions and hardness and toughness is performed. Analysis of the crack propagation allowed an explanation of the fracture mechanisms playing a significant role.

3-High-temperature plasticity has been studied by means of compression creep tests at temperatures ranged from 1500-1800ºC. The results were fitted into the classical parameters of stress exponent and activation energy included in the Dorn equation. A critical analysis of these parameters allowed concluding that such fitting is not acceptable.

4-Modelling of high-temperature plasticity is carried out. A new model is developed. The essential ingredient of this one is the coupling between dislocation dynamics and twins generated during deformation. The model is in satisfactory agreement with the main experimental facts.

5-Analysis of the creep results in boron carbide-based composites is also made. Whereas graphite-boron carbide specimens can be understood in terms of a solution-precipitation classical model derived from the Wakai's one, silicon carbide-boron carbide samples exhibit a creep behavior which can be explained only in the context of the model developed in this dissertation.

Conclusiones

Este trabajo de investigación está consagrado al sinterizado mediante chispa de plasma y caracterización de las propiedades mecánicas de grano fino de policristales de carburo de boro. Los principales logros de este trabajo pueden resumirse como sigue:

1-Se han determinado las condiciones de sinterización y los valores optimizados de la temperatura y de la presión aplicadas. Se ha descubierto ell procedimiento de sinterización de polvos con tamaño de grano nanométrico que permite la retención del tamaño en la escala nano. De esta forma, muestras densas con tamaños de grano pequeño tales como 150 nm han podido ser logradas. Igualmente se han preparado composites de carburo de boro con grafito y de carburo de boro con carburo de silicio.

2-Las propiedades en fractura de las muestras preparadas en el apartado 2 se han determinado mediante técnicas de indentación. El análisis de la propagación de las grietas ha permitido dilucidar el mecanismo de fractura activado en este material.

3-La plasticidad a alta temperatura se ha estudiado mediante fluencia en compression a temperaturas incluidas en el interval entre 1500 y 1800ºC. Los resultados se intentaron ajustar mediante los parámetros clásicos de exponente de tension y energía de activación incluidos en la ecuación de Dorn. Un análisis crítico de los valores de estos parámetros ha permitido concluir que tal ajuste no es aceptable.

4-Se ha procedido al modelado de la plasticidad a alta temperatura. Se ha desarrollado un modelo original. El ingrediente esencial de éste es el acoplo entre la dinámica de las dislocaciones y el de las maclas generadas durante la deformación. El modelo está en un acuerdo satisfactorio con los principales hechos experimentales.

5- Finalmente se ha procedido a estudiar los resultados dela fluencia de composites basados en carburo de boro. Mientras que las muestras de carburo de boro con grafito pueden explicarse bien mediante un modelo de solución-precipitación basado en el clásico propuesto por Wakai, los composites de carburo de boro con carburo de silicio sólo pueden entenderse en el marco del modelo propuesto en este trabajo.

Refrences:

[1]F. Thevenot., "Boron Carbide A Comprehensive Review," *J Eur ceram Soc* 6205-225 (1990).

[2]V. Domnich., et al., "Boron Carbide: Structure, Properties, and Stability under Stress," *J Am Ceram Soc* 94 [11] 3605–3628 (2011).

[3]D. Emin., "Structure and Single-Phase Regime of Boron Carbides," *Phys. Rev. B*, 38 6041-6055 (1988).

[4]G. Will. and K. H. Kossobutzki., "An X-ray structure analysis of boron carbide , $B_{13}C_2$," *J Less Comm Mater*, 44 87-97 (1976).

[5]D. R. Tallant., et al., "Boron carbide structure by Raman spectroscopy," *Phys Rev B*, 40(8) 5649-5656 (1989).

[6]F. Mauri., N. Vast., and C. J. Pickard., "Atomic Structure of Icosahedral B_4C Boron Carbide from a First Principles Analysis of NMR Spectra," *Phys Rev Lett*, 87(8) 085506 (2001).

[7]A. K. Suri., et al., "Synthesis and consolidation of boron carbide:a review," *Int Mater Rev*, 55(1) 4-40 (2010).

[8]R. Lazzari., et al., "Atomic Structure and Vibrational Properties of Icosahedral B4C Boron Carbide," *Phys Rev Lett*, 83(16) 3230-3233 (1999).

[9]M. Bouchacourt. and F. Theveno., "The melting of boron carbide and the homogeneity range of the boron carbide phase," *J Less Comm Met*, 67 327-331 (1976).

[10]F. Thevenot., "A Review on Boron Carbide " *Key Eng Mater*, 56-57 59-88 (1991).

[11]B. Champagne. and R. Angers., "Mechanical Properties of Hot-Pressed B-B4C Materials," *J Am Ceram Soc*, 62(3-4) 149-153 (1979).

[12]F. P. Knudsen., "Dependence of mechanical strength of brittle polycrystalline specimens on porosity and grain size," *J Am Ceram Soc*, 42 876-887 (1959).

[13]D. Ghosh., et al., "Dynamic indentation response of fine-grained boron carbide," *J Am Ceram Soc*, 90(6) 1850-1857 (2007).

[14]S. Hayun., et al., "Static and dynamic mechanical properties of boron carbide processed by spark plasma sintering," *J Eur Ceram Soc*, 29 3395-3400 (2009).

[15]H. Lee. and R. F. Speyer., "Hardness and fracture toughness of pressureless-sintered boron carbide (B_4C)," *J Am Ceram Soc*, 85(5) 1291-1293 (2002).

[16]M. W. Chen., et al., "Microstructural characterization of commercial hot-pressed boron carbide ceramics," *J Am Ceram Soc*, 88(7)[1935-1942] (2005).

[17]G. A. Gogotsi., et al., "Complex investigation of hot-pressed boron carbide," *J Less Common Met*, 117 225-230 (1986).

[18]T. G. Abzianidze., A. M. Eristavi., and S. O. Shalamberidze., "Strength and creep in boron carbide (B_4C) and aluminum dodecaboride (α-AlB_{12})," *J Solid State Chem*, 154 191-193 (2000).

[19]CH. Wood., D. Emin., and P. E. Gray., "Thermal conductivity of boron carbide," *Phys Rev B*, 31 (1985).

[20]Ch. Wood. and D. Emin., "Conduction mechanism in boron carbide," *Phys Rev B*, 29 4582-4587 (1984).

[21]S.G. Savio., et al., "An experimental study on ballistic performance of boron carbide tiles," *Int J Impact Eng*, 38 535-541 (2011).

[22]B. Paliwal. and K.T. Ramesh., "Effect of crack growth dynamics on the rate-sensitive behaviorof hot-pressed boron carbide," *Scripta Mater* 57 481-484 (2007).

[23]M. Bouchacoart. and F. Thevenot., "The correlation between the thermoelectric properties and stoichiometric properties and stoichiometry in the boron carbide phase B_4C-$B_{10.5}C$," *J Mater Sci*, 20 1237-1247 (1985).

[24]S. Sasaki., et al., "Thermoelectric properties of boron carbide thin film and thin film based thermoelectricdevice fabricated by intense-pulsed ion beam evaporation," *Sci Technol Adv Mater*, 6 181-184 (2005).
[25]A. Riyas., et al., "A new physics design of control safety rods for prototype fast breeder reactor," *Ann Nucl Energ*, 35 1484-1491 (2008).
[26]D. Emin. and T. L. Aselage., "A propeosed boron-carbide-based solid-state neutron detector," *J Appl Phys*, 97 013529?1–013529?3 (2005).
[27]C. Dominguez., et al., "Investigation on boron carbide oxidation for nuclear reactor safety: experiments in highly oxidizing conditions," *J Nucl Mater*, 374 473-481 (2008).
[28]B. L. Grabchuk. and P. S. Kislyi., "Some features of the sintering behavior of pure and technical boron carbide," *Sov Powder Metall and Met Ceram*, 15 (6) 675-678 (1976).
[29]H. Lee. and R. F. Speyer., "Pressureless sintering of boron carbide," *J Am Ceram Soc*, 86(9) 1468-1473 (2003).
[30]L. Levin., N. Frage., and M. P. Dariel., "A novel approach for the preparation of B4C-based cermets," *Int J Refract Met Hard Mater*, 18 131-135 (2000).
[31]T. K. Roy., C. Subramanian., and A. K. Suri., "Pressureless sintering of boron carbide," *Ceram Int*, 32 227-233 (2006).
[32]R. F. Speyer. and H. Lee., "Improved pressureless densification of B_4C," *Ceram Trans*, 151 71-82 (2003).
[33]R. Angers. and M. Beauvy., "Hot pressing of boron carbide," *Ceram Int*, 10 49-55 (1984).
[34]D. Jianxin., "Erosion wear of boron carbide ceramic nozzles by abrasive air-jets," *Mat Sci Eng A*, 408 227-233 (2005).
[35]G. I. Kalandadze., S. O. Shalamberidze., and A. B. Peikrishvili., "Sintering of Boron and Boron Carbide," *J Solid State Chem*, 194-198 (2000).
[36]T. L. Hans., "Dense ceramic parts hot pressed to shape by HIP," *Mater Sci Res*, 17 571-582 (1984).
[37]P. Larsson., N. Axen., and S. Hogmark, "Improvements of the microstructure and erosion resistance of boron carbide with additives," *J Mater Sci*, 35 3433-3440 (2000).
[38]N. Cho., Z. Bao., and R. F. Speyer., "Density-and hardnessoptimized pressureless sintered and pot-hot isostatic pressed B_4C," *J Mater Res*, 20 2110-2116 (2005).
[39]K. A. Schwetz., L. S. Sigl., and L. Pfau., "Mechanical Properties of Injection Molded B4C–C Ceramics," *J Solid State Chem*, 133 68-76 (1997).
[40]R. F. Speyer. and E. A. Judson., "New process makes complexshaped armor a reality," *Am Ceram Soc Bull*, 85(3) 21-23 (2006).
[41]A. Goldstein., et al., "Carbide matrix composites by fast MW reaction-sintering in air of B_4C–SiC–Al mixtures," *Ceram Int*, 35(3) 1297-1300 (2008).
[42]K. Inoue., "Method and aparatus for controlling the porosity of electrically sintered body," Vol. US3317705, Japan, 1961.
[43]M. Omori., "Sintering, consolidation, reaction and crystal growth by the spark plasma system (SPS)," *Mat Sci Eng A*, 287 183-188 (2000).
[44]K. Inoue., "Electric discharge sintering," Vol. US3241956, Japan, 1963.
[45]U. Anselmi-Tamburini., J.E. Garay., and Z.A. Munir., "Fast low-temperature consolidation of bulk nanometric ceramic materials," *Scripta Mater*, 54 823-828 (2006).
[46]J. R. Groza. and A. Zavaliangos., "Sintering activation by external electrical field," *Mat Sci Eng A*, 287 171-177 (2000).

[47]Z. A. Munir., U. Anselmi-Tamburini., and M. Ohyanagi., "The effect of electric field and pressure on the synthesis and consolidation of materials: A review of the spark plasma sintering method," *J Mater Sci* 41 763-777 (2006).
[48]S. Hayun, et al., "Microstructural characterization of spark plasma sintered boron carbide ceramics," *Ceram Int*, 36 451-457 (2010).
[49]K. Sairama., et al., "Influence of spark plasma sintering parameters on densification and mechanical
properties of boron carbide," *Int J Refract Met Hard Mater*, 42 185-192 (2014).
[50]K. M. Reddy., et al., "Enhanced mechanical properties of nanocrystalline boron carbide by nanoporosity and interface phases," *Nature Commun*, 3:1052 doi: 10.1038/ncomms2047 (2012).
[51]J. E. Zorzi., C. A. Perottoni., and J. A. H. da Jornada., "Hardness and wear resistance of B_4C ceramics prepared with several additives," *Mater Lett*, 59 2932-2935 (2005).
[52]C. Subramanian., et al., "Effect of Zirconia addition on pressureless sintering of boron carbide," *Ceram Int*, 34 1543-1549 (2008).
[53]Y.C. Ch. Xu., K. Flodström., Zh. Li., S. Esmaeilzadeh., G. J. Zhang., , "Spark plasma sintering of B_4C ceramics: The effects of milling medium and TiB_2 addition," *Int J Refract Met Hard Mater*, 30 139-144 (2012).
[54]D. Jianxin., et al., "Microstructure and mechanical properties of hot-pressed B_4C/TiC/Mo ceramic composites," *Ceram Int*, 35 771-778 (2009).
[55]J. Deng., et al., "Microstructure and mechanical properties of hot-pressed B_4C/(W,Ti)C ceramic composites," *Ceram Int*, 28 425-430 (2002).
[56]A. Goldstein., Y. Yeshurun., and A. Goldenberg., "B_4C/metal boride composites derived from B4C/metal oxide mixtures," *J Eur ceram Soc*, 27 695-700 (2007).
[57]S. Yamada., et al., "B_4C–CrB_2 composites with improved mechanical properties," *J Eur ceram Soc*, 23 561-565 (2003).
[58]F. Thevenot., "Sintering of boron carbide and boron carbide-silicon carbide two phase materials and their properties," *J Nucl Mater*, 152 154-162 (1988).
[59]V. Skorokhod. and V. D. Krstic., "High strength-high toughness B_4C-TiB_2 composites," *J Mater Sci Lett*, 19 237-239 (2000).
[60]S.G. Huang., et al., "Microstructure and mechanical properties of pulsed electric current sintered B_4C–TiB_2 composites," *Mat Sci Eng A*, 528 1302-1309 (2011).
[61]S. Hayun., et al., "The high-strain-rate dynamic response of boron carbide-based composites: The effect of microstructure," *Acta Mater*, 58 1721-1731 (2010).
[62]S. Hayun., N. Frage., and M.P. Dariel., "The morphology of ceramic phases in B_xC–SiC–Si infiltrated composites," *J Solid State Chem*, 179 2875-2879 (2006).
[63]Q. Lin., et al., "Wetting of polycrystalline B_4C by molten Al at 1173–1473 K," *Scripta Mater*, 60 960-963 (2009).
[64]M. Mashhadi., et al., "Effect of Al addition on pressureless sintering of B4C," *Ceram Int*, 35 831-837 (2009).
[65]D. M. Hulbert., et al., "Continuous functionally graded boron carbide-aluminum nanocomposites by spark plasma sintering," *Mat Sci Eng A*, 493 251-255 (2008).
[66]A.K. Swarnakar., et al., "Ultrafine Al_2O_3–B_4C composites consolidated by pulsed electric current sintering," *J Alloys Comp*, 499 200-205 (2010).
[67]J. Sun., Ch. Liu., and R. Wang., "Low pressure hot pressing of B_4C matrix ceramic composites improved by Al_2O_3 and TiC additives," *Mat Sci Eng A*, 519 27-31 (2009).
[68]M. E. Kassner., "Fundamentals of Creep in Metals and Alloys," Elsevier, Oxford. UK, 2009.
[69]J. P. Poirier., "Creep of crystals," Cambridge University Press, Cambridge, 1985.

[70]C. E. Pearson., "The viscous properties of extruded eutectic alloys of lead-tin and bismuth-tin," *J Inst Metals*, 54 111-124 (1934).
[71]K. S. Arghavan., "Superplasticity," *Bull Mater Sci*, 6 689-698 (1984).
[72]M. F. Ashby. and R. A. Verrall., "Diffusion-accommodated flow and superplasticity," *Acta Metall*, 21 149-163 (1973).
[73]A. Ball. and M. M. Hutchinson., "Superplasticity in the aluminum-zinc eutectoid," *Metal Sci J*, 3 1-6 (1969).
[74]R. C. Gifkins., "Grain-boundary sliding and its accommodation creep and superplasticity," *Metall Trans A*, 7 1225-1232 (1976).
[75]E. Arzt., M. F. Ashby., and R. A. Verrall., "Interface controlled diffusional creep," *Acta Metall*, 31 1977-1989 (1983).
[76]D. Gómez-García., et al., "Diffusion-driven superplasticity in ceramics: Modeling and comparison with available data," *Phys Rev B*, 80 214107.1-214107.8 (2009).
[77]T. H. Courtney., "Mechanical Behavior of Materials," Waveland Press, Inc., US, 2005.
[78]G. R. Love., "Dislocation pipe diffusion," *Acta Metall*, 12 731-737 (1964).
[79]J. Weertman., "Steady state creep through dislocation climb," *J Appl Phys*, 28 362-364 (1957).
[80]J. Weertman., "Steady-state creep of crystal," *J Appl Phys*, 28 1185-1189 (1957).
[81]S. Y. Hu., et al., "Dynamic drag of solute atmosphere on moving edge dislocations—Phase-field simulation," *J Appl Phys*, 96 229-236 (2004).
[82]P.M. A. S. Argon., Elsevier Science 1996: p. 1958-2007., "Mechanical properties of single-phase crystalline media: deformation in the presence of diffusion: chapter 22," Physical Metallurgy; fourth, revised and enhanced edition, 1996.
[83]V. Zamora., et al., "Spark-plasma sintering of ZrB_2 ultra-high-temperature ceramics at lower temperature via nanoscale crystal refinement," *J Eur Ceram Soc*, 32 2529-2536 (2012).
[84]V. Zamora., et al., "On the enhancement of the spark-plasma-sintering kinetics of ZrB_2–SiC powder mixtures subjected to high-energy co-ball-milling," *Ceram Int*, 39 4191-4204 (2013).
[85]S. L. Dole., S. Prochazka., and J.A.C.S. R. H. Doremus., "Microstructural coarsening duringsintering of boron carbide," *J Am Ceram Soc*, 72 958-966 (1989).
[86]S. Prochazka., S. L. Dole., and C. J. Hejna., "Abnormal Grain Growth and Microcracking in Boron Carbide," *J Am Ceram Soc*, 68 C-235-C236 (1985).
[87]L. S. Walker., W. R. Pinc., and E. L. Corral., "Powder processing effects on the rapid low-temperature densification of ZrB_2," *J Am Ceram Soc*, 95 194-203 (2012).
[88]L. B. McCusker, et al., "Rietveld refine-ment guidelines," *J Appl Crystallogr*, 32 36-50 (1999).
[89]G. R. Anstis., et al., "A critical evaluation of indentation techniques for measuring fracture toughness: I, Direct crack measurments," *J Am Ceram Soc*, 64 533-538 (1981).
[90]B. Lawn. and R. Wilshaw., "Review Indentation fracture: principles and applications," *J Mater Sci*, 10 1049-1081 (1975).
[91]J. J. Kruzica., et al., "Indentation techniques for evaluating the fracture toughness of biomaterials and hard tissues," *J Mech Behavior Biomed Mater*, 2 384-395 (2009).
[92]C. B. Ponton. and R. D. Rawlings., "Vickers indentation fracture toughness test part 1 review of literature and formulation of standardized toughness equations," *Mater Sci Tech*, 5 865-872 (1989).
[93]K. Niihara., R. Morena., and D. P. A. Hasselman., "Evaluation of KIC of brittle solid by the indentation method with low crack-to indent ratios," *J Mater Sci Lett*, 1 13-16 (1982).

[94]K. Niihara., "A fracture mechanics analysis of indentation-induced Palmkvist crack in ceramics," *J mater Sci Lett*, 2 221-223 (1983).
[95]M. A. Kuzenkova., et al., "The structure and properties of sintered boron carbide," *J Less Comm Mater*, 67 217-223 (1979).
[96]M. Chen., J. W. Mc Cauley., and K. J. Hemker., "SHock induced localized amorphization in boron carbide," *Science*, 299 1563-1566 (2003).
[97]D. Ge., et al., "Structural damage in boron carbide under contact loading," *Acta Mater*, 52 3921-3927 (2004).
[98]J. Friedel., "Dislocations in crystals," Pergamon Press, 1964.
[99]D. Gómez-García., et al., "Deformation mechanisms for high-temperatrure creep of high yttria content stabilized zirconia single crystals," *Acta Mater*, 44 991-999 (1996).
[100]K. H. G. Ashbee. and C. K. H. Dubose., "Dislocation nodes in boron carbide, with special reference to non-stoichiometry," *Acta Mater*, 20 241-245 (1972).
[101]R. M. Young. and R. McPherson., "Temperature-gradient driven diffusion in rapidrate sintering," *J Am Ceram Soc*, 72 1080-1081 (1989).
[102]D. Beruto., R. Botter., and A. W. Searcy., "Influence of temperature gradients onsintering: experimental tests of a theory," *J Am Ceram Soc*, 72 232-235 (1989).
[103]R. M. German., "Sintering theory and practice," Willey, New York, USA, 1996.
[104]K. H. G. Ashbee., "Defects in boron carbide before and afterv neutron irradiation," *Acta Mater*, 19 1079-1085 (1971).
[105]G. S. Oleinik. and T. V. Ostapchuk., "Effect of pores on the cleavage of twinned boron carbide crystals," *Powder Metallurgy and Metal Ceramics*, 34 500-504 (1995).
[106]T. Sano. and Ch. L. Randow., "The effect of twins on the mechanical behavior od boron carbide," *Metallurgical and Materials Transactions A*, 42 570-574 (2011).
[107]M. A. Meyers., A. Mishra., and D.J. Benson., "Mechanical properties of nanocrystalline materials," *Prog Mater Sci*, 51 427-556 (2006).
[108]C. A. Galan., et al., "High-energy ball-milling of ZrB_2 in the presence of graphite," *J Am Ceram Soc*, 93 3072-3075 (2010).
[109]M. W. Barsoum., "Fundamentals of ceramics," McGraw-Hill, NY, USA, 1997.
[110]P. T. B. Shaffer., "Engineering properties of carbides," Vol. 4. Ceramics and glasses, Materials Park, Ohio, 1991.
[111]D. C. Pender., et al., "Gradients in elastic modulus for improved contact-damage resisrance: part II, the silicon nitride-silicon carbide system," *Acta Mater*, 49 3263-3268 (2001).
[112]Ch. Chen., et al., "Microstructures and grain boundaries of cubic boron nitrides," *Diamond & Related Materials*, 32 27-31 (2013).
[113]U. Anselmi-Tamburini., et al., "Fundamental investigations on the spark plasma sintering/synthesis process. II. Modeling of current and temperature distributions," *Mat Sci Eng A*, 394 139-148 (2005).
[114]D. Tiwari., B. Basu., and B. Biswas., "Simulation of thermal and electric field evolution during spark plasma sintering," *Ceram Int*, 35 699-708 (2009).
[115]W. Chen., et al., "Fundamental investigations on the spark plasma sintering/synthesis process: I. Effect of dc pulsing on reactivity," *Mat Sci Eng A*, 394 132-138 (2005).
[116]U. Messerschmidt., "Dislocation dynamics during plastic deformation," Springer-Verlag, Berlin, Germany, 2010.
[117]Y. Li. and M. Enoki., "Evaluation of the twinning behavior of polycrystalline magnesium at room temperature by acoustic emission," *Mater Trans*, 48 1215-1220 (2007).

[118]Y. Wei., "The kinetics and energetics of dislocation mediated de-twinning in nano-twinned face-centered cubic metals," *Mat Sci Eng A*, 528 1558-1566 (2011).
[119]A. H. Cottrell., "Dislocations and plastic flow in cryrtals," Oxford University Press, Oxford, UK, 1963.
[120]D. Mc-Lean., "The physics of high-temperature creep in metals," *Rep Prog Phys*, 29 1-33 (1966).
[121]L. P. Kubin., "Dislocations, mesoscale simulations and plastic flow," Oxford University Press, Oxford, U.K.,, 2013.
[122]M. C. Tsenn. and N. L. Carter., "Upper limits of power-law creep of rocks," *Tectonophysics*, 136 1-26 (1987).
[123]W. Borchert. and A. R. Kerler., "Kinetische analyse des sinterns der borncarbide," *Metallwissenschaft und Technik*, 29 993-1002 (1975).

Appendix I.

Calculation of the local heating under stationary conditions on sintering powders by spark plasma sintering

Let consider a sample whose thickness is smaller than the punch length. The mathematical symbols considered in this calculation are given in the table displayed below.

Symbol	Quantity
r_1	Inner radius of graphite die
r_2	Outer radius of graphite die
K_1	Thermal conductivity of graphite
K_2	Thermal conductivity of sintering powder
T_∞	Room temperature (very far from the die)
s	Stefan-Boltzmann constant
ε	Emissivity of graphite (usually equal to 1)
q_1	Heat loss dissipated by Joule effect in the sintering powder
q_2	Heat loss dissipated by Joule effect in the graphite
T_2	Temperature at the surface of graphite die
T_0	Temperature inside the sintering sample

Under steady-state conditions, the temperature should obey the heat equation:

$$\frac{-\mathrm{K}}{\mathrm{r}}\frac{\partial}{\partial r}\left(r\frac{\partial T}{\partial r}\right)=q \qquad \text{(I.1)}$$

Such equation must be resolved in two regions: region I (inside the sintering powder; i.e. $0\leq r\leq r_1$) and region II (graphite die; i.e. $r_1\leq r\leq r_2$).

The solution to this equation can be written as follows:

$$T_{-(r)}=T_0-\frac{q_1 r^2}{4K_1}, \qquad \text{If } 0\leq r\leq r_1 \qquad \text{(I.2)}$$

$$T_{+(r)}=C_1+C_2\ln r-\frac{q_2 r^2}{4K_2}, \qquad \text{If } r_1\leq r\leq r_2 \qquad \text{(I.3)}$$

The constant T_0, C_1 and C_2 can be calculated by imposing the following boundary conditions:

1. Continuity of the temperature at $r=r_1$. This means that $T_-(r_1)=T_+(r_1)$.
2. Continuity of heat flux at $r=r_1$. this condition would imply that: $K_1\left(\partial T/\partial r\right)_{r_1}=K_2\left(\partial T/\partial r\right)_{r_2}$.
3. The heat flux at the surface of graphite die should follow the Stefan-Boltzmann law: $K_2\left(\partial T/\partial r\right)_{r_2}=\varepsilon s\left(T_2^4-T_\infty^4\right)$.
4. Finally, the temperature T_2 should be obtained also from the following equation: $T_+(r_2)=T_2$.

This set of equations allows obtaining a univocal value for the temperature T_0 and T_2.

$$T_0=\left[\frac{1}{2\varepsilon s}\left(q_1 r_1^2+q_2\left(r_2^2-r_1^2\right)\right)+T_\infty^4\right]^{1/4}+\frac{q_2\left(r_2^2-r_1^2\right)}{4k_2}+\frac{\left(q_1^2-q_2^2\right)}{2k_2}\ln\left(\frac{r_2}{r_1}\right)+\frac{q_1 r_1^2}{4k_1} \qquad \text{(I.4)}$$

$$T_2=\left[\frac{1}{2\varepsilon s}\left(q_1 r_1^2+q_2\left(r_2^2-r_1^2\right)\right)+T_\infty^4\right]^{1/4} \qquad \text{(I.5)}$$

Appendix II.

The demonstrations of the two equations of stress exponent and activation energy for boron carbide ceramics

As it is shown in chapter V, steady-state strain rate obtained as following:

$$\dot{\varepsilon}_{ss} = A\sigma_{local}^2 sh\left(\frac{\sigma_{local}\Omega}{kT}\right)\exp\left(-\frac{\Delta F}{kT}\right) \qquad \text{(II.1)}$$

Also it is demonstrated in chapter V, combination of hardening law (Fridel law: $\sigma_{local} = Gb\sqrt{\rho}$ where σ_{local} is the "local stress" on dislocations. The quantity σ_{local} is the stress exerted on a dislocation minus the internal stress: $\sigma_{local}=\sigma-\sigma_i$), and making use of $\alpha=t_w/d$, while:

$$\rho = \frac{1}{\lambda^2} = \frac{1}{t_w^2} \qquad \text{(II.2)}$$

Stress can be written as:

$$\sigma_{local} = \frac{Gb}{t_w} = \frac{Gb}{\alpha d} \qquad \text{(II.3)}$$

The equation (II.1) can be rewritten as following:

$$\ln\dot{\varepsilon}_{ss} = \ln A + \ln sh\left(\frac{\sigma_{local}\Omega}{kT}\right) - \frac{\Delta F}{kT} + 2\ln\sigma_{local} \qquad \text{(II.4)}$$

Stress exponent (n) can be obtained by derivative of steady state strain rate with stress:

$$n = \frac{\partial\ln\dot{\varepsilon}}{\partial\ln\sigma} = \sigma\frac{\partial\ln\dot{\varepsilon}}{\partial\sigma_{local}}\frac{\partial\ln\sigma_{local}}{\partial\ln\sigma} \qquad \text{(II.5)}$$

For equation (II.4), n^{eff} can be obtained as:

$$n^{eff} = \frac{\sigma}{\sigma_{local}}\left[2 + \frac{ch\left(\frac{\sigma_{local}\Omega}{kT}\right)}{sh\left(\frac{\sigma_{local}\Omega}{kT}\right)}\frac{\sigma_{local}\Omega}{kT}\right] = \frac{\sigma}{\sigma_{local}}\left[2 + \frac{\sigma_{local}\Omega}{kT}\coth\left(\frac{\sigma_{local}\Omega}{kT}\right)\right]$$

(II.6)

And by substitution of equation (II.3) in equation (II.6), one obtains:

$$n^{eff} = \frac{\sigma}{\sigma_{local}}\left[2 + \frac{Gb\Omega}{\alpha kTd}\coth\left(\frac{Gb\Omega}{\alpha kTd}\right)\right] \qquad \text{(II.7)}$$

Let's define d_c as $d_c = \frac{Gb\Omega}{\alpha kT}$. Then equation (II.7) cab be written as:

$$n^{eff} = \frac{\sigma}{\sigma_{local}}\left[2 + \frac{d_c}{d}\coth\left(\frac{d_c}{d}\right)\right] \qquad \text{(II.8)}$$

Regarding to activation energy, Q can be defined by:

$$Q = -\frac{\partial\ln\dot{\varepsilon}_{ss}}{\partial\frac{1}{kT}} = kT^2\frac{\partial\ln\dot{\varepsilon}_{ss}}{\partial T} \qquad \text{(II.9)}$$

By use of equation (II.4), Q^{eff} can be written as:

$$Q^{eff} = \Delta F + 2kT^2\frac{\partial\ln\sigma_{local}}{\partial T} + kT^2\frac{\partial}{\partial T}\ln\left[sh\left(\frac{\sigma_{local}\Omega}{kT}\right)\right] \qquad \text{(II.10)}$$

Using equation (II.3), equation (II.10) is as following:

$$Q^{eff} = \Delta F + 2kT^2 \frac{\partial \ln \sigma_{local}}{\partial T} + kT^2 \frac{\partial}{\partial T} \ln\left[sh\left(\frac{Gb\Omega}{\alpha kTd} \right) \right] \qquad \text{(II.11)}$$

In this equation, just kT and α depend on T and $\sigma_{local}=\sigma-\sigma_i$ .Thus:

$$Q^{eff} = \Delta F + \frac{2kT^2}{\sigma_{local}} \frac{\partial \sigma_{local}}{\partial T} + kT^2 \left[\frac{ch\left(\frac{Gb\Omega}{\alpha kTd} \right)}{sh\left(\frac{Gb\Omega}{\alpha kTd} \right)} \frac{Gb\Omega}{kT} \left(-\frac{1}{T\alpha^2} \frac{\partial \alpha}{\partial T} - \frac{1}{T^2 \alpha} \right) \right] =$$

$$\Delta F - \frac{2kT^2}{\sigma - \sigma_i} \frac{\partial \sigma_i}{\partial T} + \coth\left(\frac{Gb\Omega}{\alpha kTd} \right) \left[-\frac{Gb\Omega T}{d\alpha^2} \frac{\partial \alpha}{\partial T} - \frac{Gb\Omega}{\alpha d} \right] = \qquad \text{(II.12)}$$

$$\Delta F - \frac{2kT^2}{\sigma - \sigma_i} \frac{\partial \sigma_i}{\partial T} + \frac{Gb\Omega}{\alpha kTd} \coth\left(\frac{Gb\Omega}{\alpha kTd} \right) \left[-kT - kT \frac{\partial \ln \alpha}{\partial \ln T} \right]$$

And by substitution of equation (II.7) in equation (II.12), one obtains:

$$Q^{eff} = \Delta F - \frac{2kT^2}{\sigma - \sigma_i} \frac{\partial \sigma_i}{\partial T} - \left(\frac{\sigma_{local}}{\sigma} n^{eff} - 2 \right) kT \left[1 + \frac{\partial \ln \alpha}{\partial \ln T} \right] \qquad \text{(II.13)}$$

If α depends on T as:

$$t_w = d\left(1 - \frac{T}{T_m} \right) \qquad \text{(II.14)}$$

It was defined in chapter V that $\alpha=t_w/d$. Thus:

$$\alpha = 1 - \frac{T}{T_m} \qquad \text{(II.15)}$$

And:

$$\ln \alpha = \ln\left(1 - \frac{T}{T_m} \right) \qquad \text{(II.16)}$$

Therefore:

$$\frac{\partial \ln \alpha}{\partial \ln T} = T \frac{\partial \ln \alpha}{\partial T} = T \frac{-\frac{1}{T_m}}{1 - \frac{T}{T_m}} = \frac{\alpha - 1}{\alpha} \qquad \text{(II.17)}$$

By substitution equation (II.17) in (II.12), one obtains:

$$Q^{eff} = \Delta F - \frac{2kT^2}{\sigma - \sigma_i} \frac{\partial \sigma_i}{\partial T} - \left(\frac{\sigma_{local}}{\sigma} n^{eff} - 2 \right) kT \left[1 + \frac{\alpha - 1}{\alpha} \right] =$$

$$\Delta F - \frac{2kT^2}{\sigma - \sigma_i} \frac{\partial \sigma_i}{\partial T} + \left(\frac{\sigma_{local}}{\sigma} n^{eff} - 2 \right) \frac{1 - 2\alpha}{\alpha} kT \qquad \text{(II.18)}$$